Enhancing the performances of the MOF-based anodes for lithium ion batteries by order/disorder engineering

Gao, Chengwei

DOI (link to publication from Publisher):
10.54337/aau443824154

Publication date:
2021

Document Version
Publisher's PDF, also known as Version of record

ENHANCING THE PERFORMANCES OF THE MOF-BASED ANODES FOR LITHIUM-ION BATTERIES BY ORDER/DISORDER ENGINEERING

BY
CHENGWEI GAO

DISSERTATION SUBMITTED 2021

AALBORG UNIVERSITY
DENMARK

ENHANCING THE PERFORMANCES OF THE MOF-BASED ANODES FOR LITHIUM-ION BATTERIES BY ORDER/DISORDER ENGINEERING

by

Chengwei Gao

AALBORG UNIVERSITY
DENMARK

Dissertation submitted 2021

Dissertation submitted: May 2021

PhD supervisor: Prof. Yuanzheng Yue,
Aalborg University

PhD co-supervisors: Prof. Yanfei Zhang
Qilu University of Technology

Prof. Søren Knudsen Kær,
Aalborg University

PhD committee: Associate Professor Morten Lykkegaard Christensen
Aalborg University (chair)

Professor Liqiang Mai
Wuhan University of Technology

Associate Professor Dorthe B. Ravnsbæk
University of Southern Denmark

PhD Series: Faculty of Engineering and Science, Aalborg University

Department: Department of Chemistry and Bioscience

ISSN (online): 2446-1636
ISBN (online): 978-87-7210-947-3

Published by:
Aalborg University Press
Kroghstræde 3
DK – 9220 Aalborg Ø
Phone: +45 99407140
aauf@forlag.aau.dk
forlag.aau.dk

Printed in Denmark by Rosendahls, 2021

CV

Mr. Chengwei Gao was born in Zhoukou, Henan, P. R. China in June 1991. He got his Bachelor's degree and Master's degree in Chemistry in Zhengzhou University, P. R. China in 2015 and in 2017. He started his PhD study at Department of Chemistry and Bioscience in Aalborg University in November, 2017. His research has been focused on metal organic framework based materials for lithium ion batteries during the three-year PhD study at AAU.

ENGLISH SUMMARY

Lithium-ion batteries (LIBs) is one of the most popular energy storage devices in modern society due to their advantages compared with traditional energy storage devices, such as light weight, high power density and high energy density. However, the fast development of the electric vehicles, smart grid and portable devices urgently demand better performance from LIBs. To meet the ever-increasing demands, new anode materials with higher capacity have been extensively investigated in recent years. Metal organic frameworks (MOF) shows great potentials as electrode materials for LIBs due to their great porosity, high surface area and tunable chemical components. In this thesis, preparation and electrochemical performance of MOF-based anode materials have been investigated.

To study the impact of lithiation/delithiation processes on the structure of MOFs as anode materials, an Al-MOF (chemical formula: $Al(OH)[O_2C–C_6H_4–CO_2]$) is prepared, and then uniformly covered with graphene sheets to improve the electronic conductivity. After electrochemical characterizations, it is noticed that the lithiation/delithiation could induce pronounced structural changes of the Al-MOF, which is proposed as an order-disorder transition. This transition generates more open channels, thereby benefiting the diffusion and storage of Li^+ ions. Therefore, this MOF/graphene composite exhibits an increasing capacity along with cycling.

In addition, MOF itself could also be used as protection layers to buffer the volume changes of other high-capacity anode materials for LIBs. As a proof of concept, nanosized SnO_2 are packed into MOF to obtain SnO_2@MOF composite, which is one of the most promising anode materials. SnO_2 nano particles are assembled into MOF via a wet impregnation process, and then wrapped by graphene to increase the electronic conductivity. The as-prepared SnO_2@MOF/graphene composite exhibits an excellent cycling stability as well as great capacity. In the meantime, this MOF protection strategy also provides a new way to increase the cycling stability of other anode materials.

The structure-performance relationship is vital for designing better anode materials. To investigate this relationship, MOF with same components but different structures, i.e., crystalline, glass, and amorphous MOF, were prepared and characterized as anodes for LIBs. The glass MOF is prepared by melt quench method and the amorphous MOF is obtained via a high energy ball mill process. The electrochemical results reveal that the MOF glass (Cobalt ZIF-62) exhibited the best performance. This phenomenon could be explained by the advantages of glass materials, i.e., isotropic structure, higher energy state, and large free volume. This finding may be crucial for the development of glass materials for LIBs.

DANSK RESUME

Litium ion batterier (LIBs) er en af de mest populære energiopbevaringsteknologier i det moderne samfund. Dette skyldes at de har mange fordele over andre traditionelle energiopbevaringsteknologier da de blandt andet har en lav vægt, høj energitæthed og effekttæthed. På trods af disse fordele har den hurtige udvikling af elektriske køretøjer, smart elnets, og håndholdte elektriske enheder sat et enormt pres på at udvikle bedre og mere effektive LIBs. For at imødekomme det stigende behov har forskere fokuseret på udviklingen af nye anode materialer med høj kapacitet i de seneste år. Metalorganiske gitter (MOF) har udvist et stort potential som elektrode materiale i LIBs på grund af deres høje porøsitet, overflade areal og deres justerbare kemiske sammensætning. Denne Ph.d.-afhandling undersøger produktionen og den elektrokemiske ydelse af MOF baseret anode materialer.

For at undersøge effekten af lithiering/de-lithierings processen på strukturen af MOFs som anode materiale blev en Al-MOF (kemisk strukturformel: $Al(OH)[O_2C–C_6H_4–CO_2]$) syntetiseret og spredt uniformt ud over graphen ark for at øge deres elektriske ledeevne. Efter den elektrokemiske karakterisering af disse materialer blev det opdaget at lithiering/de-lithierings processen påfører en tydelig faseændring af Al-MOFen, som er forklaret til at forekomme gennem en orden-til-uorden faseovergang. Denne overgang danner kanaler i graphenstrukturen, hvilket øger transporten og opbevaringen af Li^+-ioner. På grund af dette udviser denne MOF/graphen komposit en elektrisk kapacitet som siger med antallet af cyklusser.

Derudover kan MOFs bruges som et bufferlag til at beskytte imod volumeændringer i højkapacitetsanodematerialer i LIBs. Et konceptbevis findes med nanostørrelse SnO_2 introduceret I MOFs for at danne et SnO_2@MOF komposit som har vist sig at være et yderst lovende anodemateriale. Tinoxid nanopartiklerne er integreret I MOFen gennem våd impregnering for at forbedre den elektriske ledeevne. De fabrikerede SnO_2@MOF kompositter udviser fremragende cyklisk stabilitet samt kapacitet. Ved at inddrage MOFs som et bufferlag bliver det også muligt at udvikle måder at forbedre den cykliske stabilitet af andre anodematerialer.

Struktur/ydeevne forholdet er vitalt for at kunne designe bedre anode materialer. For at undersøge forholdet mellem disse blev MOFs med samme opbygning men forskellige struktur (krystallinsk, glas og amorf) fremstillet som anodemateriale of LIBs. Glas MOF er fremstillet gennem smelte frysning metoden og amorfe MOFs blev fremstilt via en højenergi kuglemølle proces. De elektrokemiske resultater viser at MOF glasset (Kobolt ZIF-62) udviser den bedste ydeevne. Dette fænomen kan forklares med de fordele der er med glasmaterialer, deres isotropiske struktur, højere energi stadie, og større frie volumen. Disse resultater kan blive essentielle for udviklingen af glasmaterialer til LIBs

ACKNOWLEDGEMENTS

I would like to say thank you to a great number of people for their help during my PhD study. If would be impossible to accomplish my PhD study and research without their kind support. First and foremost, I would like to thank my supervisor Professor Yuanzheng Yue. I had a skype meeting with him four years ago when I just obtained my master's degree. I was thrilled by his scientific knowledge and his cautious attitude toward research works after getting to know him afterwards. It encouraged me come to Denmark for pursuing my PhD degree with him in 2017. With his guidance and support, I feel comfortable to conduct my research independently. We had spent a lot of time together to share research ideas, discuss experimental results, revise our papers as well as drink a cup of coffee. I am very grateful for his dedicated supervision in my PhD study.

Then, I would like to give my appreciation to my co-supervisor Professor Yanfei Zhang. Her research creativity, scientific attitude and working efficiency inspire me to conduct my work. Discussions with her are always joyful and meaningful. I benefited greatly from her suggestions and encouragement whenever I meet challenges. And her writing skills impressive me and stimulate me to improve my writing ability. With her kind help, especially in academic, I could perfectly finish my experiments in three years.

It is a marvelous experience to work with all my colleagues in the chemistry section. They helped me so much in conducting my experiments, reviewing my paper as well as other leisure activities, like coffee breaks and cake sharing. I would like to thank my colleagues and collaborators: Prof. Søren K. Kær, Assoc. Prof. Vittorio Boffa, Prof. Morten Smedskjær, Assoc. Prof. Donghong Yu, Dr. Assoc. Prof. Morten Christensen, Assoc. Prof. Wanmin Liu, Assoc. Prof. Thorbjørn Nielsen, Assoc. Prof. Mads Jørgensen, Assoc. Prof. Cejna Quist-Jensen, Dr. Hao Liu, Dr. Ang Qiao, Dr. Chao Zhou, Dr. Jiayan Zhang, Dr. Yang Shen, Dr. Tobias Bechgaard, Dr. Martin Østergaard, Dr. Rasmus Peterson, Dr. Usuma Naknikham, Dr. Katie Kedwell, Dr. Kacper Januchta, Dr. Malwina Stępniewska, Dr. Qiang Tao, Dr. Ming Liu, Dr. Theany To, Dr. Anil Kumar Suri, Dr. Fengchao Li, Dr. Qi Zhang, Dr. Tao Du, Mikkel Bødker, Katarzyna Janowska, Rasmus Madsen, Søren Sørensen, Anne Sophie Jødal, Johan Christensen, Pengfei Liu, Zhencai Li, Jiajia Yan, Linling Tan, Xinxin Chen, Xianzheng Ma, Wei Xu, Wei Fan, Xiangting Ren, Annemarie Davidsen, Anne Flensborg, Lisbeth Wybrandt, Timo Kirwa.

During my external study at Qilu University of Technology, I also had a great time working, because of many brilliant and supportive collaborators. I am very grateful to Prof. Jianxing Shen, Dr. Qiuju Zheng, Dr. Guangda Li, Dr. Shujiang Liu, Dr. Yuebo Hu, Dr. Tailin Wang, Dr. Chaofeng Zhu, Dr. Xue Wang, Peixing Wang,

Zhenjing Jiang, Peng Li for great help in both research and life when I study there. I also really enjoy working together with them and I would like to express my appreciation to all the researchers and scientists there. I hope they will enjoy their academic life and have a bright future. The experiences are so memorable that I will never forget the fantastic moments there.

I also appreciate my collaborators for their scientific assistance and helpful discussions, who are Assoc. Prof. Lars Jensen, Assoc. Prof. Deyong Wang from Aalborg University, Prof. Haizheng Tao, Dr. Zhaoyang Wang and Dr. Fangyu Xiong, Zijuan Du from Wuhan University of Technology. It is my great lucky to work with them. I also would like to thank for the support from China Scholarship Council. It provides me a great opportunity to conduct my research with many talent researchers and scientists.

Furthermore, I would personally give my tremendous appreciation to my lovely friends: Kanglu, Bin, Keke, Wenjie, Mingze, Wenfu, Na, Jimin, Fan, Kaiqi, Juan, Jinfeng, Tianbao, Baoze, Wenzhao, Guoqiang, Jianfang, Guohan, Fan, Haitao, Songda, Dunzhi, Chaopeng, Xin, Qin, Zexian, Fangcheng, Zhenkun, Zifeng, Jialing, Yuwei, Danfeng, Xinwei, Coco, Zhuo. This list goes on. It is lovely to have them around.

My great thanks go to my wife Miaomiao, my lovely daughter Jessie and my parents. I could not imagine how I would be without their encouragement and love. I survive from PhD study and I really appreciate their supports. I love all of you forever!

LIST OF ABBRIVATIONS

MOF	Metal-organic frameworks
CP	Coordination polymer
ZIF	Zeolitic imidazolate framework
MIL	MOFs named after Matériaux de l'Institut Lavoisier
PXRD	Powder X-ray diffraction
CIF	Crystallographic information files
DSC	Differential scanning calorimetry
TGA	Thermogravimetry
NMR	Nuclear magnetic resonance
SEM	Scanning electron microscopy
TEM	Transmission electron microscopy
FT-IR	Fourier-transform infrared spectroscopy
BET	Brunauer-Emmett-Teller method
XPS	X-ray phono spectroscopy
UV	Ultraviolet spectroscopy
CV	Cyclic voltammetry
GCD	Galvanostatic charge-discharge
EIS	Electrochemical impedance spectroscopy
LIBs	Lithium-ion batteries
Im	Imidazole
BIm	Benzimidazole
2-HmIm	2-Methylimidazole
BDC	Terephthalic acid; Benzene-1,4-dicarboxylic acid
DMF	*N*,*N*-Dimethylformamide
DEF	*N*,*N*-Diethylformamide
H_3BTB	4,4',4''-benzene-1,3,5-triyl-tri-benzoic acid
MeOH	Methanol
EtOH	Ethanol
GO	Graphene oxide
rGO	Reduced graphene oxide
T_g	Glass transition temperature

TABLE OF CONTENTS

TABLE OF SCHEME

TABLE OF FIGURES

CHAPTER 1. INTRODUCTION

1.1. BACKGROUND AND CHALLENGES

With the development of modern world, the sustainable development is becoming one of the ultimate goals for human society. To achieve that, renewable energy sources such as wind, tidal, solar, geothermal and biomass, have been regarded as the alternatives for traditional fossil fuel. However, these new energy sources are all inherently intermittent and generally dispersed compared to current isolated large-scale facilities. To manipulate these new energy sources optimally, energy storage technologies are urgently needed to store energy both at a large scale and low cost(1–3).

Since the first commercialization in 1991 by Sony Inc., lithium-ion batteries (LIBs) have been extensively investigated and utilized in recent years due to their merits such as high energy density, high cell voltage, long cycle life, low self-discharge rate, low maintenance and environmental friendliness, compared with traditional energy storage devices(4–7). As shown in Scheme 1-1, the LIBs consist of three important parts, i.e., two electrodes (anode and cathode), electrolyte and separator. During cell discharge, electrons transport from anode to cathode through an external circuit with a load of resistance. The lithium ions flow from anode into cathode inside the cell to convert chemical energy to electrical energy. During cell charge, the whole process is reversed by an external applied voltage and the electrical energy is converted back to chemical energy. For the cathode parts, $LiCoO_2$, $LiFePO_4$, $LiMn_2O_4$ and $LiNi_xCo_yMn_{1-x-y}O_2$ are common materials for practical LIBs(8–11). Carbonaceous materials and silicon-based materials are commercially available anode materials(12–16). Common electrolytes are lithium hexafluorophosphate ($LiPF_6$) salt dissolved in the mixture of carbonate solvents selected from carbonates including cyclic carbonates and linear carbonates(17).

However, the rapid development of large-scale smart grids, portable electronic devices and electric vehicles urgently demand better LIBs with higher energy density, longer cycle life, lower cost, and improved safety than current commercial ones. Therefore, the development of new electrode materials with higher capability for lithium storage, higher safety and lower cost has been attracting more attention in recent years.

Although many anode materials, such as silicon, transition metal oxide have been investigated, there are still a long way to put these materials into practice since their huge capacity loss, complex synthesis procedures, expensive raw materials, equipment, etc(18–22). Among these anode materials, metal-organic frameworks (MOFs) and their derivatives are one of the most promising anode candidates due to their simple preparation process, tunable structures, flexible chemical composition,

great porosity, and high surface area. Besides energy storage, MOFs also shows great potential for other applications, such as gas separation and storage, proton conduction, catalysis, drug delivery, sensor, etc(23–28).

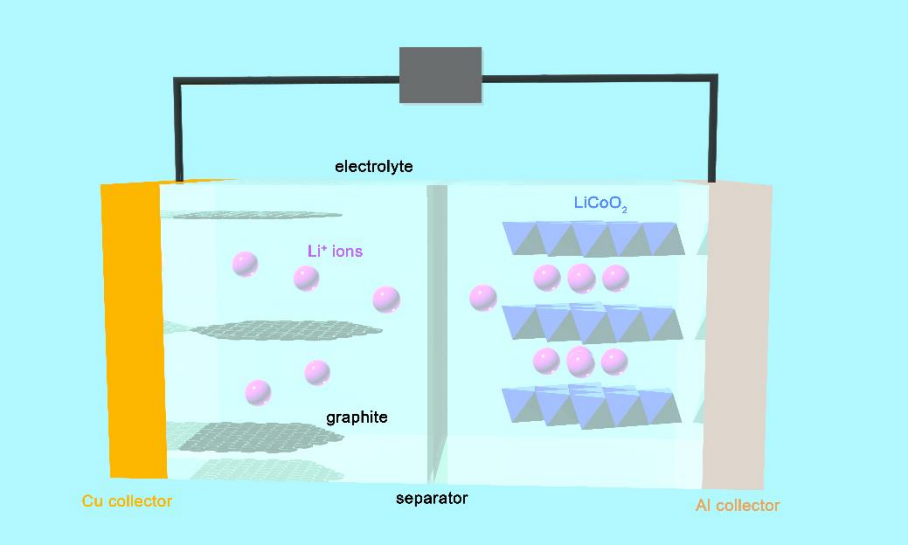

Scheme 1-1 Schematic illustration of the Li-ion battery. Anode part consists of copper current collector and graphite while cathode part includes aluminum current collector and $LiCoO_2$.

MOFs generally consist of metal ions/nodes and appropriate organic ligands, which was first reported by Yaghi and Li et al. in the 1990s(29). After that, a great number of MOFs constructed by different metal ions and organic ligands with variable interesting properties have been prepared and investigated in various research areas. Currently, more than 20 thousand MOFs with tunable structures and properties have been reported. Among these MOFs, some MOFs have been investigated as anode for LIBs and shows fascinating electrochemical performance. The first MOF tested as anode was reported in 2006, during which the MOF-177 ($Zn_4O(BTB)_2 \cdot (DEF)_m(H_2O)_n$) exhibited a capacity of 400 mAh g^{-1} during the first cycle and then the capacity decayed to 105 mAh g^{-1} in the second cycle(30). While other pristine MOFs were also investigated as anode materials, there are still some challenges faced by the MOFs that yet to be overcome, including poor electronic conductivity, weak structure stability, low reversible capacity(31–33). Furthermore, the lithium storage mechanism of MOFs is not fully understood, and the structure-performance relationship of MOFs is still not clear. Solving these problems will be helpful to design appropriate MOFs for better lithium storage. Moreover, understanding the structure-performance of MOFs might also contribute to developing other anode materials for better LIBs.

1.2. OBJECTIVES

The overall goal of this PhD project is to investigate the potential applications of MOFs as anode materials for LIBs, from aspects of capacity, cycling stability and structure-performance relationship.

The capacity of an active material is determined by the amount of lithium it could accommodate per formula unit. The cycling stability is the retention of the capacity after a certain number of charge-discharge cycles. These two properties are vital factors that determine the overall lithium storage performance.

The details of this project are summarized as below:

1. Develop a synthesis method to hybrid graphene sheets with MOFs to improve its electronic conductivity and the cycling stability towards charge-discharge processes.

2. Use MOFs as a matrix to accommodate guest molecules to improve its capacity toward lithium storage.

3. Utilize MOF glass and crystalline MOF to explore the structure-performance relationship of MOFs.

4. Investigate the potential of MOF glass and their derivatives for anode materials.

1.3. THESIS CONTENTS

The experiment works of this thesis were conducted at Aalborg University, Qilu University of Technology and Wuhan University of Technology. This thesis consists of three papers, of which two papers have been published in peer-reviewed journals, and one is submitted for publication. These three papers correspond to Chapter 3, Chapter 4, Chapter 5, and Chapter 6. These papers constitute the main body of the thesis, and will be referred to by their roman:

I. **Gao, C.**, Wang, P., Wang, Z., Kær, S. K., Zhang, Y., & Yue, Y., The disordering-enhanced performances of the Al-MOF/graphene composite anodes for lithium-ion batteries. *Nano Energy*, 65, 104032 (2019).

II. **Gao, C.**, Jiang, Z. J., Wang, P. X., Jensen, L. R., Zhang, Y. F., & Yue, Y., Optimized assembling of MOF/SnO_2/Graphene leads to superior anode for lithium-ion batteries. *Nano Energy*, 74, 104868 (2020).

III. **Gao, C.**, Jiang, Z. J., Wang, P. X., Jensen, L. R., Zhang, Y. F., & Yue, Y., Metal-organic framework glass anode with an unusual cycling-induced capacity enhancement for lithium-ion batteries (to be submitted).

CHAPTER 2. EXPERIMETAL

In this chapter, preparation methods and the characterization techniques of MOFs and other anode materials are presented.

2.1. SYNTHESIS

All the chemicals used for the synthesis are purchased from commercial companies and used without any purification unless specified. All syntheses were performed by the author in this thesis with assistance from other co-authors. All the structures of samples were verified by matching PXRD patterns with simulated ones and reported ones.

2.1.1. GRAPHENE OXIDE

The graphene oxide used in this thesis was prepared via a modified Hummers method(34–36). In detail, 92 mL H_2SO_4 (sulfuric acid, 98%) in a 1 L beaker was placed in an ice bath for 0.5 h to cool it completely. Then, 2.0 g graphite powder (Graphit Kropfmühl GmbH) was added to the acid slowly and then stirred for 0.5 h. Then, 2.0 g $NaNO_3$ was added slowly into the suspension and stirred for 0.5h. Then 12.0 g K_2MnO_4 was also added slowly to avoid any sudden temperature increase, which might cause exploration otherwise. After 0.5 h stirring, the beaker was moved to a water bath at 35 ℃ for 1 h and the suspension became dark green. Then, the temperature of the water bath was increased to 90 ℃ and kept for 1 h and then 160 mL deionized water slowly to maintain a steady temperature of the mixture. After 0.5 h, a dark brown paste was obtained and other 400 mL deionized water and 12 mL 30% H_2O_2 was added. The obtained light-yellow suspension was centrifugated and rinsed with dilute HCl (5%) to remove impurities, such as K^+, Mn^{2+}, sulfates, etc. Then the paste was washed with water to eliminate residue acid. After freeze drying for 48 h, dark yellow and fluffy graphene oxide (GO) powder was obtained. GO suspension could be prepared by disperse GO powder in deionized water with sonication for 4 h. GO could be reduced to rGO (reduced graphene oxdie) by various methods and rGO is noted as graphene for simplicity purposes.

2.1.2. AL-MOF

Al-MOF, whose formula is $Al(OH)[O_2C–C_6H_4–CO_2]$, was prepared as reported with slight modifications(37). In detail, aluminum nitrate nonahydrate (1.3 g, 3.5 mmol) and 1,4-Benzenedioic acid (0.288 g, 1.7 mmol) were dispersed into 30 mL deionized water. Then the obtained mixture was transferred to a 50 mL Teflon-lined high-pressure autoclave and heated at 220 ℃ for 3 days. After cooling down naturally to room temperature, white precipitation was collected by centrifugation and washed

several times with de-ionized water. The pristine Al-MOF was finally obtained after that the product was heat treated at 330 ℃ for 3 days to expel any trapped organic ligands.

2.2. CHARACTERIZATION METHODS

The author performed most of the experiments and analyzed all results in this thesis. A co-author contribution is presented in the relevant sections if the experiments or characterizations were not conducted by the author independently.

2.2.1. POWDER X-RAY DIFFRACTION (PXRD)

PXRD patterns of all samples were collected with PANalytical X-ray diffraction meters in Aalborg University and Qilu University of Technology with Cu Kα ($\lambda = 1.5406$ Å) radiation during the 2θ range of 5-60° with a step size of 0.013°. All samples were finely grinded before measurement. Simulated PXRD patterns were obtained from Software Mercury 3.8 from the crystallographic information files (CIF) of corresponding framework structures or standard X-ray diffraction patterns of corresponding materials. Analysis of the results was carried out using the X'pert HighScore Plus.

2.2.2. RANMAN SOECTROSCOPY

Raman spectra of all samples were collected from a HORIBA LabRAM HR Evolution Raman microscope excited by a 532 nm laser and a Renishaw In-Via Raman microscopic with an Ar^+ laser (λ = 785 nm) at 50 × aperture in Aalborg University and Wuhan University of Technology. The wavelength of incident laser is 532 nm and a power of 0.1 W was used to record the Raman shift within the range from 200 to 2000 cm^{-1}. All samples were tested for three times for error reduction. Raman spectra were collected with help from Dr. L.R. Jensen from Department of Materials and Production, AAU, and Dr. Zhaoyang Wang from Wuhan University of Technology.

2.2.3. ATTENUATED TOTAL REFLECTION FOURIER TRANSFORM INFRARED SPECTROSCOPY (ATR-FTIR)

Attenuated Total Reflection Fourier transform infrared (ATR-FTIR) spectra of all samples were recorded from a Bruker TENSOR II FTIR spectrometer in Aalborg University with Platinum ATR Accessory at room temperature within the range of 400–4000 cm^{-1}. Baselines were recorded before each tests and the samples were placed directly on the crystal sample holder for data collection. All samples were tested for three times for error reduction.

2.2.4. THERMOGRAVIMETRY

Thermogravimetric (TG) curves of all samples were collected from a Thermogravimetric Analyzers Discovery and a Netzsch STA 449 F1 Jupiter in Aalborg University. The masses of samples were recorded when they were heated from room temperature to target temperature with a rate of 10 ℃ min^{-1} under N_2 protection or in air atmosphere.

2.2.5. DIFFERENTIAL SCANNING CALORIMETRY (DSC)

Differential scanning calorimetric curves of all samples were collected simultaneously with Netzsch STA 449 F1 Jupiter in Aalborg University. Pt/Rh crucibles were used for both samples and the references. The sample mass was normally about 15 mg. The direction of the enthalpy release, i.e., exothermic direction, points downwards in all figures in this thesis. Scanning rate was 10 K min^{-1} as default and samples were heated from 200℃ to target temperature under N_2 or Argon atmosphere. Baselines were collected within the same temperature range and under same temperature rates before each test.

2.2.6. X-RAY PHOTOELECTRON SPECTROSCOPY (XPS)

X-ray Photoelectron Spectroscopy (XPS) was conducted to investigate the surface chemistry of samples by using ESCALAB 250Xi spectrometer (ThermoFisher Scientific, USA) with non-monochromatic Al Ka X-ray (1486.6 eV) at pass energy of 50 eV from Qilu University of Technology and Wuhan University of Technology with the help of Peixing Wang, Zhenjing Jiang and Dr. Zhaoyang Wang. The survey spectra and high-resolution spectra of specific elements were collected for all samples. The peaks were deconvoluted via XPSPEAK and Origin.

2.2.7. N_2 ADSORPTION MEASUREMENT

N_2 adsorption measurements were conducted to study the surface area and pore size of samples. N_2 adsorption-desorption isotherms were obtained at 77 K with an ASAP 2020 Accelerated Surface Area and Porosimetry System. All samples (around 100 mg) were degassed at 200 ℃ for 1h to before measurements. Brunauer-Emmett-Teller (BET) and Barrett-Joyner-Halenda (BJH) analysis were also applied to calculate the specific surface area, and the corresponding pore size distribution.

2.2.8. SCANNING ELECTRON MICROSCOPY (SEM)

Scanning electron microscopy (SEM) images were obtained from a Zeiss EVO 60 SEM and a Zeiss Gemini SEM 500 with secondary electron mode in Alborg University and Qilu University of Technology to investigate the morphology of

samples. All samples were vacuum dried at 120 ℃ and then pasted onto the conductive gel before testing.

2.2.9. TRANSMISSION ELECTRON MICROSCOPY (TEM)

Transmission Electron Microscopy (TEM) images of all samples were collected from a JEM-2100F (JEOL Ltd., Japan) in Qilu University of Technology with scanning TEM mode to observe their morphology and element distribution. Samples were dispersed in ethanol and ultrasonicated for 30 min, and then drop cast to copper mesh before TEM measurements.

2.2.10. DIFFUSE REFLECTANCE ULTRAVIOLET–VISIBLE SPECTROSCOPY

Diffusion reflectance ultraviolet-visible spectra within the range 200–800 nm were collected from a UV-visible Spectrophotometer in Aalborg University, PerkinElmer Lambda 1050 (Waltham, MA, USA), with an integrating sphere using standard $BaSO_4$ as a reference material. The band gap energy was calculated from the Tauc plot of the Kubelka-Munk (K-M) function(38):

$$(\alpha h\nu)^{1/2} = C(h\nu - E_g)$$

in which α is the absorption coefficient of the samples, h is the Planck's constant, ν is the frequency of incident beam, C is a proportionality constant, and E_g is the band gap energy of the sample.

2.3. ELECTROCHEMICAL METHODS

The electrochemical performances of all samples as anode were evaluated by using CR2032 coin-type cells with lithium foil (diameter of 10 mm) as the counter/reference electrode. The working electrodes were prepared by pasting a slurry composed of 70 wt% active materials, 20 wt% acetylene black and 10wt% polyvinylidene difluoride (PVDF) onto a copper foil substrate (diameter of 12 mm) and then dried at 110 ℃ in a vacuum oven overnight. The loading of active materials is 1-2 mg, based on which the specific capacities were calculated. The electrolyte is 1 M $LiPF_6$ in ethylene carbonate (EC)/diethyl carbonate (DEC)/ dimethyl carbonate (DMC) (1:1:1 vol%) and the separator is a Celgard 2325 membrane (diameter of 19.0 mm). The cells were assembled in an Argon-filled glovebox with both the moisture and oxygen content below 1 ppm and kept for 24 h before testing at 25 ℃. Some of the electrochemical measurements were conducted with the help of Peixing Wang and Zhenjing Jiang from Qilu University of Technology.

2.3.1. CYCLIC VOLTAMMETRY

Cyclic Voltammetry (CV) curves of samples were recorded to study the lithium storage mechanism in active materials at a scan rate of 0.1 mv s^{-1} in the range from 0.01 to 3 V on a CHI 760e electrochemical working station. The first three cycles were recorded.

Generally, the total stored charge originated from three components: the faradaic contribution from the Li^+ ions insertion/extraction process (the diffusion capacity), the faradaic contribution from the charge transfer process with surface atoms (referred to as pseudocapacitance)(39,40), and the nonfaradaic contribution from the double-layer effect. The capacitive effects (pseudocapacitance and double-layer effect) could be characterized by analysing CV curves at various scan rate according to the following equation(40):

$$i(V) = av^b$$

in which the measured current $i(V)$ obey a power law relationship with the sweep rate v. Both a and b are adjustable parameters, with b-values determined from the slope of the plot of log i vs log v. There are two well-confined conditions: $b = 0.5$ and $b = 1$. In detail, $b = 0.5$ represents a diffusion-controlled process, i.e., lithiation insertion process whereas $b = 1$ stands for the capacitive effects, i.e., capacitive process is dominant. The b-value between 0.5 and 1 suggests the mixed contribution from both diffusion-controlled processes and capacitive effects. By plotting log i vs. log v, b-values can be determined from the slopes. The total capacitive contribution at a given scan rates (v) can be divided into two fractions (the diffusion-controlled fraction $k_2v^{1/2}$ and capacitive contribution k_1v) at a fixed potential (V) according to the following equation(41):

$$i(V) = k_1v + k_2v^{\wedge 1/2}$$

which could be rearranged to

$$i(V)/v^{\wedge 1/2} = k_1v^{\wedge 1/2} + k_2$$

where k_1 and k_2 can be evaluated by plotting $i(V)/v^{\wedge 1/2}$ vs. $v^{\wedge 1/2}$. After determining the k_1 and k_2, the total capacitive contributions and total stored charge of samples could be calculated.

2.3.2. GALVANOSTATIC CHARGE-DISCHARGE

Galvanostatic Charge-discharge (GCD) measurements were carried out to evaluate the capacity, cycling stability and rate capability of materials for LIBs. All samples were cycled during the voltage range from 0.01 to 3 V with different current densities

for different cycles. The specific capacities of materials were calculated based on their weight and the Coulombic efficiencies of charge-discharge processes were also recorded. Besides, galvanostatic charge-discharge voltage profiles were also obtained to study the lithium insertion/extraction mechanism of electrode materials.

2.3.3. ELECTROCHEMICAL IMPEDANCE SPECTROSCOPY

Electrochemical Impedance Spectroscopy (EIS) plots of all coin cells were collected to within the frequency range from 0.01 to 100 kHz with an amplitude of 10 mV. By the analysis of impedance data and equivalent circuit modelling, the resistance (R_e, bulk resistance and R_{ct}, charge transfer resistance), capacitance and other interface information could be obtained.

For some samples, the Li^+ ions diffusion coefficient (D) was derived from EIS plots via following equation:

$$D=R^2T^2/\ 2A^2n^4F^4C^2\sigma^2$$

in which R is the gas constant, T is the absolute temperature, A is the surface area of the electrode, n is the number of electron transferred during the redox reaction, F is the Faraday constant, C is the Li^+ concentration, and σ is the Warburg factor associated with Z_{re} (Z_{re} α $\sigma\omega^{-1/2}$), which could be obtained by linear fitting between Z_{re} and the reciprocal square root of the angular frequency ω. Then, the apparent Li^+ diffusion coefficient D could be calculated from above equation.

CHAPTER 3. PREPARATION AND CHARACTERIZATION OF MOF-BASED COMPOSITE

3.1. AL-MOF/GRAPHENE

3.1.1. PREPARATION OF AL-MOF/GRAPHENE

To prepare the Al-MOF/graphene composite, 285 mg pristine Al-MOF powder was first dispersed in 30 mL graphene oxide (GO) aqueous suspension (0.5 mg mL^{-1}) and stirred for 0.5 h. After adding 60 mg Vitamin C, the above mixture then was heated at 90 ℃ for 1 h. Finally, the black Al-MOF/graphene paste was separated by centrifugation and then dried in a vacuum oven at 120 ℃ overnight. For simplicity, reduce graphene oxide (rGO) is noted as graphene in this thesis. The weight percentage of graphene in the composite is estimated to be 5% in order to obtain the best performance according to previous report(42). For comparison, MOFs based on other metals (Fe, Co, Ni) were also prepared according to literatures.

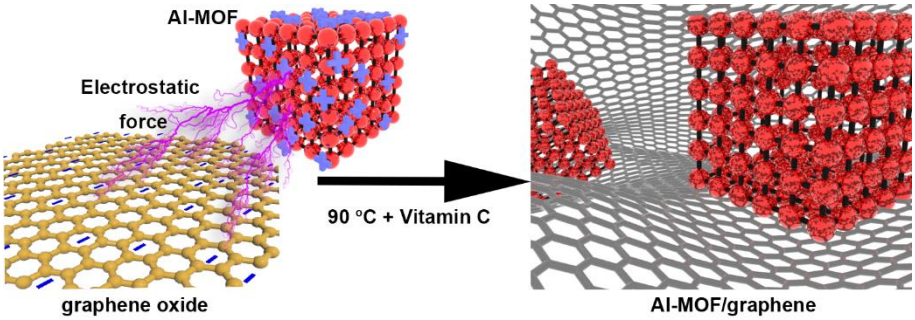

Scheme 3-1 Schematic representation of preparation procedures of the Al-MOF/graphene composite. The "+" and "-" symbols on the surface of Al-MOF and GO in the scheme represent positive or negative charges on their surfaces.

The preparation process is briefly illustrated in Scheme 3-1. Confirming by Zeta potential measurements, the Al-MOF carry positive charges on its surface (15.6 mV). While, GO bears negative charges (-44.7 mV), which originate from oxygen-contained function groups on its surface. These positive and negative charges are represented as "+" and "-" symbols in the scheme, respectively. Owing to the strong electrostatic force between these two components, GO and Al-MOF tend to aggregate and form the Al-MOF/GO precursor through a self-assembly process. Then, Vitamin C is used to reduce GO to rGO (which is noted as graphene) at elevated temperature and the Al-MOF/graphene composite is obtain after centrifugation and vacuum dry.

3.1.2. CHARACTERIZATION OF AL-MOF/GRAPHENE

The as-prepared Al-MOF/graphene composite was characterized with SEM, TEM, XRD, Raman, FTIR, BET, XPS, UV-vis to investigate its structure and components. Detail information could be found in paper I.

3.1.2.1 Morphology of Al-MOF and Al-MOF/graphene

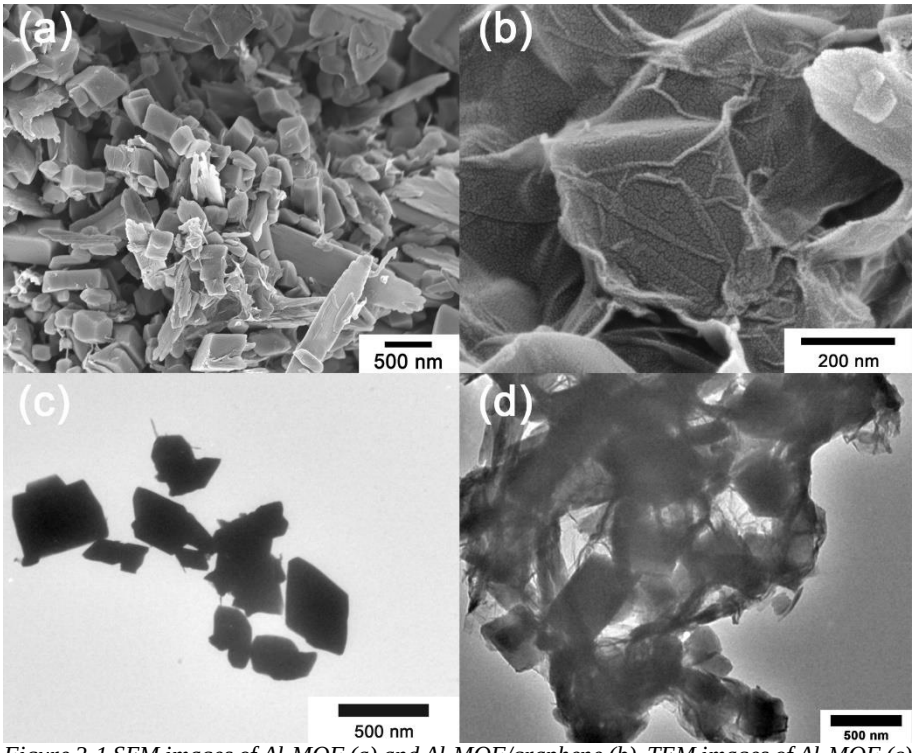

Figure 3-1 SEM images of Al-MOF (a) and Al-MOF/graphene (b). TEM images of Al-MOF (c) and Al-MOF/graphene (d).

The morphologies of Al-MOF and Al-MOF/graphene were determined by SEM and TEM. As shown in Figure 3-1, the Al-MOF particles possess irregular shapes with size range from 100 nm to micrometers. After hybridized with graphene sheets, pristine Al-MOF particles are wrapped by silk-like graphene sheets, confirming that the successful assembly of Al-MOF particles and graphene sheets. In addition, Al-MOF in the composite still present similar profiles as that of pristine MOF, suggesting that it remains intact against Vitamin C reduction and heat treatment. However, MOFs based on Co and Ni decomposed directly when dispersed in water and Fe based MOF collapsed during the Vitamin C reduction process. This decomposition could be also verified by their XRD patterns after the reduction process.

3.1.2.2 XRD patterns

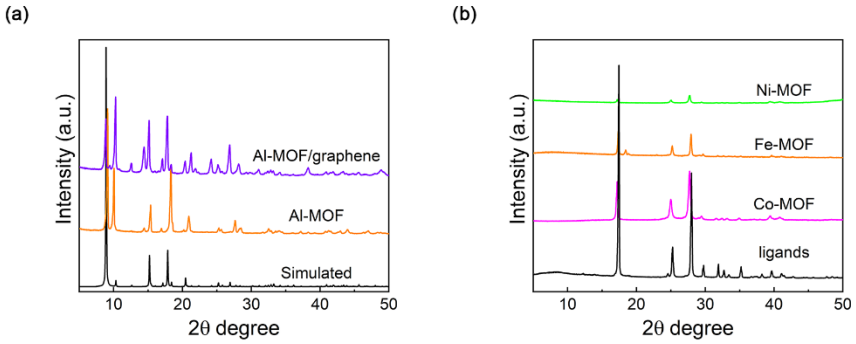

Figure 3-2 (a) XRD patterns of simulated Al-MOF, as-prepared Al-MOF and Al-MOF/graphene. (b) XRD patterns of Fe-MOF, Co-MOF, Ni-MOF after hybridization with graphene and organic ligand (1,4-terephthalic acid).

As shown in Figure 3-2a, both Al-MOF and Al-MOF/graphene composite displays diffraction peaks at 8.9, 10.3, 15.1, 17.9 and 20.5 degree, which match well with those of the simulated Al-MOF pattern(37). This agreement proves that the successful preparation of Al-MOF and the Al-MOF retain its crystal structure after hybridization with graphene sheets, which also suggests the excellent structural stability of Al-MOF. Other diffraction peaks apart from those assigned to Al-MOF in the patterns mainly originate from other two crystal form of Al-MOF with water molecules or no guest molecules trapped inside the pores of MOF(37,43). In Figure 3-2b, the patterns of Fe-MOF, Co-MOF, Ni-MOF after hybridization with graphene only present diffraction peaks that belong to the organic ligands, which suggests that these MOFs decompose during the reduction and heat treatment processes. This destruction might be caused by the reduction of metal nodes by Vitamin C, after which the whole MOF structure is destroyed completely.

3.1.2.3 Raman spectra

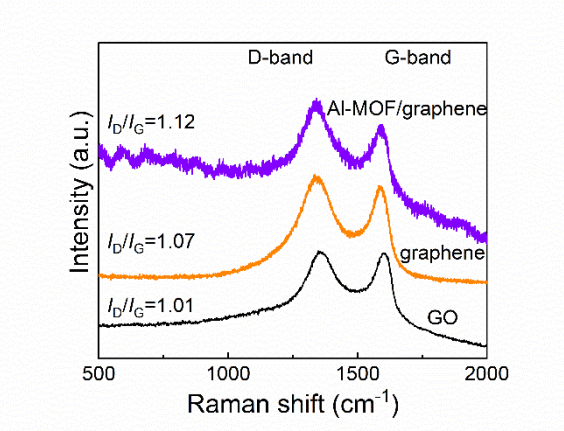

Figure 3-3 Raman spectra of Al-MOF/graphene, GO and graphene.

The Raman spectra of the Al-MOF/graphene composite, GO and graphene exhibit two main bands at 1350 cm^{-1} (D-band, disorder carbon) and 1590 cm^{-1} (G-band, graphite lattice), respectively. These two bands originate from the breathing mode of κ-point phonons of A_{1g} symmetry and the E_{2g} phonon of sp^2 hybridized C atoms, respectively(44). In general, the peak intensity ratio (I_D/I_G) of two bands could be regarded as the degree of the lattice distortion of graphene sheets. Obviously, the Al-MOF/graphene composite exhibits the largest I_D/I_G ratio (1.12) than those of graphene (1.07) and GO (1.01), demonstrating that more defects were induced after the anchoring of Al-MOF particles and the reduction process. The increased I_D/I_G ratio could also suggest that the Al-MOF particles are attached onto the surface of graphene sheets.

3.1.2.4 Fourier-transform infrared spectra

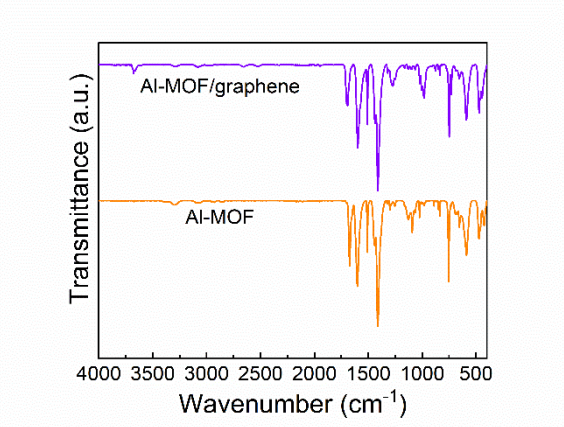

Figure 3-4 Attenuated Total Reflection Fourier-transform infrared spectra of Al-MOF and the Al-MOF/graphene composite.

ATR-FTIR spectra of Al-MOF and Al-MOF/graphene were also recorded at room temperature during the range from 400 to 2000 cm^{-1}. As displayed in Figure 3-4, these two samples share virtually the same patterns. Two absorption bands at 1602 and 1508 cm^{-1} correspond to the $-CO_2$ asymmetric stretching and the strong band at 1410 cm^{-1} could be assigned to the $-CO_2$ symmetric stretching. These $-CO_2$ groups mainly originate from organic ligands that coordinated with Al^{3+} nodes in the Al-MOF. The extra band at 1673 cm^{-1} might be attributed to the guest ligand molecules trapped inside pores of the MOF in the protonate form ($-CO_2H$). These results confirm that the organic ligands remain unaffected after reduction and heat treatment process.

3.1.2.5 X-ray photoelectron spectra

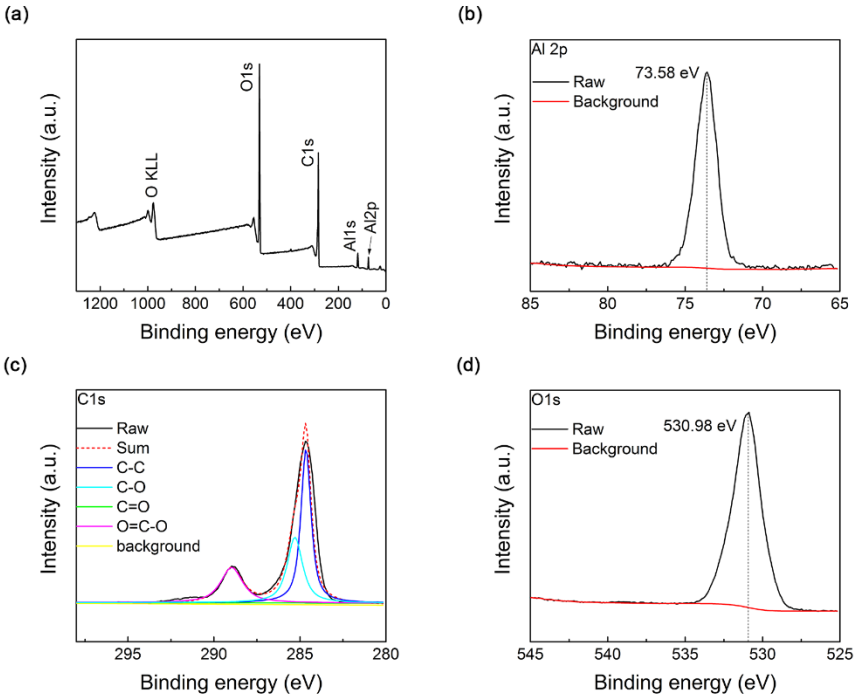

Figure 3-5 (a) XPS survey spectrum of Al-MOF/graphene. High-resolution spectra for (b) Al 2p, (c) C 1s and (d) O 1s.

The surface composition of Al-MOF/graphene was further investigated by XPS. The survey spectrum in Figure 3-5a shows obvious Al 2p, C 1s and O 1s peaks, whose high-resolution spectra are also displayed in Figure 3-5. The peak of Al 2p locates at the binding energy of 73.6 eV, proving the valance state of Al^{3+} remain unchanged after the reduction process. The C 1s spectrum demonstrates two obvious peaks at 284.7 and 288.9 eV, which could be deconvoluted into four peaks at 284.6, 285.9, 287.3 and 288.8 eV corresponding to C–C, C–O, C=O and O=C–O, respectively(45). In the meantime, the O 1s peak at 531.7 eV also suggests the presence of O=C–O group. These results confirm that the existence of oxygen-contained functional groups, which might originate from both organic ligands and residue functional groups on the surface of graphene.

3.1.2.6 Diffuse reflectance ultraviolet-visible spectra

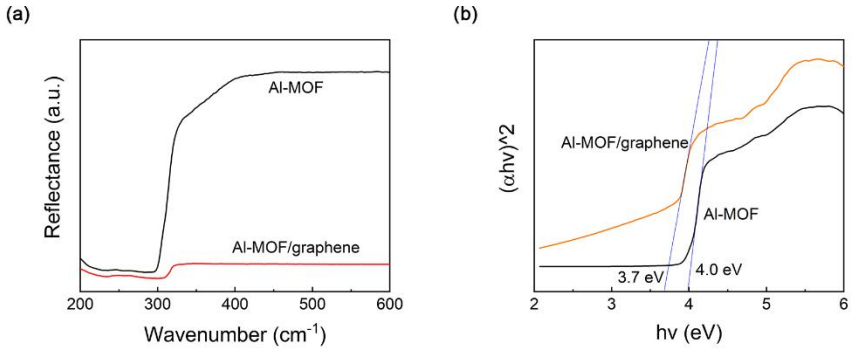

Figure 3-6 (a) Diffuse reflectance ultraviolet-visible spectra of Al-MOF and Al-MOF/graphene. (b) Tauc plots of Al-MOF and Al-MOF/graphene.

As shown in Figure 3-6a, the Al-MOF/graphene presents a much lower reflectance than Al-MOF. This low reflectance might originate the black color of this composite after hybridization with graphene sheets. The band gap of Al-MOF and Al-MOF/graphene were derived as presented in Figure 3-6a. A smaller bang gap of the Al-MOF/graphene (3.7 eV) than that of Al-MOF (4.0 eV) could contribute a better electronic conductivity of this composite compared with pristine Al-MOF.

3.2. TIN DIOXIDE@AL-MOF/GRAPHENE

3.2.1. PREPARATION OF TIN DIOXIDE@MOF/GRAPHENE

The SnO_2@MOF precursor was prepared by a wet impregnation method inspired by previous reports(46,47). Specifically, 100 mg pristine Al-MOF powder was dispersed homogeneously in 200 mL deionized water by vigorous stirring for 12 h. Then dissolving 1350 mg $SnCl_2{\cdot}2H_2O$ in the mixture and stirring for 72 h to make the complete transformation from $SnCl_2{\cdot}2H_2O$ to nano SnO_2 particles (897 mg SnO_2 would be obtained if the yield is 100%). The SnO_2@MOF was obtained after washing and drying of the above mixture. Then 285 mg of the as-prepared SnO_2@MOF precursor was dispersed in 30 mL GO aqueous dispersion (0.5 mg mL^{-1}) and 120 mg VC was added after stirring for 0.5 h. Then the obtained dispersion was stirred for another 0.5 h and kept in an oven at 90 ℃ for 1 h. The final SnO_2@MOF/graphene composite was obtained after centrifugation and drying under vacuum. The SnO_2 particles were also prepared without MOF. In addition, the mechanical mixture of SnO_2 and MOF was also prepared via grinding for comparison.

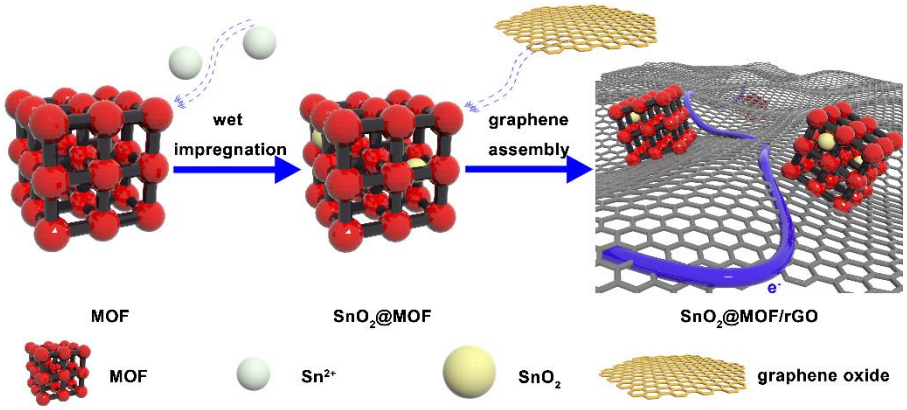

Scheme 3-2 Schematic representation of self-assembly process of the SnO_2@MOF precursor and the SnO_2@MOF/graphene composite (The blue line in SnO_2@MOF/graphene represents the electron transport path in this composite)(48).

The self-assembly process of the SnO_2@MOF/graphene composite is schematically presented in Scheme 3-2. The SnO_2 nano particles were packed into MOF via a wet impregnation process and then the SnO_2@MOF precursor was wrapped by graphene sheets through a self-assembly process. In detail, pristine MOF particles were dispersed in deionized water. Then, Sn^{2+} ions diffused into the pores of MOF driven by both capillary force and the electrostatic force during the wet impregnation process. Then Sn^{2+} ions were oxidized to SnO_2 with the pores of MOF acting as template to control the size of nano SnO_2 nano particles. Then the composite was rinsed with water several times to remove unreacted $SnCl_2{\cdot}2H_2O$ and SnO_2 on the surface of MOF. The SnO_2@MOF precursor was obtained after vacuuming dry. To obtain SnO_2@MOF/graphene composite, a similar self-assembly method was adopted as that of Al-MOF/graphene, during which the SnO_2@MOF was attached onto GO sheets via electrostatic force. After the reduction of GO to graphene sheet by Vitamin C, SnO_2@MOF/graphene composite was collected after centrifugation and drying.

3.2.2. CHARACTERIZATION OF TIN DIOXIDE@MOF/GRAPHENE

The as-prepared SnO_2@MOF precursor and SnO_2@MOF/graphene composite were characterized with SEM, TEM, XRD, Raman, FTIR, TG, XPS and BET to study their structures and components.

3.2.2.1 Morphology of SnO_2@MOF and SnO_2@MOF/graphene

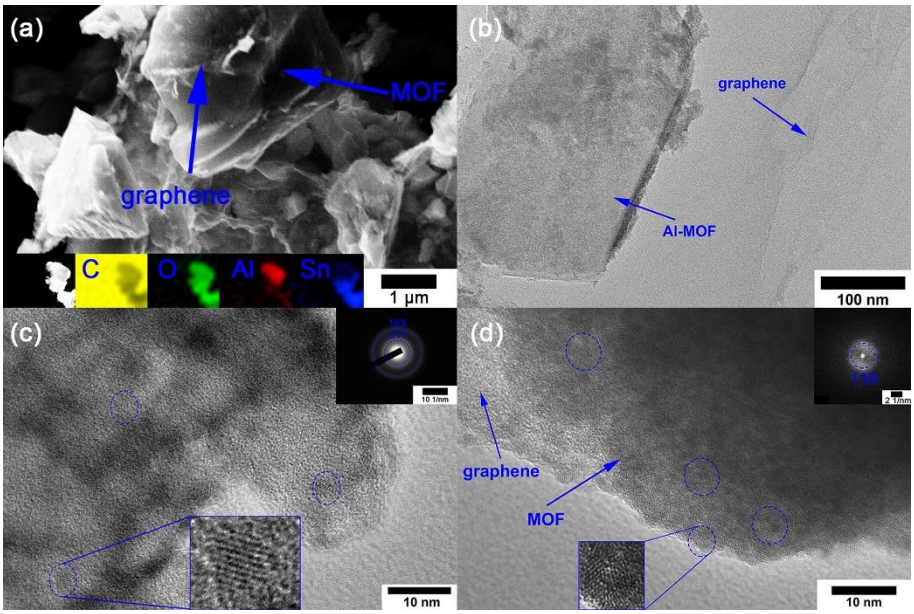

Figure 3-7 (a) SEM image and (b) TEM image of the SnO_2@MOF/graphene composite. (Inset: EDS elemental mappings of C, O, Al and Sn). HRTEM images of SnO_2@MOF (c) and SnO_2@MOF/graphene (d). (Insets ae selected area electron diffraction images of SnO_2@MOF and SnO_2@MOF/graphene, respectively.)

SEM and TEM images of the SnO_2@MOF precursor and the SnO_2@MOF/graphene composite were shown in Figure 3-7. Observed in SEM image, the SnO_2@MOF/graphene composite presents cuboid MOF particles with size of about 1 μm and silk-like graphene sheets covering the MOF particles. In addition, the uniform distribution of C, O, Al, Sn is confirmed by the EDS elemental mappings of the SnO_2@MOF/graphene composite. HRTEM images of SnO_2@MOF and SnO_2@MOF/graphene provide more detailed information about the size and distribution of SnO_2 nano particles. It could be noticed that SnO_2 nano particles (< 5 nm) are embedded inside MOF matrix, as indicated by the blue circles in Figure 3-7 c and d. A lattice fringe of 0.33 nm and diffraction rings including (103), (211) and (110), could be clearly noticed in the HRTEM images of SnO_2@MOF and SnO_2@MOF/graphene, which might be ascribed to rutile-like SnO_2. Above results verify that SnO_2 nano particles were trapped inside MOF as designed, which indicate that the MOF could function as a template for SnO_2 growth during the wet impregnation process., The SnO_2 nano particles could also be sheltered by both MOF matrix and graphene sheets from pulverization after the hybridized with graphene when used as anode materials for LIBs.

3.2.2.2 XRD patterns

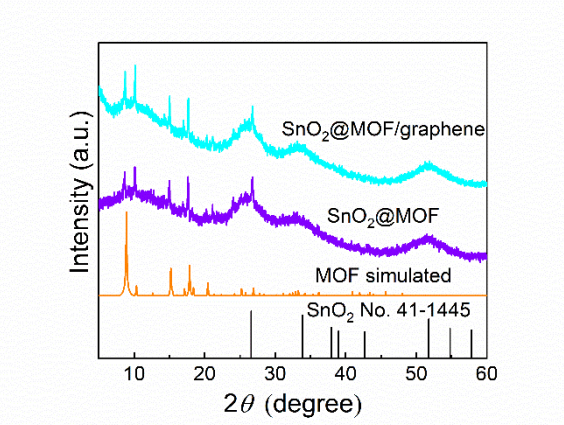

Figure 3-8 XRD patterns of simulated MOF, as-prepared SnO_2, SnO_2@MOF precursor and SnO_2@MOF/graphene composite.

As shown in Figure 3-8, both SnO_2@MOF precursor and SnO_2@MOF/graphene composites display sharp diffraction peaks at 8.9, 10.3, 15.2, 17.8, 26.7 degree, which could be indexed to that of pristine MOF, confirming that the crystal structure of MOF could be retained even after implanting of SnO_2 nano particles. Moreover, the broad peaks at 26.5, 33.8 and 51.7 degree originate from (110), (101), and (211) crystal planes of tetragonal rutile-like SnO_2 (JCPDS No. 41–1445)(49). No peaks of impurity such as SnO or $SnCl_2{\cdot}2H_2O$ could be noticed, suggesting the complete transformation from $SnCl_2{\cdot}2H_2O$ to SnO_2. The average crystal size of the SnO_2 nano particles was calculated to be around 2 nm according to the Scherrer equation, which is consistent with the HRTEM results.

3.2.2.3 Raman spectra

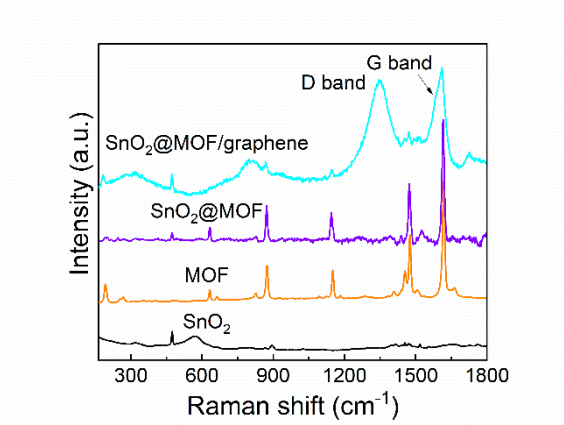

Figure 3-9 Raman spectra of as-prepared SnO_2, pristine MOF, SnO_2@MOF precursor and SnO_2@MOF/graphene composite.

Raman spectra of as-prepared SnO_2, MOF, SnO_2@MOF and SnO_2@MOF/graphene were also collected to investigate their structures. Confirmed by Figure 3-9, the Raman spectrum of the as-prepared SnO_2 displays a sharp peak at 474 cm^{-1}, which could be assigned to the E_g mode of SnO_2 nanoparticles. The broad peak at around 575 cm^{-1} mainly originates from the band *S1* because of disorder activation(50). The characteristic peaks at 192, 631, 872, 1150, 1472 and 1615 cm^{-1} in the spectra of SnO_2@MOF and SnO_2@MOF/graphene match well with those of pristine MOF. In addition, the peak at 474 cm^{-1} suggests the presence of SnO_2 in SnO_2@MOF and SnO_2@MOF/graphene. The SnO_2@MOF/graphene composite also displays two broad bands at 1350 and 1590 cm^{-1} that originate from the structural defects of graphene sheets and the first order scattering of the E_{2g} mode, respectively, which suggest the tight combination between the SnO_2@MOF precursor and graphene sheets(45).

3.2.2.4 Fourier-transform infrared spectra

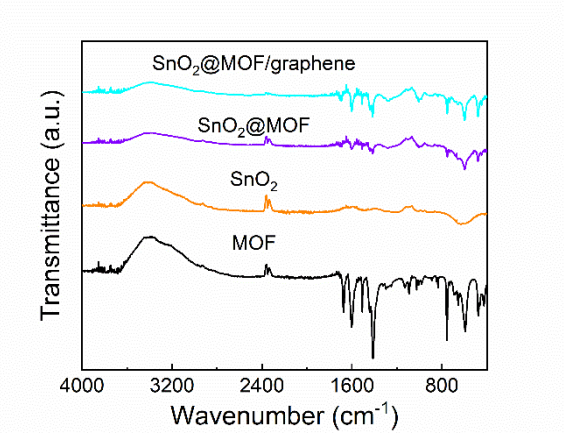

Figure 3-10 FTIR spectra of as-prepared SnO_2, pristine MOF, SnO_2@MOF and SnO_2@MOF/graphene collected from 400 to 4000 cm^{-1}.

Fourier transform infrared (FTIR) spectra of as-synthesized SnO_2, pristine MOF, SnO_2@MOF and the SnO_2@MOF/graphene composite were collected to gain more information about their structures. As seen in Figure 3-10, both the SnO_2@MOF and SnO_2@MOF/graphene present similar peaks as that of MOF, confirming that they contain same functional groups. Besides, they also present characteristic bands at about 1600, 1500 and 1410 cm^{-1}, which are ascribed to asymmetric and symmetric stretching of carboxyl groups from the organic ligands (-CO_2). In addition, a broad band at around 620 cm^{-1} could also be noticed in the spectra of SnO_2@MOF and SnO_2@MOF/graphene, which originates from the antisymmetric Sn–O–Sn stretching(51). Above results suggest the presentence of SnO_2 in both SnO_2@MOF precursor and SnO_2@MOF/graphene composite.

3.2.2.5 Thermalgravimetric Analysis

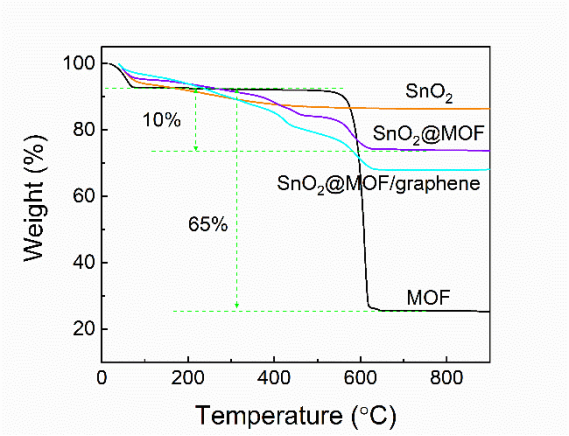

Figure 3-11 Thermogravimetry curves presenting mass changes of as-prepared SnO_2, MOF, SnO_2@MOF and SnO_2@MOF/graphene when heated from room temperature to 900 ℃ with a heat rate of 10 ℃ min^{-1} in air.

Thermogravimetry (TG) curves of the as-prepared SnO_2, pristine MOF, SnO_2@MOF and SnO_2@MOF/graphene were gathered to determine the weight retention rate of SnO_2 in the SnO_2@MOF as a function of temperature. As shown in Figure 3-11, the as-prepared SnO_2 possesses a high thermal stability to 900 ℃ except the initial mass loss. The TG curve of pristine MOF presents two main thermal events during the heating process. The initial mass loss of 8% from room temperature to about 100 ℃ is related to the loss of guest molecules, such as absorbed water and unreacted organic ligands inside pores of MOF. Another mass loss of about 65% takes place at about 600 ℃, which stems from the decomposition of MOF. As expected, the SnO_2@MOF/graphene composite demonstrates similar mass loss events as SnO_2@MOF. The mass losses below 400 ℃ is related to the expulsion of guest molecules from MOF and the sharp mass loss at about 600 ℃ is associated with the decomposition of MOF, implying the existence of MOF in both SnO_2@MOF and SnO_2@MOF/graphene. After this sharp mass drop, no obvious thermal events could be noticed, and the remaining mass belongs to the remained SnO_2. By calculating the mass loss percentage of MOF and SnO_2@MOF, the SnO_2 account for about 85% mass in the as-prepared SnO_2@MOF composite, while the designed weight percentage is 90%.

3.2.2.6 X-ray photoelectron spectra

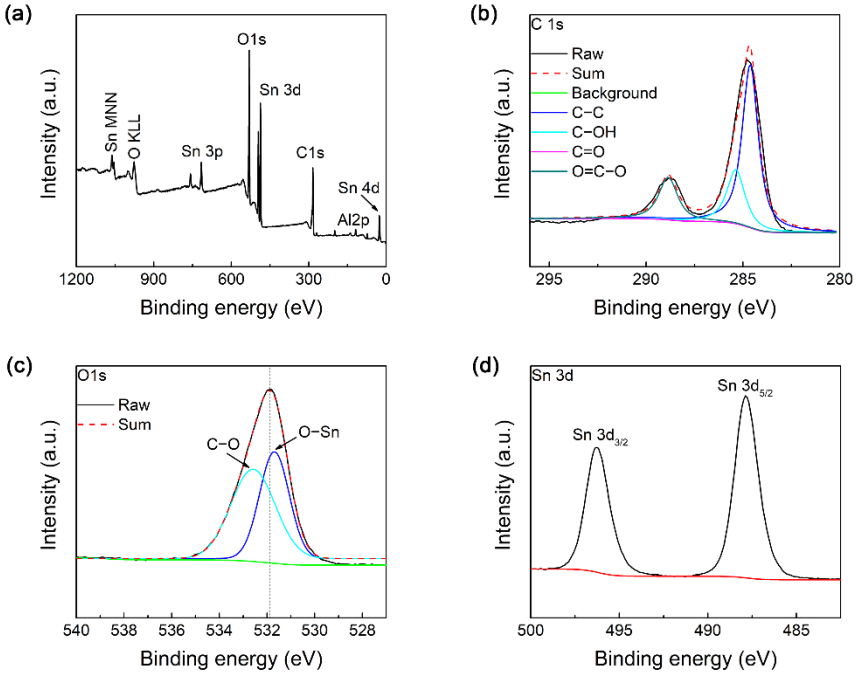

Figure 3-12 XPS survey spectrum (a), and core level spectra of C 1s (b), O 1s (c) and Sn 3d of the SnO_2@MOF/graphene.

X-ray photoelectron spectra were collected to investigate the surface composition of the SnO_2@MOF/graphene composite. As displayed in Figure 3-12, C, O, Al and Sn elements could be detected in the SnO_2@MOF/graphene composite. As for the high-resolution spectrum of C 1s， the strong bands at 284.9 and 288.9 eV were deconvoluted into four peaks (284.8, 285.6, 286.6 and 288.9 eV), matching well with C–C, C–OH, C=O, and O=C–O functional groups, respectively (45). The graphitic carbon mainly originates from graphene sheets, while the oxygen-contained groups stem from the organic ligands. In the meantime, the pronounced O 1s peak could also be deconvoluted into two peaks at 531.6 eV and 532.6 eV, which are related to the carboxyl groups of organic ligands and SnO_2, respectively (52). As for the high-resolution spectrum of Sn 3d, two distinct peaks at binding energies of 487.8 and 496.2 eV correspond to Sn $3d_{5/2}$ for Sn $3d_{3/2}$, respectively. This binding energy difference of 8.4 eV agrees with that previous reports of SnO_2, confirming valence of Sn^{4+}(53). The above XPS results suggest that the SnO_2@MOF/graphene composite consists of three main components, i.e., SnO_2, MOF and graphene.

3.2.2.7 N_2 adsorption-desorption isotherm

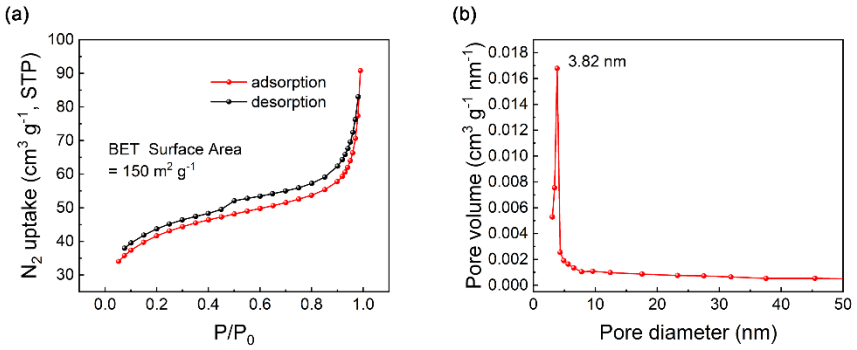

Figure 3-13 (a) N_2 adsorption-desorption isotherm and (b) Pore width distribution curve of the SnO_2@MOF/graphene composite.

To determine the specific surface area, a N_2 adsorption-desorption experiment on the SnO_2@MOF/graphene composite was conducted after the composite was degassed at 200 °C. As shown in Figure 3-13a, the composite displays a typical type IV isotherm with slight hysteresis upon desorption, which is a main characteristic of mesoporous materials. This result is further supported by the pore width distribution plot, which shows that the most probability pore size is 3.82 nm. The Brunauer–Emmett–Teller (BET) surface area of the composite is calculated to be 150 m^2 g^{-1}, which is much smaller than that of pristine MOF (1112 m^2 g^{-1}). The total pore volume of pristine MOF also decreases from 0.18 to 0.14 m^3 g^{-1} after impregnation process. These sharp declines of surface area and pore volume could confirm that the pores of MOF are occupied by SnO_2 nano particles.

3.3. CO ZIF-62 (CRYSTALLINE, GLASSY AND AMORPHOUS)

The following preparation and characterization details is included in the paper III, which is in submit.

3.3.1. PREPARATION OF CRYSTALLINE, GLASSY AND AMORPHOUS CO ZIF-62

Crystalline ZIF-62 (Co) was synthesized via a modified method based on previously literatures(54–57). In detail, imidazole (Im, 11.55 mmol, 785.4 mg) and benzimidazole (BIm, 1.66 mmol, 196 mg) were dissolved in 90 mL N,N-dimethylformamide (DMF). Then, $Co(NO_3)_2 \cdot 6H_2O$ (4 mmol, 1164 mg) was added into above solution. After stirring for 0.5 h, the solution was transferred into an oven and heated at 130 °C for 3 days. After cooling, the purple product was separated by centrifugation and dried under vacuum at 120 °C overnight. To obtain glassy ZIF, the

finely ground crystalline ZIF was heated to 450 °C at a heating rate of 10 °C min^{-1} and calcined for 5 minutes followed by cooling naturally to room temperature, which was purged with argon the whole process. The amorphous ZIF was prepared by ball milling the crystalline ZIF at 500 rpm for 10 h with a high energy planetary ball mill.

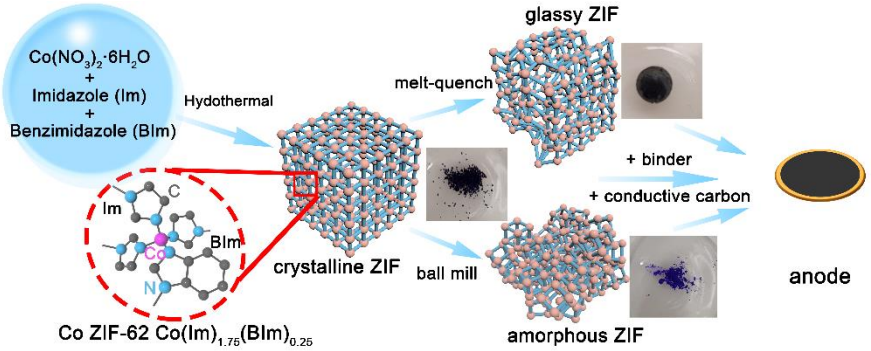

Scheme 3-3 Preliminary schematic representation of the crystalline, glassy and amorphous ZIF as anode for LIBs.

As shown in Scheme 3-1, glassy ZIF and amorphous ZIF could be prepared by melt-quench and mechanic ball milling, respectively. Then these three samples were mix with binder and conductive carbon to prepare electrode for coin-type cells, which were tested to study the electrochemical performance of these three samples.

3.3.2. CHARACTERIZATION OF CRYSTALLINE, GLASSY AND AMORPHOUS CO ZIF-62

The as-prepared crystalline, glassy and amorphous ZIF were characterized with XRD, DSC, TG, Raman, FTIR, XPS and BET to study their structures and components.

3.3.2.1 XRD patterns

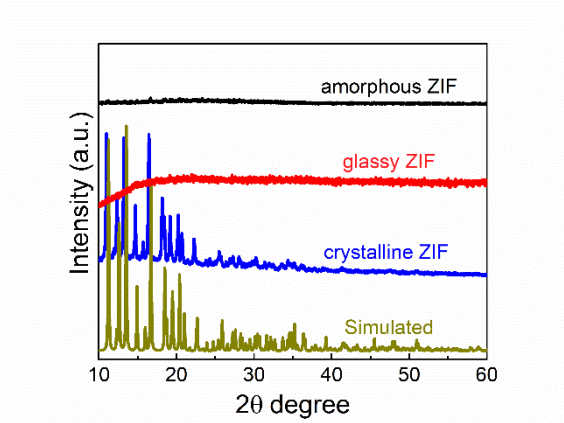

Figure 3-14 XRD patterns of crystalline, glassy, amorphous Co ZIF-62 and simulated one.

To study the structure differences of crystalline, glassy and amorphous ZIF, their XRD patterns were collected within the range of 10-60 degree. As presented in Figure 3-14, the crystalline ZIF shows sharp diffraction peaks at 11.2, 12.6, 13.5, 14.9, 16.0, 16.6, 18.5, 19.48, 20.4, 21.0, 22.7 degree, which match well with that of the simulated pattern, confirming the successful preparation of ZIF-62(56,58). The X-ray diffraction patterns of the glassy ZIF and amorphous ZIF demonstrates no obvious diffraction peaks, confirming the collapse of the crystalline structure into the long-range disordered state upon melt-quenching or ball milling treatment. The subtle structure differences between the glassy and amorphous ZIF are investigated by their differential scanning calorimetry (DSC) curves as shown below.

3.3.2.2 Differential scanning calorimetry and thermogravimetry curves

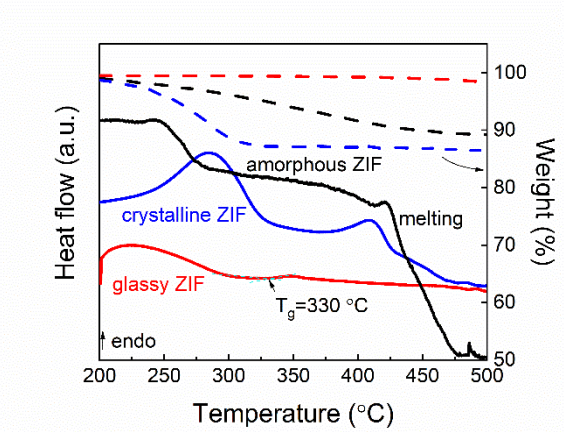

Figure 3-15 DSC upscans and thermalgravimetric curves of crystalline, glassy and amorphous Co ZIF-62 from 200 to 500 ℃ at a rate of 10 ℃ min^{-1}.

DSC curves and thermalgravimetric curves of crystalline, glassy and amorphous ZIF are shown in Figure 3-15. It is obvious that the as-prepared crystalline ZIF underwent solvent release corresponding to an endothermic peak at 270 ℃ and a melting event at around 435 ℃ upon heating at 10 ℃/min to 500 ℃ in the DSC upscan. The amorphous ZIF presents a similar scenario as that of crystalline ZIF, in which both solvent release and ZIF melting occur at about 250 and 435 ℃, respectively. In contrast, the glassy ZIF prepared by melt-quenching method presented a different DSC curve, which displays a glass transition temperature (T_g) at around 330 ℃. This indicates the glass nature of ZIF after melt-quenching process. As for the TG curves, notable weight losses were from 100 to 300 ℃ for both the crystalline and amorphous ZIF owing to the solvent release while that of glassy ZIF kept nearly constant. This implies that no other possible decompose reactions occurred in the three ZIF samples up to 500 ℃, suggesting their excellent thermal stability.

3.3.2.3 Raman spectra

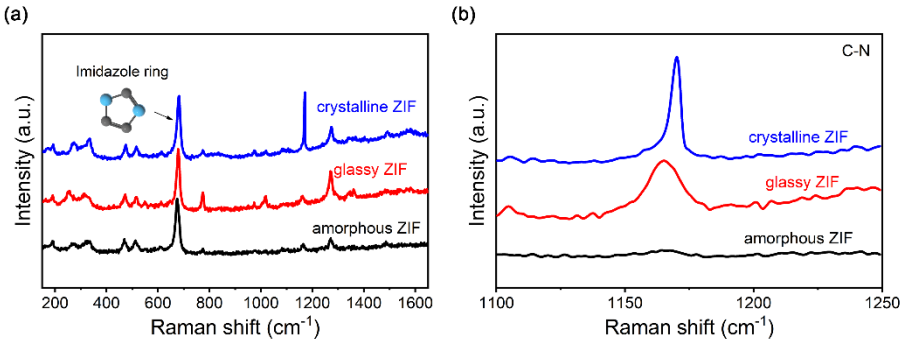

Figure 3-16 Raman spectra (a) and high-resolution spectra (b) of crystalline, glassy and amorphous Co ZIF-62.

The structures of the three ZIF samples were also investigated by Raman scattering method. It is noticed that crystalline, glassy and amorphous ZIF share similar Raman spectra, all of which correspond well with previous reports(54,58). This similarity endorses that the organic ligands in ZIF remain intact after melt-quench and high energy ball milling. However, some minor changes could be noticed from crystal to glassy ZIF and amorphous ZIF. The frequency of C-N stretching mode located at 1150-1200 cm^{-1} decreases after melt-quench or ball milling process, indicating small adjustment of C-N bonds during these processes(54,59,60).

3.3.2.4 Fourier-transform infrared spectra

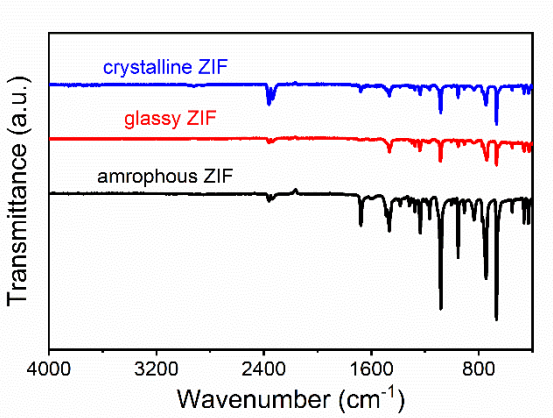

Figure 3-17 FTIR spectra of crystalline, glassy and amorphous Co ZIF-62 from 400 to 4000 cm^{-1}.

FTIR spectra of crystalline, glassy and amorphous ZIF were also collected. As shown in Figure 3-17, the peak at 1676 cm^{-1} of crystalline ZIF and amorphous ZIF is originated from carbonyl groups from solvent molecules (DMF) trapped in pores of ZIF. This peak become less obvious in spectrum of glassy ZIF, which is explained by the release of DMF molecules during heating treatment. The peaks at 1465, 1235, 1082, 668 cm^{-1} could be noticed in all three spectra, which correspond to C-N stretching, C-H in-plane-bending, C-H out-of-plane-bending and ring deformation out-of-plane-bending, respectively(61), which originate from the organic ligands of ZIF. In summary, crystalline, glass and amorphous ZIF showed almost the same patterns, which indicates the integrity of organic ligands preserved during the melt-quenching or ball milling process.

3.3.2.5 X-ray photoelectron spectra

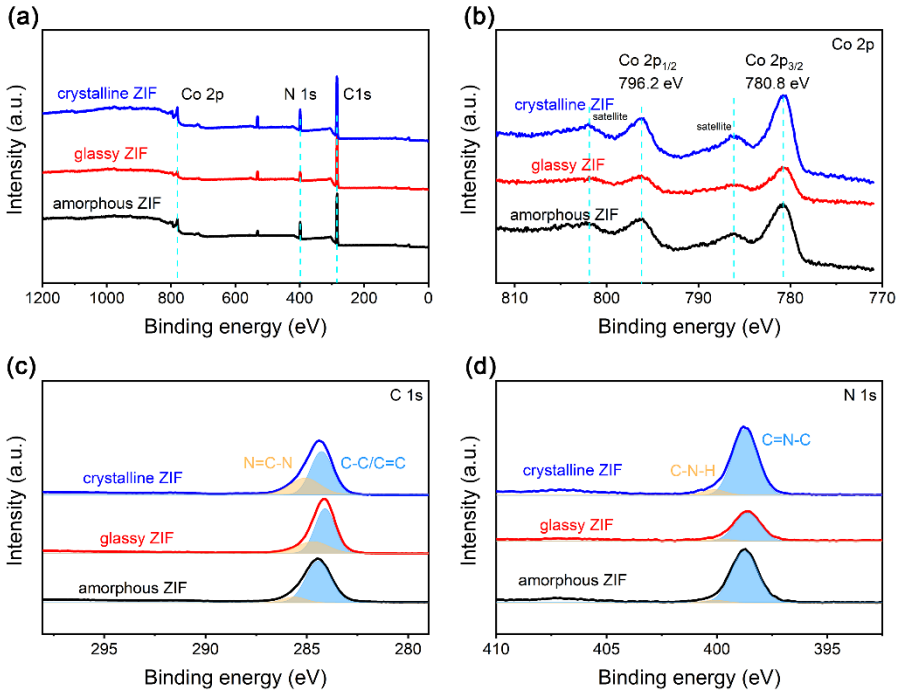

Figure 3-18 XPS survey spectra (a), core level spectra of Co 2p (b), C 1s (c), and N 1s (d) of crystalline ZIF, glassy ZIF and amorphous Co ZIF-62, respectively.

X-ray photoelectron spectroscopy (XPS) spectra were collected to analyze the surface elemental chemistry of crystalline, glassy and amorphous ZIF. The survey spectra display the regions of Co, C and N, confirming the components of ZIF remain unchanged after heat treatment or ball milling processes. The core level spectrum of Co 2p exhibits the Co $2p_{1/2}$ and Co $2p_{3/2}$ peaks locate at 796.2 and 780.8 eV with two

satellite peaks at 801.9 and 786.2 eV, respectively. The three samples share the same patterns of Co 2p, confirming that the valance state of Co remains unaffected after the heat treatment and ball milling processes. In addition, the peak of C 1s can be deconvoluted into two peaks referred to C-C/C=C at 284.2 eV and N=C-N at 286 eV, respectively. Similarly, the N 1s peak consists of the C=N- peak at 398.7 eV and the C-N-H peak at 399.5 eV, respectively(62). These samples present almost identical C 1s and N 1s spectra, suggesting that the imidazole and benzimidazole ligands in ZIF retain their structure through the melt-quench and the ball milling treatment.

3.4. SUMMARY

In this Chapter, the preparations and characterizations of Al-MOF/graphene, SnO_2@MOF/graphene, glassy and amorphous ZIF were presented, detailed information could be found in paper I, II and III. The results show the successful preparation of these composites via different methods, including self-assembly, wet impregnation, melt-quench, and mechanic ball milling. Their electrochemical performance was evaluated and presented in Chapter 4, Chapter 5, and Chapter 6, respectively. In addition, these different composites confirm the great potential of MOFs as platform, precursor template and matrix for preparing novel materials for energy storage.

CHAPTER 4. ELECTROCEHMICAL PERFORMANCE OF AL-MOF/GRAPHENE

This Chapter is mainly based on paper I, in which all the detailed information about preparation, characterization and electrochemical performance of the Al-MOF/graphene composite could be found. In following parts, the electrochemical performance of Al-MOF and Al-MOF/graphene were evaluated in a coin cell. To investigate the structure evolution during charge-discharge processes, characterizations after cycling were also conducted.

4.1. CYCLIC VOLTAMMETRY CURVES

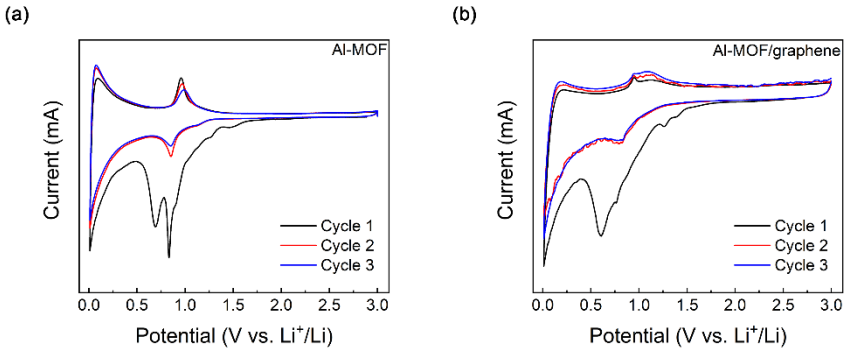

Figure 4-1 Cyclic voltammetry curves of the initial 3 cycles of pristine Al-MOF (a) and the Al-MOF/graphene composite (b) within the range from 0.01 to 3 V at a rate of 0.1 mV s^{-1}.

As shown in Figure 4-1, Al-MOF presents two main reduction peaks at 0.68 V and 0.82 V during the first cathodic scan, which originate from the formation of solid electrolyte interface (SEI) film and some other irreversible reactions, respectively(63). In the next two cathodic scans, one main peak at 0.84 V corresponds to the reversible lithiation process of the Al-MOF(64). In addition, three anodic upscans present the same shapes with two oxidation peaks at about 0.1 V and 0.9 V, which might be related to two different lithium extraction processes from the Al-MOF, respectively. As for the Al-MOF/graphene composite, its CV curves resemble to those of the pristine Al-MOF, implying they might share a similar lithium insertion/extraction mechanism.

4.2. GALVANOSTATIC CHARGE-DISCHARGE TESTS

4.2.1. CHARGE-DISCHARGE VOLTAGE PROFILES

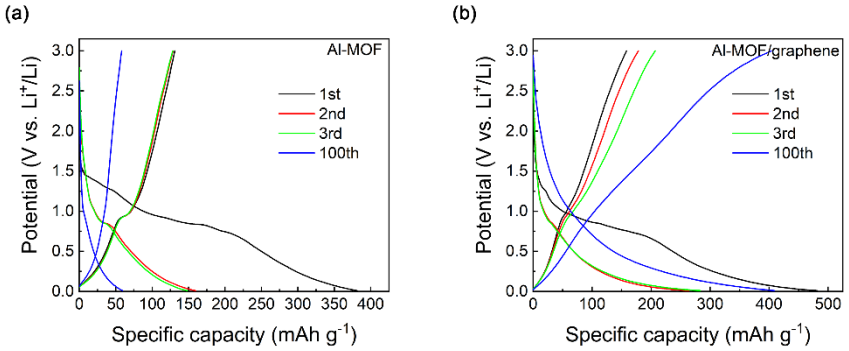

Figure 4-2 Galvanostatic charge-discharge voltage profiles of the initial 3 and the 100th cycles of the pristine Al-MOF (a) and the Al-MOF/graphene composite (b) at a current density of 0.1 A g^{-1} during the voltage range of 0.01-3 V.

The initial three and 100th galvanostatic charge-discharge voltage profiles of the Al-MOF and Al-MOF/graphene were displayed in Figure 4-2. The first discharge profile of Al-MOF presents two discharge plateaus at about 0.7 and 0.1 V, which might originate from the formation of SEI layer and other irreversible reactions. In the following two cycles, a discharge plateau at 0.8 V and a charge plateau at 0.9 V that are related to the Li^+ intercalation and deintercalation could be observed, coinciding well with the couple of redox peaks in the CV curves of Al-MOF. As expected, both the charge and discharge plateau become almost absent after 100 cycles, which might result from the shattered structure of Al-MOF. The initial discharge-charge capacities of Al-MOF are 381/131 mAh g^{-1} and capacities of the second, third and 100th cycles drop to 159/128, 148/128 and 59/58 mAh g^{-1}, respectively, indicating the poor cycling stability of the pristine Al-MOF.

In contrary, the Al-MOF/graphene composite presents a quite different scenario compared with pristine Al-MOF. Specifically, the voltage profiles of Al-MOF/graphene composite display similar charge and discharge plateaus as that of the pristine Al-MOF. Interestingly, the initial three discharge/charge capacities of the Al-MOF/graphene anode are 481/158, 263/178 and 283/207 mAh g^{-1}, respectively, which are much larger than those of the pristine Al-MOF. Notably, the Al-MOF/graphene composite delivers an increasing capacity along with cycling and the capacity reached 409/403 mAh g^{-1} after 100 cycles, which is much larger than that of the initial three cycles. Generally, the capacity of electrode decays along with cycling. However, this Al-MOF/graphene composite exhibits an unusual increasing capacity, which might originate from electrochemically activations during the repeated charge-discharge processes.

4.2.2. CYCLING PERFORMANCE

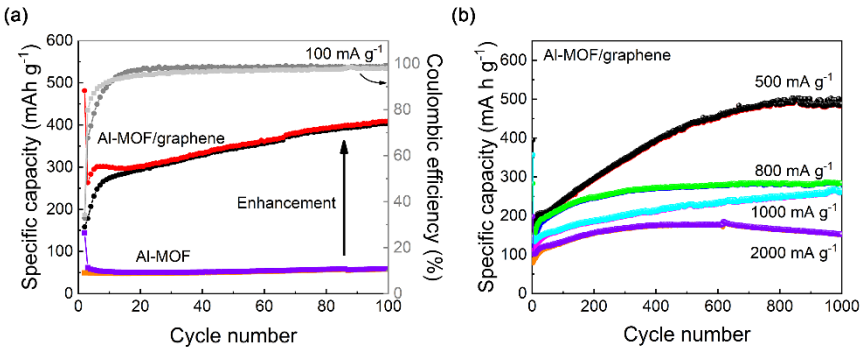

Figure 4-3 (a) Cycling performance and Coulombic efficiency of Al-MOF and the Al-MOF/graphene composite at a current density of 0.1 A g^{-1}. (b) Cycling performance of Al-MOF/graphene at current densities of 0.5, 0.8, 1 and 2 A g^{-1}.

The cycling stability of Al-MOF and Al-MOF/graphene composite were evaluated at the current density of 0.1 A g^{-1}. As displayed in Figure 4-3, Al-MOF deliveries a capacity of 381 mAh g^{-1} with an initial Coulombic efficiency of 34% during the first cycle. This large capacity drop might be related to the formation of SEI layer and other irreversible reactions during the first lithium insertion process. Then the pristine Al-MOF presents a stable capacity of 60 mAh g^{-1} and a Coulombic efficiency about 97% up to 100 cycles after a slight capacity decline. On the contrary, the Al-MOF/graphene composite presents a significantly improved performance. As for the cycling stability, irreversible capacity losses in the first 20 cycles might be mainly related to the SEI layer growth and other irreversible side reactions. This capacity loss should be mitigated in future works. To achieve this goal, some strategies are promising, including pre-lithiation and replacement of solid electrolytes for liquid ones. After capacity losses upon initial several cycles, the Al-MOF/graphene composite displays a huge capacity jump from 263 to 403 mAh g^{-1} after 100 cycles, which is more than 6 times higher than that of the pristine Al-MOF. This remarkable capacity enhancement of the Al-MOF/graphene composite in this work is reported for the first-time, especially for MOFs-based anode materials. This enhancement might be attributed to the following features of the Al-MOF/graphene composite: First, the porous MOF particles covered with graphene sheets provides high specific surface area and abundant Li^+ ions transport paths, which might accelerate the activation process of MOF particles is after being covered with graphene sheets. This "activation" facilitates Li^+ ions diffuse into the internal pores of the MOF and provides more reaction sites for lithium storage, contributing to the enhanced capacity. Second, in addition to facilitating the electron transport, the excellent mechanic property of the graphene sheets can strengthen the MOF particles and keep their structure intact during charge-discharge processes. However, the accurate mechanism for such an

improvement in electrochemical performance of Al-MOF/graphene still need to be further explored.

The long-term cycling stability of the Al-MOF/graphene composite are presented in Figure 4-3b. The Al-MOF/graphene composite maintains impressive capacities of 484, 284, 267, and 153 mAh g^{-1} after 1000 cycles at 0.5, 0.8, 1 and 2 A g^{-1}, respectively. Notably, the Al-MOF/graphene composite exhibits a capacity increase trend with continuous cycling up to 1000 cycles at current densities lower than 1 A g^{-1}. To date, this phenomenon has not been reported for MOFs-based anode materials. This striking phenomenon might originate from the gradual activation process of this composite, during which more and more internal pores and channels become accessible for electrolyte and Li^+ ions. Then a large capacity could be obtained after cycling. However, when the high current density increased to 2 A g^{-1}, the capacity peaked at around 500 cycles with a maximum value of 178 mAh g^{-1}, after which the capacity decayed slowly to 152 mAh g^{-1}. This capacity fading might be ascribed to the structural degradation at high current density.

4.2.3. RATE PERFORMANCE

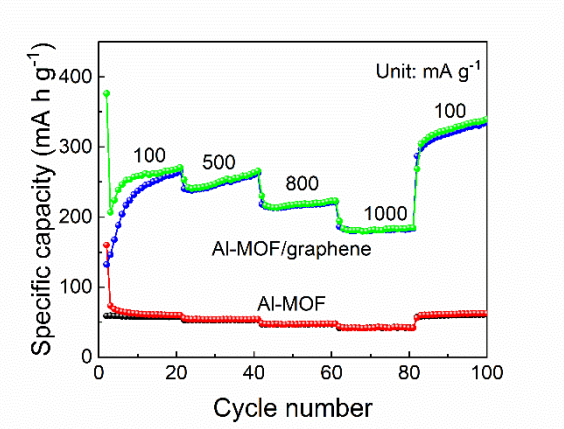

Figure 4-4 Rate performance of the pristine Al-MOF and the Al-MOF/graphene composite.

The rate performances of the pristine Al-MOF and the Al-MOF/graphene composite are evaluated under different current densities. As expected, the Al-MOF/graphene composite exhibits a better rate capability than the pristine Al-MOF. In detail, the Al-MOF/graphene composite exhibits average capacities of 260, 250, 220 and 180 mAh g^{-1} at current densities of 0.1, 0.5, 0.8 and 1 A g^{-1}, respectively. Then the capacity recovers to 326 mAh g^{-1} when the current decreases to 0.1 A g^{-1}, suggesting the outstanding rate capability of the composite. More strikingly, the Al-MOF/graphene composite exhibits similar incline trends under different current densities, which not only suggests its excellent rate capability and cyclic stability, but also proves that the rate tests affect the structure of MOF as that of galvanostatic charge-discharge

experiment, i.e., the activation of structure of this composite induced by charge-discharge processes. In the meantime, the pristine Al-MOF merely exhibits 55, 53, 47 and 42 mAh g^{-1} under the same conditions, indicating its poor rate performance.

4.3. CHARACTERIZATIONS AFTER CHARGE-DISCHARGE CYCLING

To explore the reasons that might contribute to the performance enhancement of the Al-MOF/graphene composite, its XRD pattern, TEM image, XPS spectra after 100 charge-discharge cycles at a current density of 0.1 A g^{-1} were also collected.

4.3.1. STRUCTURAL CHARACTERIZATIONS

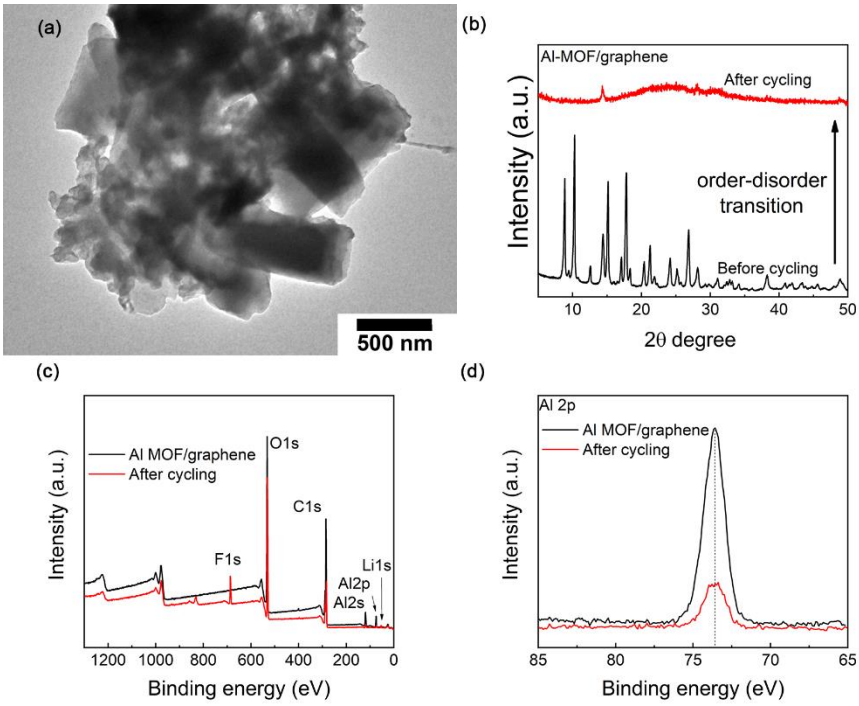

Figure 4-5 (a) Ex-situ TEM image of Al-MOF/graphene after 100 discharging/charging cycles. Ex-situ XRD patterns (b), ex-situ XPS survey spectrum (c) and high-resolution spectra of Al 2p (d) of as-prepared Al-MOF/graphene and Al-MOF/graphene after 100 discharging/charging cycles.

To clarify the origin of the excellent electrochemical performance of the Al-MOF/graphene after cycling, ex-situ XRD patterns were collected. As clearly shown in Figure 4-5a, no obvious pronounced diffraction peaks could be observed after cycling, suggesting this composite is amorphized and the long-range order structures

are destroyed after charge-discharge cycles, i.e., the order-disorder transition occurs, and finally the long-range order vanishes. The possible scenario of the order-disorder transition might be portrayed as follows. It is known that the Al-MOF contains many voids, and ligand walls between the neighboring voids. It is also recognized that the coordinative bonds between the central atom (e.g., Al^{3+} nodes in this work) and organic ligand are much weaker than the covalent bonds in the ligand molecules (BDC molecules). Considering these two factors, the repeating lithium ions insertion/extraction might have a large impact on coordinative bonds than covalent bonds, and thereby lead to the rotation, liberation, and migration of some ligands, and the breakage of the Al–O–Al skeleton, which results in the disappearance of diffraction peaks of Al-MOF(48). It means that both rotational and translational disordering are induced during lithiation/delithiation processes, and consequently more and larger channels and voids are generated. Thus, the number of channels continuously increases along with cycling and then the degree of long-range order in Al-MOF is gradually diminished while this might lead to a gradually enhanced lithium diffusion and storage in the meantime.

The ex-situ TEM image of the Al-MOF/graphene composite after cycling reveal clearly that the morphology of this composite remains unaltered, indicating that the graphene sheets might protects the Al-MOF particles from being destroyed, i.e., the overall structural integrity of this composite is well conserved. This high structural stability of Al-MOF/graphene against lithium intercalation/deintercalation might be related to the protecting role of graphene sheets. In addition, the survey XPS spectrum Li, F, Al, C and O elements could be observed in the Al-MOF/graphene composite subjected to 100 charge-discharge cycles, as seen in Figure 4-5c. The Li and F mainly originate from the SEI film since a minor amount of the electrolyte would react with lithium during the first lithiation process. Compared to the as-prepared Al-MOF/graphene, no obvious change in valence states of Al upon 100 cycles could be noticed, implying that the charge-discharge processes do not alter the valance state of Al nodes in MOF. These results suggest that although the long-term order structure of MOF is lost, the chemical states and components remain unchanged.

4.3.2. ELECTROCHEMICAL IMPEDANCE SPECTRA

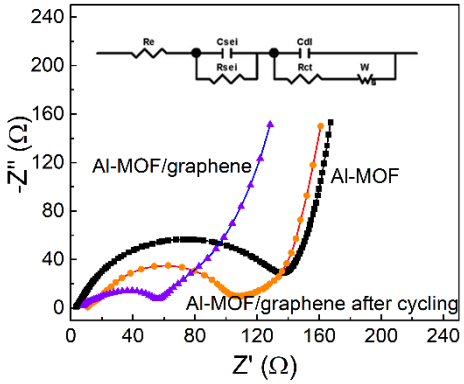

Figure 4-6 Nyquist plots of the pristine Al-MOF, the Al-MOF/graphene composite and Al-MOF/graphene after cycling (Inset is the equivalent circuit).

Figure 4-6 displays electrochemical impendence spectra (EIS) of pristine Al-MOF, the Al-MOF/graphene composite and Al-MOF/graphene cycling. It is obvious that all EIS spectra consist of one depressed semicircle from the high to middle frequency region and one inclined line at low frequency end. Fitting by the equivalent circuit, is ascribed to the resistance (R_e) of the bulk electrode, electrolyte and the separator is determined as the intercept at far-left end while the semicircle mainly originates from the SEI resistance (R_{SEI} and C_{SEI}) and charge transfer resistance (R_{ct} and C_{dl}). The line with a slope of 45° at the low frequency is related to the Warburg impedance (W), which is associated with the diffusion of Li^+ ions at the interface between the active material particles and electrolyte(65). Obviously, the diameter of the semicircle of the Al-MOF/graphene composite is much smaller than that of the pristine Al-MOF and that of the composite after 100 cycles, which is still smaller than that of the pristine Al-MOF. This indicates that the Al-MOF/graphene composite exhibits enhanced Li^+ ions migration kinetics and faster charge transfer reactions compared to Al-MOF after the addition of graphene sheets. However, the enhanced kinetics of Al-MOF/graphene is gradually undermined during the repeated charge-discharge cycles, which might result from growth of the SEI film, side reactions or structural degradation of the MOF.

4.3.3. CYCLIC VOLTAMMETRY CURVE

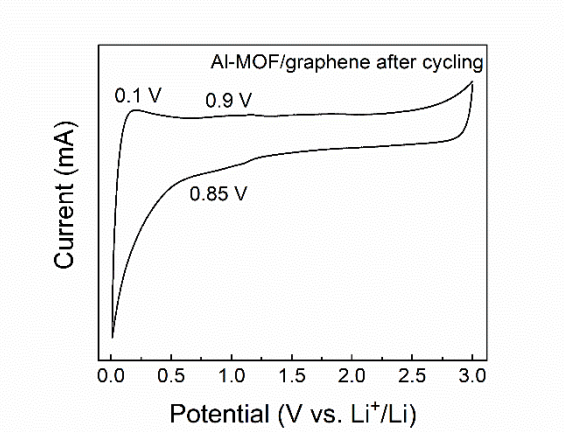

Figure 4-7 Cyclic voltammetry curve of the Al-MOF/graphene composite after cycling for 100 cycles.

The CV curve of the Al-MOF/graphene composite after cycling was displayed in Figure 4-7. It exhibits a weak peak at about 0.85 V in the cathodic scan and two peaks at 0.1 and 0.9 V in the anodic scan. These peaks match well with that of pristine Al-MOF/graphene, confirming that the lithium insertion/extraction mechanism remain unchanged during all 100 cycles while the structure of MOF lost long-term order.

4.4. PROPOSED MECHANISM

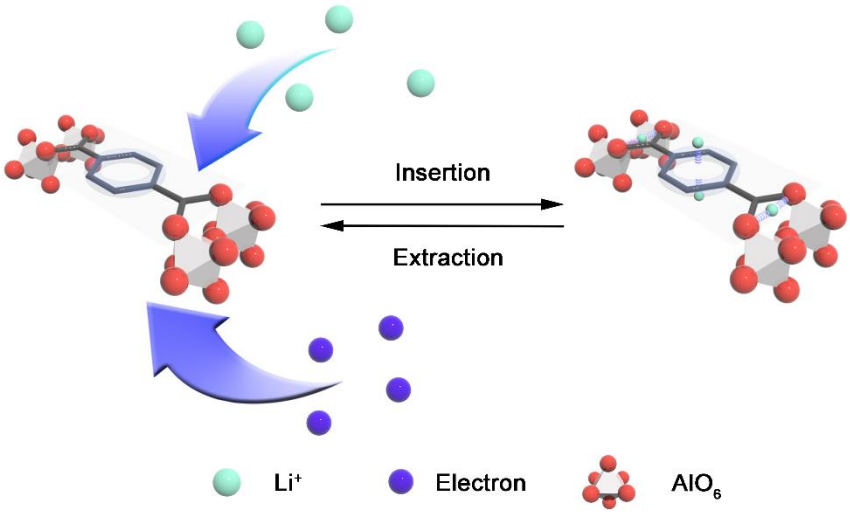

Scheme 4-1 Proposed mechanism for Li^+ ions insertion-extraction process into or from Al-MOF.

Based on previous reports and above results, the lithium intercalation/deintercalation mechanism of the Al-MOF is proposed as follows(64,66):

$$Al(OH)[O_2C–C_6H_4–CO_2] + xLi^+ + xe^- \leftrightarrow Al(OH)[O_2C–C_6H_4–CO_2Li_x]$$

which is sketched as in Scheme 4-12, the Al-MOF might possess an insertion type lithium storage mechanism. In detail, after diffusing into MOF, Li^+ ions might interact with aromatic rings and carboxyl groups of organic ligands instead of metal nodes (Al in this MOF)(48). The lithium insertion/extraction processes of MOF then contribute to the redox peaks observed in CV curves (Figure 4-1). However, further experiments and investigation should be done to clarify the actual lithium storage mechanism of the Al-MOF.

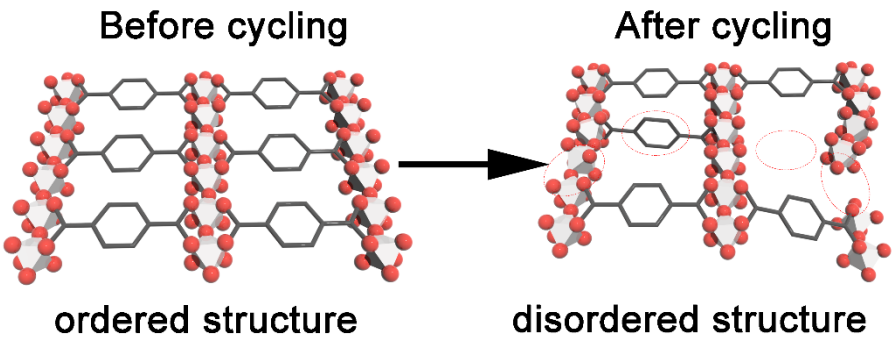

Scheme 4-2 Graphic representation of the order-disorder transition of the Al-MOF during charge-discharge cycles.

The order-disorder scenario of Al-MOF is simplified as Scheme 4-2. The repeated lithium insertion/extraction alter the order arrangement of organic ligands, causing ligand missing, rotations, the distortion or breakage of metal-node skeleton, etc. These induced defects destroy the long-term order of MOF structure while the integrity of MOF could be protected by the graphene sheets. And this order-disorder transition could introduce more voids and channels for lithium diffusion and storage, which contribute to the greatly enhanced electrochemical performance of Al-MOF/graphene along with charge-discharge cycles.

4.5. SUMMARY

In this Chapter, the electrochemical performance of the Al-MOF/graphene composite was evaluated via GCD, CV and EIS methods, and its lithium storage mechanism was further investigated via ex-situ characterization techniques. As confirmed by cycling

stability tests, the Al-MOF/graphene composite exhibited a drastically enhanced capacity from 60 to 400 mAh g^{-1} at the current density of 0.1 A g^{-1} during repeated charge-discharge cycles. To illustrate this remarkable capacity improvement, we proposed that an order-disorder transition of MOF caused by lithiation/delithiation should be the main reason. This structure disordering of MOF could induce more channels and voids for lithium migration and storage while MOF particles remain electronically contact with current collectors with the help of graphene sheet coverage. These graphene sheets also increase the electronic conductivity, and simultaneously enhance both the Li^+ ions migration kinetics through the SEI layer and the charge transfer reactions. In summary, this order-disorder transition in the Al-MOF during lithiation/delithiation cycles provides us a new perspective to enhance the cycling stability of MOF-based anode materials for LIBs, which might also be inspiring for other anode materials.

CHAPTER 5. ELECTROCHEMICAL PERFORMANCE OF TIN DIOXIDE@MOF/GRAPHENE

In this Chapter, the lithium storage performance of SnO_2@MOF and the SnO_2@MOF/graphene composite were evaluated in coin-type cells while the detailed information could be found in paper II. To verify the protection role of MOF on SnO_2 nano particles, structural and electrochemical characterizations after cycling were also conducted. For comparison, as-prepared SnO_2 and SnO_2+MOF physical mixture were also tested.

5.1. CYLIC VOLTAMMETRY CURVES

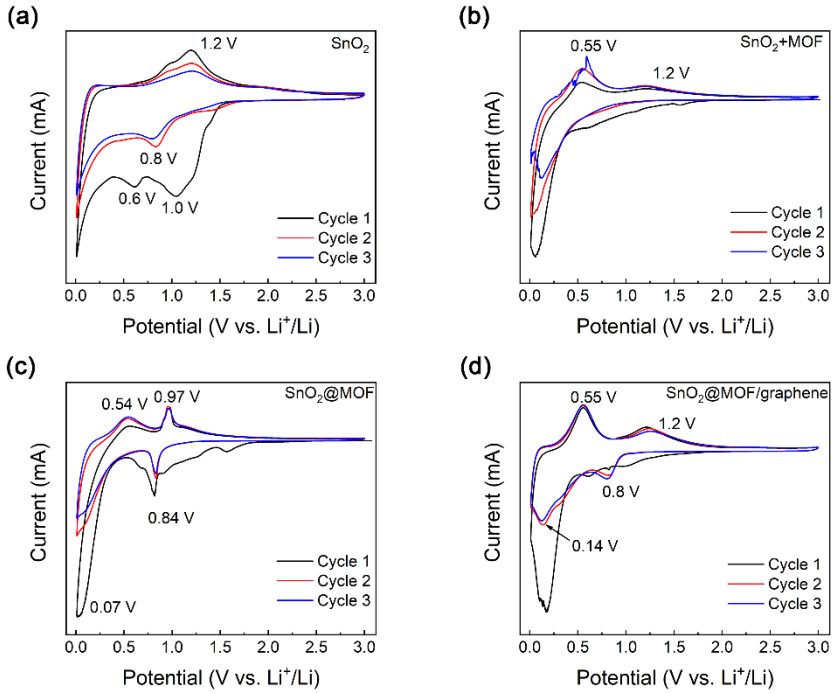

Figure 5-1 Cyclic voltammetry curves of initial three cycles for as-prepared SnO_2 (a), SnO_2+MOF physical mixture (b), SnO_2@MOF (c) and SnO_2@MOF/graphene (d) in the range from 0.01 to 3 V at a scanning rate of 0.1 mV s^{-1}.

To investigate the lithium storage mechanism, as-prepared SnO_2, SnO_2+MOF physical mixture, SnO_2@MOF and SnO_2@MOF/graphene were evaluated by cyclic voltammetry. As for the SnO_2@MOF, two noticeable peaks at 0.84 and 0.07 V could be observed in the first cathodic scan, which might originate from the insertion of Li^+ ions into MOF and the growth of solid electrolyte interface (SEI) layer, respectively. Besides, the broad peak at 1.0 - 0.6 V could be related to the reduction of SnO_2 to Sn. In the subsequent anodic scan, the peaks at 0.54 and 0.97 V are obvious, corresponding to the dealloying process of Li_xSn and Li^+ ions extraction from MOF, respectively(47,48). These two processes could be also observed in CV curves of the as-prepared SnO_2 and SnO_2+MOF physical mixture (Figure 5-1a and b). Interestingly, the redox peaks related to lithium extraction from MOF (at 0.97 and 0.84 V) are relative stronger than those originating from SnO_2 (at 1.2 and 0.8 V), which might indicate that MOF in the SnO_2@MOF composite contributes a larger portion to the current than SnO_2 does. However, the redox peaks originated from SnO_2 are much stronger than those of MOF in the CV curves of SnO_2+MOF physical mixture. This different could be interpreted as the successful packing of SnO_2 into MOF matrix. In the physical mixture, most SnO_2 could still contribute to the redox current. However, if SnO_2 nano particles are embedded in MOF matrix, some of them would be electrochemically "dead", i.e., they cannot interact with Li^+ ions completely due to poor electronic conductivity of SnO_2 and MOF shell, then smaller redox current could be generated. Thus, the redox peaks related to SnO_2 become weak in CV curves of the SnO_2@MOF composite.

The SnO_2@MOF/graphene composite presents a different CV curves from SnO_2@MOF, in which two couples of redox peaks at 0.14/0.55 V and 0.8/1.2 V could be observed. These two couples of redox peaks mainly originate from the alloying/dealloying processes of Li_xSn and the partial reversible transformation of SnO_2, respectively(67). Interestingly, the redox peaks at 0.97/0.84 V, which are related to MOF, are overlapped by the couple of strong peaks assigned to the reversible transformation of SnO_2 at 0.8/1.2 V. This could be illustrated as follows. After hybridized with graphene sheets, because of the enhanced electronic conductivity, the peaks originating from SnO_2 (at 0.14/0.55 V) become intense compared with SnO_2@MOF. This phenomenon could be explained by that a larger fraction of the embedded SnO_2 nanoparticles in SnO_2@MOF/graphene anode could interact with Li^+ ions and thereby contribute to a larger redox current. After the first cycle, the CV curves of the SnO_2@MOF/graphene composite present the same shape in the subsequent two cycles, indicating the highly reversible electrochemical reactions (between SnO_2 and Sn) and excellent structural stability of this composite.

5.2. GALVANNSTATIC CHARGE-DISCHARGE TESTS

5.2.1. CHARGE-DISCHARGE VOLTAGE PROFILES

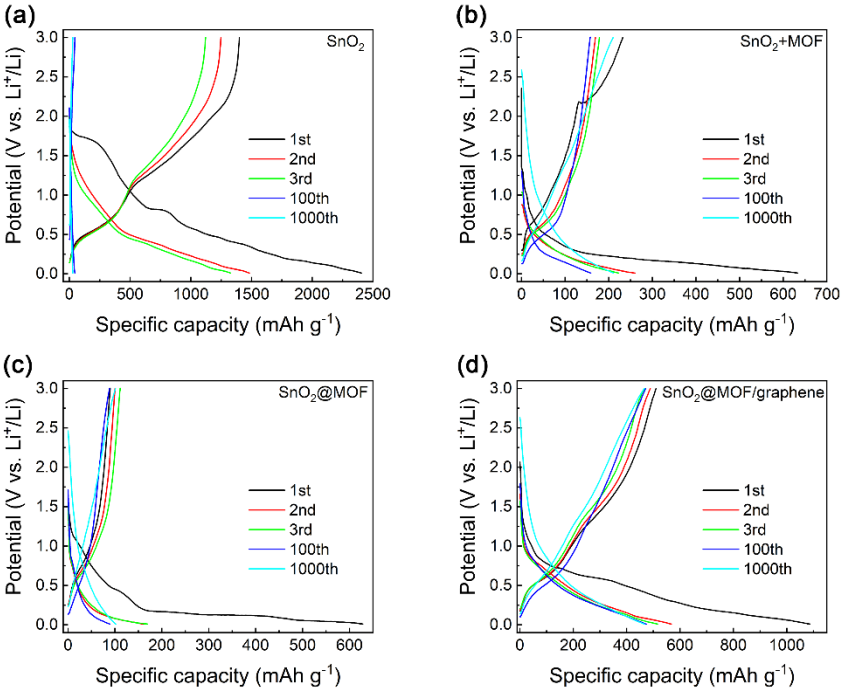

Figure 5-2 Charge/discharge profiles of the initial three, 100th and 1000th cycles of as-prepared SnO_2 (a), SnO_2+MOF physical mixture (b), SnO_2@MOF (c) and SnO_2@MOF/graphene (d) within the range from 0.01 to 3 V at a current density of 1 A g^{-1}.

The galvanostatic charge/discharge profiles of the as-prepared samples are displayed in Figure 5-2. The as-prepared SnO_2 shows several plateaus in the first discharge profile, which might result from the formation of SEI film and other irreversible reactions. Then its capacity keeps dropping and no detectable capacity could be obtained after 100 cycles. In addition, the SnO_2+MOF physical mixture exhibits voltage curves with similar shape while it presents a capacity of 200 mAh g^{-1} after 1000 cycles. As for the SnO_2@MOF, discharge plateaus at around 1.0 and 0.6 V match well with its CV curves. In the following charge profiles, charge plateaus at about 0.6 and 1.2 V mainly originate from the dealloying processes of Li_xSn and the lithium extraction from MOF, respectively. In contrast, the SnO_2@MOF/graphene composite displays plateaus locate at 0.8 and 1.2 V in the galvanostatic charge/discharge curves, which correspond to the reversible reactions between SnO_2 and Li_xSn, respectively(68). Notably, the plateaus remain stable at 0.8/1.2 V even after

1000 cycles and the capacity is about 460 mAh g^{-1}, indicating the high reversibility of electrochemical processes and cycling stability of the SnO_2@MOF/graphene.

5.2.2. CYCLING PERFORMANCE

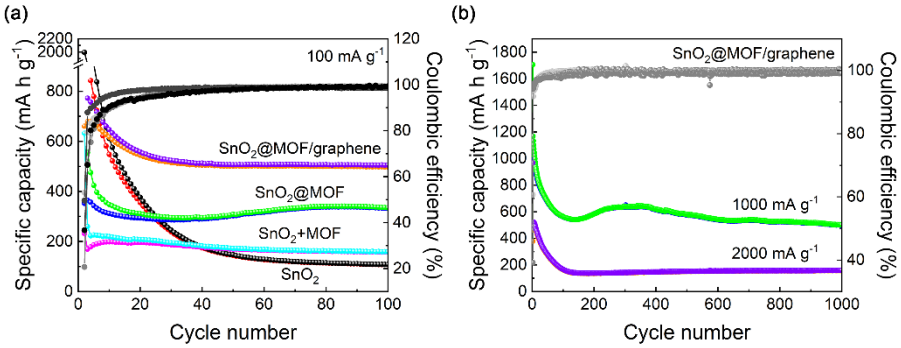

Figure 5-3 (a) Cycling performance and Coulombic efficiency of as-prepared SnO_2, SnO_2+MOF, SnO_2@MOF and the SnO_2@MOF/graphene composite at a current density of 0.1 A g^{-1}. (b) Cycling performance of the SnO_2@MOF/graphene composite at current densities of 1 and 2 A g^{-1}.

The cycling performances and the Coulombic efficiency of SnO_2, SnO_2+MOF, SnO_2@MOF and SnO_2@MOF/graphene were investigated by galvanostatic charge/discharge tests within the voltage range from 0.01 to 3 V at a current density of 0.1 A g^{-1}. As displayed in Figure 5-3a, the first charge-discharge capacities are 1996/1060, 633/232, 1700/352, 1332/660 mAh g^{-1} for SnO_2, SnO_2+MOF, SnO_2@MOF and SnO_2@MOF/graphene, leading to CE about 53%, 37%, 20% and 50%, respectively. This drastic capacity decays for these samples might originate from both SEI growth and incomplete delithiation processes. Interestingly, the SnO_2@MOF/graphene composite demonstrates a higher CE than SnO_2+MOF, SnO_2@MOF, which might be explained as follows. When wrapping SnO_2@MOF with graphene sheets, the "accessible" surface area of MOF decreases since the graphene sheets could blocks part of the pores of MOF. Consequently, less "dead" lithium will be trapped in the pores of MOF after being covered by graphene sheets, leading to a higher CE during the first cycle. In addition, the SEI growth would also be limited since the decreased surface. However, the CE of these composites are still relatively low for practical LIBs. This problem could be overcome by other methods, e.g., pre-lithiation process, before practical applications.

It is obvious to notice that the capacity of SnO_2 decreases to about 100 mA h g^{-1} within the first 50 cycles while SnO_2@MOF and SnO_2@MOF/graphene exhibit almost stable capacity after mild capacity drops. This poor cycling stability of SnO_2 mainly originates from its structural degradation caused by the drastic volume change and the aggregation of in-situ formed Sn particles(69,70). The SnO_2+MOF physical mixture

presents a capacity of 160 mAh g^{-1}, which mainly originate from the MOF instead of SnO_2. The SnO_2@MOF preserves a capacity of 330 mA h g^{-1} after 100 cycles, which is better than that of SnO_2+MOF, confirming the importance of MOF protection on the cycling stability. As for SnO_2@MOF/graphene composite, the largest capacity of 500 mAh g^{-1} is obtained after 100 cycles. This best performance could be explained by several reasons. First, the volume changes of SnO_2 during cycling could be accommodated by the MOF matrix and graphene sheets, avoiding capacity decay caused by material pulverization. Then, because the in-situ formed Sn nanoparticles from SnO_2 nano particles are enclosed in the pores of the MOF, the aggregation of Sn nanoparticles are hindered, preventing formation of Sn clusters with less electrochemical activity(71). Third, the electronic conductivity is considerably improved with the addition of graphene sheets. Besides, the cycling performance of SnO_2@MOF/graphene was also evaluated at high current densities of 1 and 2 A g^{-1}. Capacities of 450 and 160 mAh g^{-1} could still be kept up to 1000 cycles, suggesting the excellent cycling stability of the SnO_2@MOF/graphene composite even at high current densities. The astounding cycling stability of this composite against Li^+ ions insertion/ extraction can also be proved by its excellent rate performance.

5.2.3. RATE PERFORMANCE

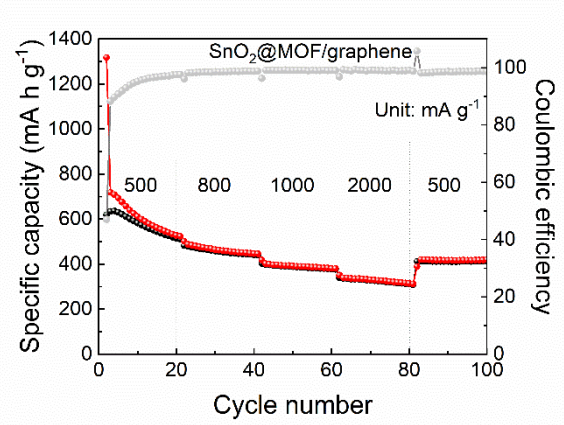

Figure 5-4 Rate performance of the SnO_2@MOF/graphene composite.

To evaluate the rate capability, the SnO_2@MOF/graphene composite was charge-discharged at different current densities. Then, average capacities of 565, 450, 385, and 324 could be obtained at 500, 800, 1000, 2000 mA g^{-1}, respectively. It is worth noting that the capacity retains to 410 mA h g^{-1} when the current density was restored to 500 mA g^{-1}. Except a sharp capacity drop when the current density is 2 A g^{-1}, the SnO_2@MOF/graphene composite exhibits an excellent rate capability.

5.2.4. ELECTROCHEMICAL IMPEDANCE SPECTRA

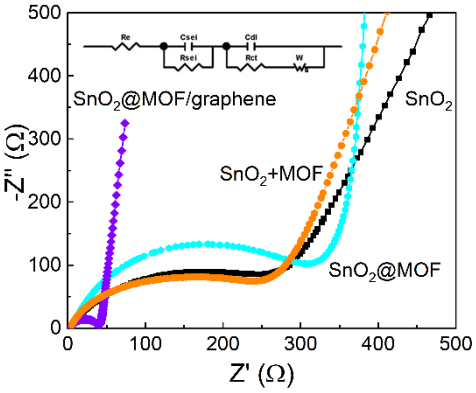

Figure 5-5 Nyquist plots of the as-prepared SnO_2, SnO_2+MOF mixture, SnO_2@MOF and SnO_2@MOF/graphene (Inset is the equivalent circuit).

EIS was conducted to investigate the electrochemical performance of SnO_2, SnO_2+MOF, SnO_2@MOF and SnO_2@MOF/graphene. As shown in Figure 5-5, all Nyquist plots display similar shapes, consisting of a depressed semicircle at high frequency region and an inclined line at low frequency end(72). According to previous reports, the charge transfer resistance (R_{ct}) is reflected by the diameter of the semicircle, while the Warburg impedance (W) that related to the Li^+ ions diffusion effects is represented by the straight line(73). The inset figure is the equivalent circuit used to fit these impedance data. The EIS plot of SnO_2@MOF/graphene presents the smallest diameter of the semicircle than those of SnO_2, SnO_2+MOF and SnO_2@MOF, indicating its smaller R_{ct} after the hybridization of graphene sheets, i.e., SnO_2@MOF/graphene anode exhibits the highest electronic conductivity.

5.3. CHARACTERIZATION AFTER CHARGE-DISCCHARGE CYCLING

To verify the protection role of MOF and investigate the structure changes during charge-discharge cycles, TEM images, XPS spectra, EIS spectrum and CV curves of SnO_2@MOF/graphene after 1000 cycles at 1 A g^{-1} were also collected.

5.3.1. STRUCTURAL CHARACTERIZATIONS

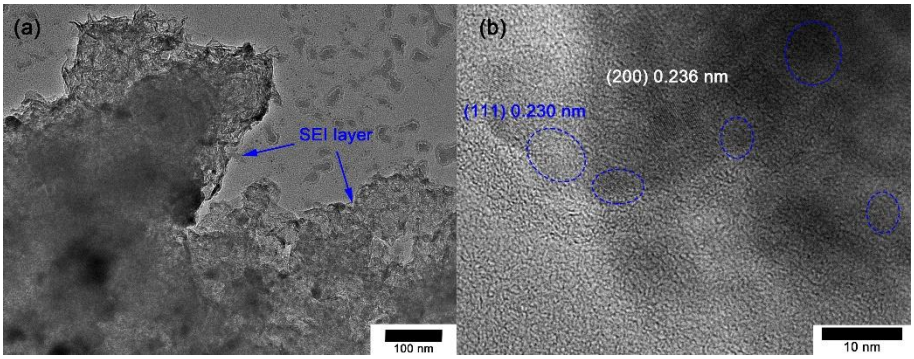

Figure 5-6 TEM image (a) and HRTEM image of the SnO_2@MOF/graphene composite after 1000 charge-discharge cycles.

The morphology of the SnO_2@MOF/graphene composite after cycling was observed by ex-situ TEM and HRTE. It is noticed that a uniform SEI film with a thickness about 10 nm formed and the MOF kept its morphology after cycling. The HRTEM image of SnO_2@MOF/graphene composite after cycling displays SnO_2 nano particles with diameters of about 5 nm. The lattice fringe spacings were measured to be 0.236 nm and 0.230 nm, corresponding to the (200) and (111) crystal planes of SnO_2, respectively. These results suggest that the MOF shell could protect SnO_2 nano particles from pulverization and a stable SEI could be retained outside MOF, which leads to the outstanding cyclic stability of the SnO_2@MOF/graphene composite.

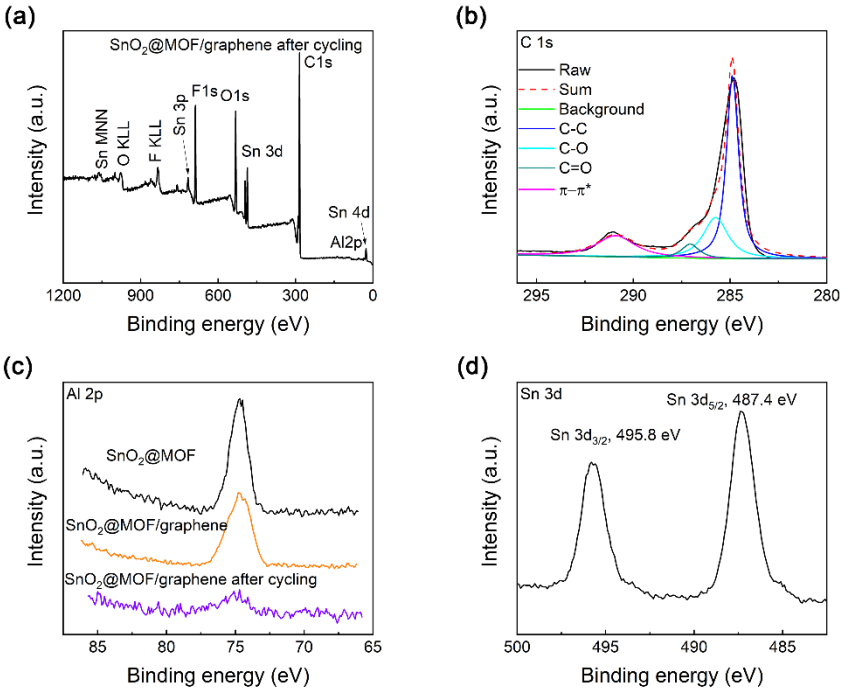

Figure 5-7 XPS survey spectrum (a), high-resolution spectra of C 1s (b), Al 2p (c) and Sn 3d (d) of the SnO2@MOF/graphene after 1000 cycles.

XPS spectra of the SnO_2@MOF/graphene composite after cycling were collected to investigate its chemical composition and bonding characters. As clearly seen in Figure 5-7, XPS survey proves the presence of Li, C, O, F, Al and Sn elements, which mainly originate from the formed SEI layer and the composite. The high-resolution of C 1s confirms the presence of C-C, C-O, C=O etc., corresponding to carbonate slats from SEI film and graphene sheets. The Al 2p for the as-prepared SnO_2@MOF and SnO_2@MOF/graphene, and the SnO_2@MOF/graphene after cycling display peaks at the same binding energy (74 eV), proving that the chemical environment of Al species is not altered by SnO_2 packing and lithiation/delithiation processes. Besides, the Sn 3d spectrum clearly displays two pronounced peaks at 495.8 for Sn $3d_{3/2}$ and 487.4 eV for Sn $3d_{5/2}$, which coincides well with those of the as-prepared SnO_2@MOF/graphene composite. The binding energy difference of 8.4 eV between these two peaks confirms the existence of SnO_2, suggesting that SnO_2 could be regenerated from LiO_2 and Sn after delithiation processes(74). Thus, the greatly enhanced capacity and prolong cycling stability should originate from the highly reversible reactions between SnO_2 nano particles trapped inside MOF and Li^+ ions.

5.3.2. ELECTROCHEMICAL CHARACTERIZATION AFTER CYCLING

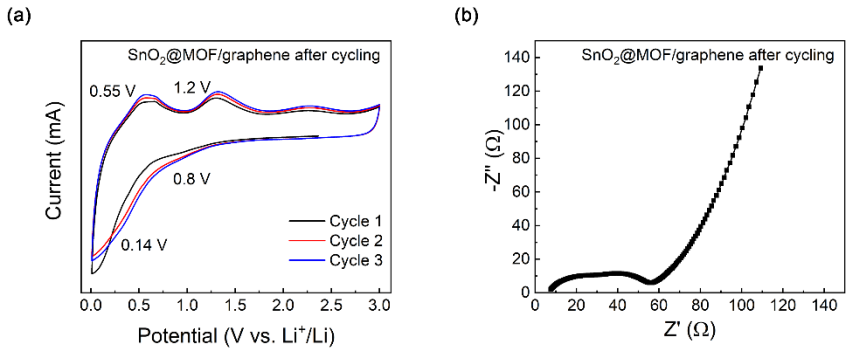

Figure 5-8 CV curves (a) and EIS spectrum (b) of SnO_2@MOF/graphene after cycling.

The CV curves of SnO_2@MOF/graphene after cycling were collected at a scan rate of 0.1 mV s^{-1} within voltage range from 0.01 to 3 V. Two redox peaks at 0.14/0.5 V and 0.8/1.2 V could be clearly noticed, which are consistent with those of the as-prepared composite(75). In addition, SnO_2@MOF/graphene after cycling present a similar EIS plot as that of as-prepared SnO_2@MOF/graphene (Figure 5-8b). These results indicate that the lithium storage mechanism of the SnO_2@MOF/graphene composite remains consistent throughout the cycling processes, that is, SnO_2@MOF/graphene composite exhibits an outstanding structural stability against repeated lithium insertion-extraction processes.

5.4. PROPOSED MECHANISM

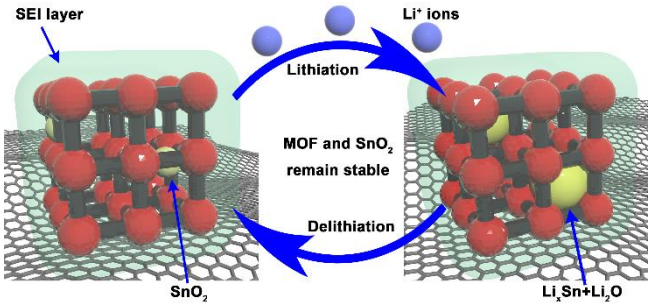

Scheme 5-1 Schematic illustration of the proposed mechanism for SnO_2@MOF/graphene after the formation of SEI film, during which the nanosized SnO_2 particles interact with Li^+ ions reversibly and the MOF matrix protects nanosized SnO_2 from collapsing.

To clarify the protecting role of the MOF matrix, a mechanism is proposed as depicted in Scheme 5-1. After the formation of the SEI layer during the first lithiation process, Li^+ ions diffuse through the SEI layer and then interact with nanosized SnO_2. The induced volume changes of SnO_2 could be accommodated by the MOF matrix and

graphene sheets because of their flexible while robust porous structure. These merits ensure that SnO_2 could react with Li^+ ions reversely to form Sn, Li_2O and then Li_xSn. The formed Sn nano particles are also confined within the MOF, preventing it from aggregation. In addition, Li_xSn could dealloy completely. During the whole charge-discharge processes, the structure of SnO_2@MOF/graphene composite remains stable, indicating the greatly enhanced cycling stability and capacity of the SnO_2@MOF/graphene composite.

5.5. SUMMARY

In this Chapter, a facile method was developed to prepare the nanosized SnO_2 particles within MOF, which acts as both template and protecting layer. Graphene sheets are also added to improve the electronic conductivity to obtain the better lithium storage performance of SnO_2 based materials as anodes for LIBs. Specifically, the SnO_2@MOF precursor was first prepared via a wet impregnation method and then the precursor was covered by the graphene sheets. The as-prepared SnO_2@MOF/graphene composite was assembled in an optimized ratio and exhibited greatly enhanced electrochemical performances compared to the pure SnO_2-based anode. Notably, this composite exhibits a capacity of 450 mA h g^{-1} at a current density of 1 A g^{-1} after 1000 cycles, whereas the pure SnO_2 anode almost lost its total capacity after only 50 cycles. This greatly enhanced performance of the SnO_2@MOF/graphene might result from the shortened Li^+ ions diffusion distance, superior electronic conductivity, rich accessible electroactive sites, and good structure stability.

In addition, the preparation approach developed in this Chapter is simple and economically effective. Hence, it is promising to up-scale this method to practical applications. This study provides new paths for rational designing of superior anode materials for high performance LIBs based on SnO_2 and other high-capacity anode materials.

CHAPTER 6. ELECTROCHEMICAL PERFORMANCE OF CO ZIF-62 (CRYSTALLINE, GLASSY, AMORPHOUS)

The electrochemical performance of crystalline ZIF, glassy ZIF and amorphous ZIF were evaluated in CR2032 coin-type cells. Detailed information could be found in paper III, which is in submission. Characterizations after cycling were also performed to investigate the impact of the structural difference on the lithium storage performance.

6.1. CYCLIC VOLTAMMETRY CURVES

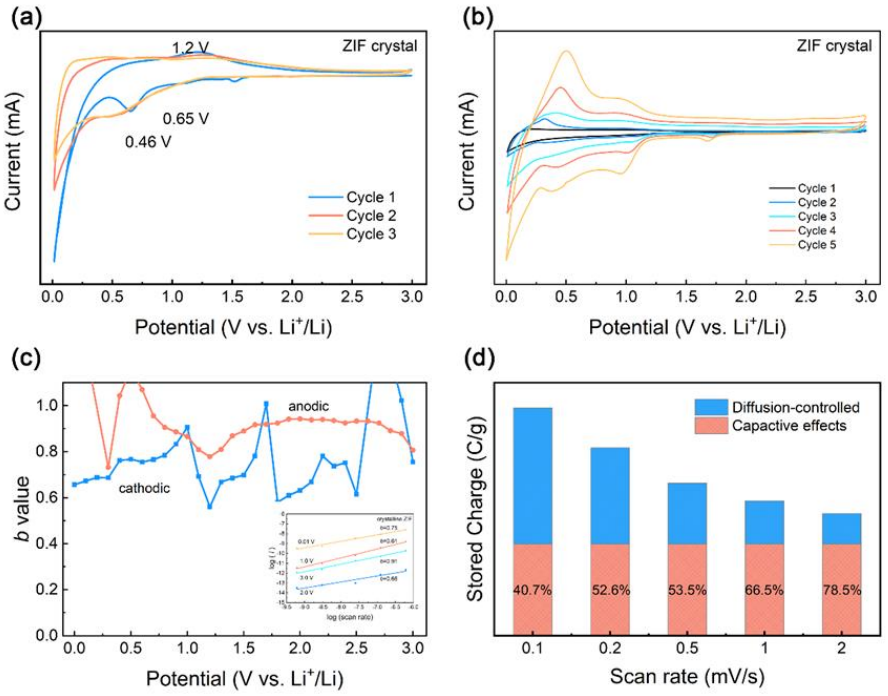

Figure 6-1 (a) Cyclic Voltammetry curves of crystalline ZIF within the range from 0.01 to 3.0 V at a scan rate of 0.1 mV s^{-1}. (b) Cyclic Voltammetry curves of crystalline ZIF under different scan rates of 0.1, 0.2, 0.5, 1 and 2 mV s^{-1}. (c) b values calculated from CV curves and (d) stored

charge and capacitive contributions calculated from CV curves under different scan rates. Inset in (c): log i vs. log v plots.

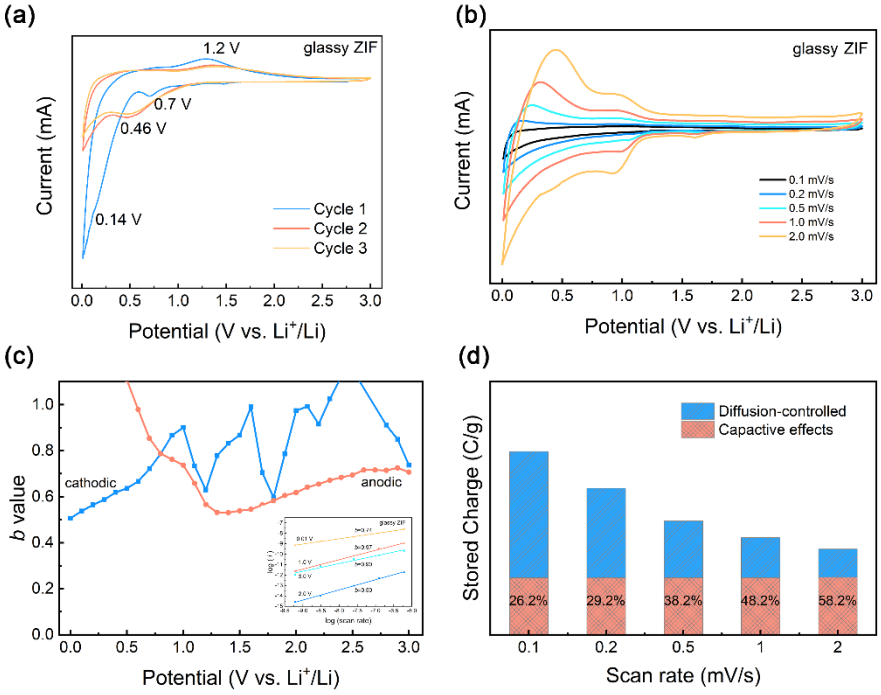

Figure 6-2 (a) Cyclic Voltammetry curves of glassy ZIF within the range from 0.01 to 3.0 V at a scan rate of 0.1 mV s^{-1}. (b) Cyclic Voltammetry under different scan rates of 0.1, 0.2, 0.5, 1 and 2 mV s^{-1}. (c) b values and (d) stored charge and capacitive contributions calculated from CV curves under different scan rates. Inset in (c): log i vs. log v plots.

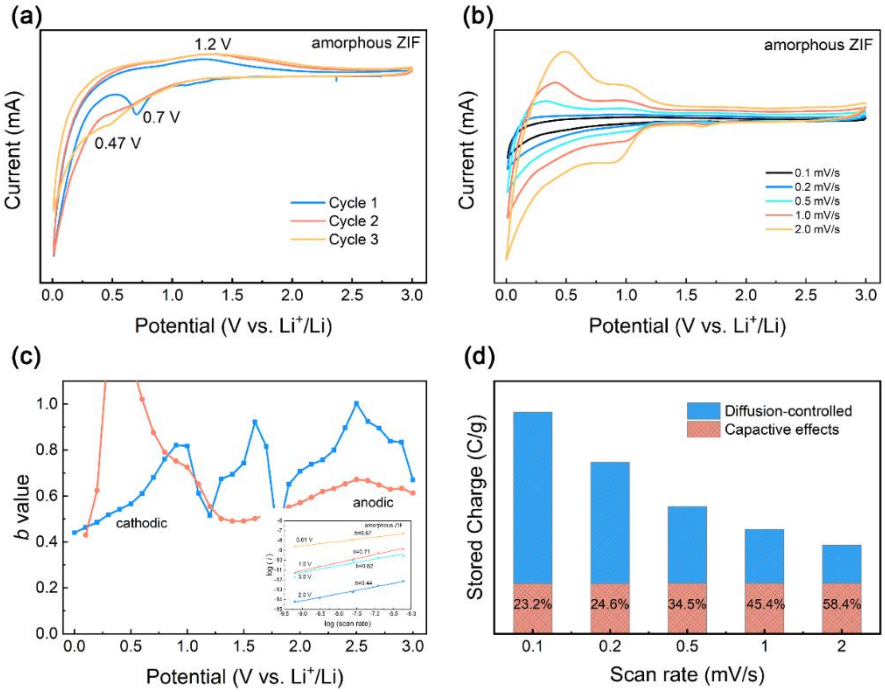

Figure 6-3 (a) Cyclic Voltammetry curves of amorphous ZIF within the range from 0.01 to 3.0 V at a scan rate of 0.1 mV s^{-1}. (b) Cyclic Voltammetry curves of amorphous ZIF under different scan rates of 0.1, 0.2, 0.5, 1 and 2 mV s^{-1}. (c) b values calculated from CV curves and (d) stored charge and capacitive contributions calculated from CV curves under different scan rates. Inset in (c): log i vs. log v plots.

To further investigate the electrochemical performance of the three ZIF anodes, the quantitative kinetic analyses were conducted based on the CV curves obtained at different scan rates within 0.1-2 mV s^{-1}. As shown in Figure 6-2a, the CV curves of glassy ZIF present reduction peaks at 0.7 and 0.14 V in the first cathodic scan, which might originate from insertion of Li^+ ions into ZIF and formation of solid electrolyte interface film (SEI), respectively(42). The oxidation peak at 1.2 V in the anodic scan is ascribed to the extraction of Li^+ ions from glassy ZIF. Then in subsequent two cycles, one couple of redox peaks (0.46/1.2 V) remains almost unchanged, corresponding to the reversible insertion/extraction of Li^+ ions into/from glassy ZIF. In Figure 6-1a and 6-3a, the CV curves of crystalline ZIF and amorphous ZIF anodes present almost the same redox peaks as those of glassy ZIF. This similarity further confirms that the identical lithium storage mechanisms are shared by these three ZIF samples even with different microstructures.

It is generally accepted that the total stored charges are determined by three contributors: 1) the faradaic contribution of the Li^+ ions insertion/extraction process (the diffusion-controlled capacity), 2) the faradaic contribution of the charge transfer

process with surface atoms (referred to as pseudocapacitance), 3) the non-faradaic contribution of the double-layer effect(39,40). The capacitive effects (pseudocapacitance and double-layer effect) could be characterized by analysing CV curves at various scan rates by using a power law relation between the current *i(V)* and the sweep rates *v* according to the following equation(40):

$$i(V) = av^b \qquad (6\text{-}1)$$

where *a* and *b* are fitting parameters, with *b*-values determined from the slope of the plot of log *i* vs log *v*. There are two well-confined conditions: $b = 0.5$ and $b = 1$. In detail, $b = 0.5$ represents a diffusion-controlled process, i.e., lithiation insertion process whereas $b = 1$ stands for the capacitive effects, i.e., capacitive process is dominant. A *b*-value between 0.5 and 1 suggests mixed contributions from both diffusion-controlled processes and capacitive effects. The *b* values of glassy ZIF anode are calculated at different potential for cathodic and anodic peaks, respectively (Figure 6-2c). The total capacity at a given scan rates (*v*) can be divided into two fractions (the diffusion-controlled fraction $k_2v^{1/2}$ and capacitive contribution k_1v) at a fixed potential (V) according to the following equation(41):

$$i(V) = k_1v + k_2v^{1/2} \qquad (6\text{-}2)$$

which could be rearranged to

$$i(V)/v^{1/2} = k_1v^{1/2} + k_2 \qquad (6\text{-}3)$$

where k_1 and k_2 can be evaluated by plotting $i(V)/v^{1/2}$ vs. $v^{1/2}$. Thus, after determining the k_1, the total capacitive contributions and total stored charge of glassy ZIF are shown in Figure 6-2d. It is noticed that capacitive effects contributed 26.2%, 28.0%, 38.2%, 48.2% and 58.2% at scan rates of 0.1, 0.2, 0.5, 1 and 2 mV s^{-1}, respectively. Interestingly, the capacitive contribution of crystalline ZIF is much larger than that of glassy ZIF and amorphous ZIF (Figure 6-1d and 6-3d). From above results, it could be concluded that the glassy ZIF and amorphous ZIF are mainly diffusion-controlled while the crystallin ZIF possesses large capacitive contribution due to the larger surface area than that of glassy ZIF and amorphous ZIF. The large fraction of diffusion-controlled Li^+ insertion of glassy ZIF might be one possible reason for its best performance.

6.2. GALVANOSTATIC CHARGE-DISCHARGE TESTS

6.2.1. CHARGE-DISCHARGE VOLTAGE PROFILES

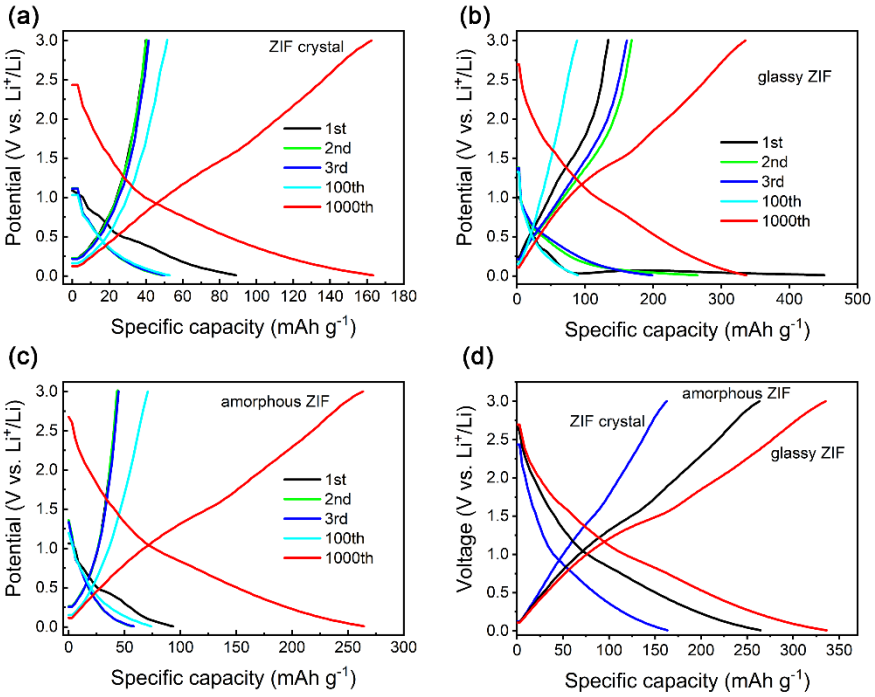

Figure 6-4 Galvanostatic charge/discharge profiles of the initial three, 100th and 1000th cycles of crystallin ZIF, glassy ZIF and amorphous ZIF and their comparison at the 1000th cycle at a current density of 1 A g^{-1}.

The electrochemical performances of the anodes made from the crystalline ZIF, glassy ZIF and amorphous ZIF, respectively, are characterized by galvanostatic charge/discharge cycling. As shown in Figure 6-4, these three anodes display similar charge-discharge profiles, in which the first cycle curve has a discharge-charge plateau at 0.14 and 1.2 V, respectively. In the following cycles, the discharge-charge plateaus of the three samples shift to 0.46 and 1.2 V, respectively, confirming the similar lithiation/delithiation processes of the three samples. As for the first charge-discharge cycle, crystalline ZIF, glassy ZIF and amorphous ZIF exhibit capacities of 89/40, 451/134 and 93/45 mAh g^{-1}, corresponding to Coulombic efficiency of 45%, 30% and 48%, respectively. Interestingly, all three samples exhibit capacity decays after 100 cycles while capacity enhancements after 1000 cycles. In detail, the glassy ZIF exhibit a capacity of 336 mAh g^{-1}, which is higher than those of crystalline ZIF (163 mAh g^{-1}) and amorphous ZIF (264 mAh g^{-1}). This variance of capacity enhancements might be related to their structural difference of these three samples.

6.2.2. CYCLIC PERFORMANCE

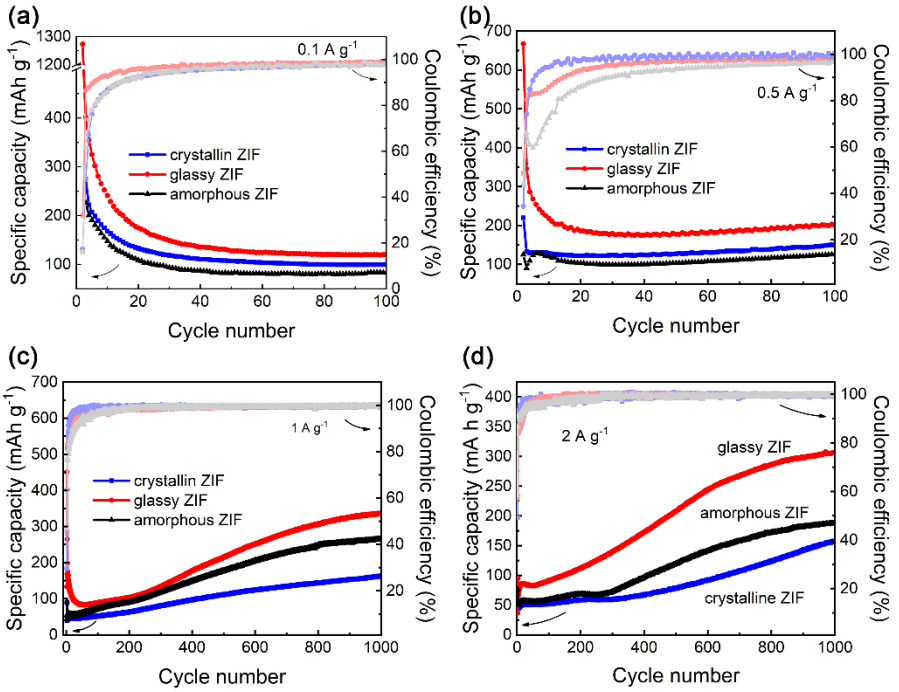

Figure 6-5 Cycling performance and Coulombic efficiency of crystalline ZIF, glassy ZIF and amorphous under current densities of (a) 0.1, (b) 0.5 A g^{-1} for 100 cycles, and (c) 1, (d) 2 A g^{-1} for 1000 cycles.

The cycling performances and Coulombic efficiency (CE) of the three above-mentioned anodes are evaluated at 0.1, 0.5, 1 and 2 A g^{-1} (Figure 6-5). At 0.1 and 0.5 A g^{-1}, these three samples show similar trend, i.e., the capacities drop in the first 20 cycles and remain stable until 100 cycles. In detail, the starting discharge capacity (670 mAh g^{-1}) of the glassy ZIF is significantly higher than those of other two samples (220 mAh g^{-1} for crystalline ZIF and 125 mAh g^{-1} for amorphous ZIF) at 0.5 A g^{-1}. However, the capacity of the glassy ZIF anode decays to about 200 mAh g^{-1} after 20 cycles. This capacity is still higher than those of both the crystalline ZIF (149 mAh g^{-1}) and amorphous ZIF (125 mAh g^{-1}). The CEs for the first cycle are 49%, 30% and 47% of three samples, these low CEs might be originated from SEI growth and other irreversible reactions during the first lithiation process. Notably, the glassy ZIF exhibit the largest capacity while the lowest CE. In Figure 6-5 c and d, an unusual phenomenon is noticed, that is, the three samples display a continuous increase of the capacity during 1000 cycles at 1 and 2 A g^{-1}. Specifically, the capacities of crystalline ZIF, glassy ZIF and amorphous ZIF have reached 157, 188 and 306 mAh g^{-1}, respectively, after 1000 cycles at 2 A g^{-1}. It is clearly observed that, compared to

crystalline ZIF and amorphous ZIF, the glassy ZIF shows a significantly greater enhancement in capacity after 1000 cycles, i.e., its capacity is tripled relative to the initial value of 95 mAh g^{-1}. Under the same conditions, both crystalline ZIF and amorphous ZIF exhibit the capacity enhancement as well, but to a lesser extent compared with that of glassy ZIF anode (from 77 to 158 mAh g^{-1} for crystalline ZIF and from 76 to 188 mAh g^{-1} for amorphous ZIF). When comparing the cycling curves between the amorphous ZIF and crystalline ZIF, it is obvious that the former shows slightly higher capacity than the latter throughout 1000 cycles. Further studies are needed to reveal the reasons for this unusual and unique cycling-induced capacity enhancement of the glass anode.

As mentioned early, the capacity of crystalline ZIF is also gradually enhanced during the cycling process. The reasons for this enhancement might be explained by the weak coordination bonds between cobalt nodes and nitrogen atoms in the Im/BIm ligands. During cycling, some of these bonds may easily be broken by Li^+ ion insertion/extraction, and thus the tetrahedral $Co(Im/BIm)_4$ network is partially depolymerized. This leads to the formation of larger channels (compared to the original ones), and hence, an increasing amount of Li^+ ions can be transferred and stored in crystalline ZIF. As for the amorphous ZIF, it contained numerous defects, which could function as active sites for lithium storage. Thus, the capacity of the amorphous ZIF anode is also enhanced compared with crystalline ZIF.

6.2.3. RATE PERFORMANCE

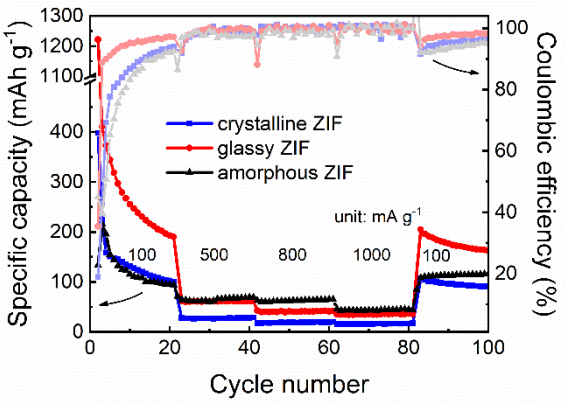

Figure 6-6 Rate performance of the three samples at current densities of 100, 500, 800, 1000 and 100 mA g^{-1} for 20 cycles.

As shown in Figure 6-6, the rate capacities of the three samples are evaluated at the current densities of 100, 500, 800 and 1000 mA g^{-1}, at each of which 20 cycles of discharging/charging are conducted. It is clearly seen that capacities drops with increasing current densities while the capacity could be fully retained if the current is

switch back to 100 mA g^{-1}. Specifically, glassy ZIF delivers average capacities of 238, 63, 51 and 37 mAh g^{-1} after 20 cycles at 100, 500, 800 and 1000 mA g^{-1}, respectively. Remarkably, after the current density is switched back to 100 mA g^{-1}, the anode can fully recover its capacity back to about 172 mAh g^{-1}. Apparently, the capacities delivered by the glassy ZIF are much larger than those of both crystalline ZIF and amorphous ZIF at the same conditions.

6.2.4. ELECTROCHEMICAL IMPEDANCE SPECTRA

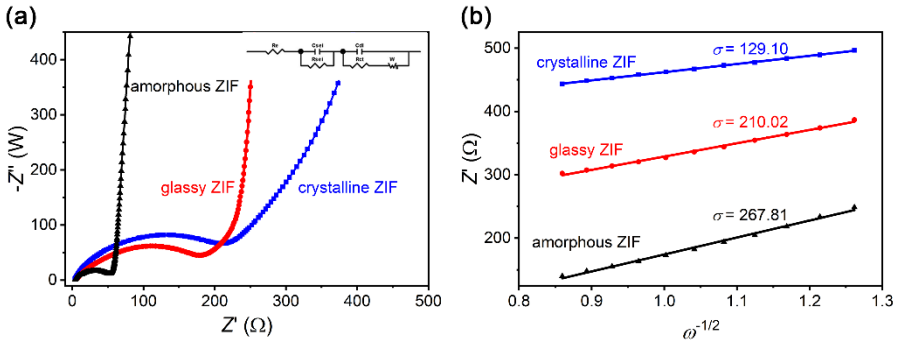

Figure 6-7 (a) Nyquist plots obtained from electrochemical impedance spectra of the three samples within frequency range from 0.01 to 10 kHz with an amplitude of 10 mV. Inset: the equivalent circuit model. (b) Z' vs. $\omega^{-1/2}$ plots in the low frequency region obtained from Nyquist plots.

To observe the difference in electrical resistance among the three ZIF anodes, we conducted electrochemical impedance spectroscopy measurement as shown in Figure 6-7a. It is seen that the Nyquist plots of the three anodes consist of a depressed semicircle in high frequency range and a straight line at low frequency end. The equivalent circuit model of the experimental curves is also shown in Figure 6-7a. The R_b (bulk resistance of the cell) of all three samples are found to be 3.5, 7.6 and 4.0 Ω, respectively (Table 6-1). The R_{ct} (charge transfer resistance) of the amorphous ZIF is the smallest (52 Ω) among the three samples, indicating the highest electrical conductivity. The low-frequency sloping line is ascribed to the Warburg impedance, which is associated with the diffusion of Li^+ ions in the electrode material. Then, the apparent Li^+ ion diffusion coefficient D of these three samples are calculated from the incline line in the Warburg region using equation(76):

$$D=R^2T^2/2A^2n^4F^4C^2\sigma^2 \qquad (6\text{-}4)$$

where R is the gas constant, T is the absolute room temperature, A is the surface area of the electrode (~1.13 cm^2), n is the number of electron transferred during oxidation, F is the Faraday constant, C is the Li^+ concentration, and σ is the Warburg factor

associated with Z_{re} ($Z_{re} \propto \sigma\omega^{-1/2}$). σ can be determined from the linear relation between Z_{re} and the reciprocal square root of the angular frequency ω (Figure 6-7b).

	R_e (Ω)	R_{ct} (Ω)	C (F)
crystalline ZIF	2.68	258	0.72
glassy ZIF	4.95	218	0.64
amorphous ZIF	3.57	52	0.79

Table 6-1 Calculated values of components from EIS equivalent circuit model.

By introducing σ into Equation (6-4), we can calculate the apparent Li^+ diffusion coefficient D since the temperature and other constants are known. Thus, the D values of crystalline ZIF, glassy ZIF and amorphous ZIF are found to be 2.82×10^{-14}, 1.06×10^{-14} and 6.54×10^{-15} $cm^2\ s^{-1}$, respectively.

6.3. CHARACTERIZATIONS AFTER CHARGE-DISCHARGE CYCLING

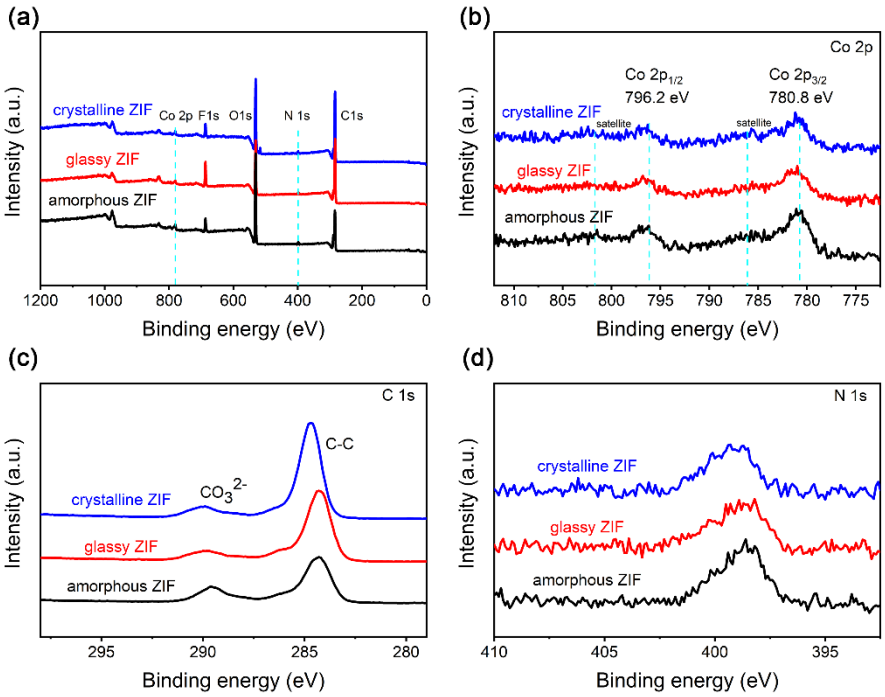

Figure 6-8 (a) XPS survey spectra, high-resolution spectra of (b) Co 2p, (c) C 1s, (d) N 1s of crystalline ZIF, glassy ZIF and amorphous ZIF after 1000 charge-discharge cycles at 1 A g^{-1}, respectively.

To confirm verify that the electrochemical performance differences among the three samples arise from their structural difference, the XPS spectra were collected of the anodes that have been subjected to 1000 charge-discharge cycles at 1 A g^{-1} (Figure 6-8). These three samples present similar survey spectra. In Figure 6-8a, it is clearly seen that F and O are present in all three samples, which originate from the SEI film. To find out whether cycling processes affect the valence state of cobalt, the Co 2p spectrum are highlighted in Figure 6-8b, which exhibits two peaks at 796.2 eV (Co $2p_{1/2}$) and 780.8 eV (Co $2p_{3/2}$) with two satellite peaks, indicating the existence of Co^{2+}. This result suggests that the valence state of Co is not influenced by 1000 charge-discharge cycles for all the three samples. In addition, the high-resolution spectra of C 1s and N 1s also remain unchanged upon cycling in evidenced in Figures 6-8 c and d. The CO_3^{2-} peaks for the cycled samples originate from SEI layer (Figure 6-8c). All the XPS results suggest that both the metal nodes and organic ligands in all ZIF samples remain unaltered after 1000 charge-discharge cycles.

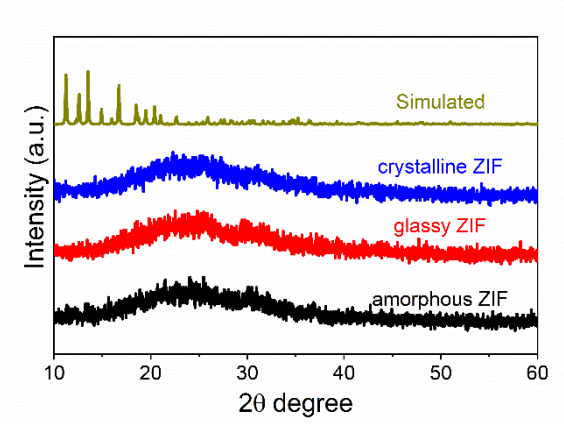

Figure 6-9 XRD patterns of crystalline ZIF, glassy ZIF and amorphous ZIF after 1000 charge-discharge cycles at 1 A g^{-1}, respectively.

To study the structure evolution during cycles, the ex-situ XRD patterns were also collected (Figure 6-9). It is striking that crystalline ZIF lose its long-range order by the order-disorder transition(48). In contrast, both glassy ZIF and amorphous ZIF maintain their original disordered structure after cycling, as no diffraction peaks appear.

6.4. PROPOSED MECHANISM

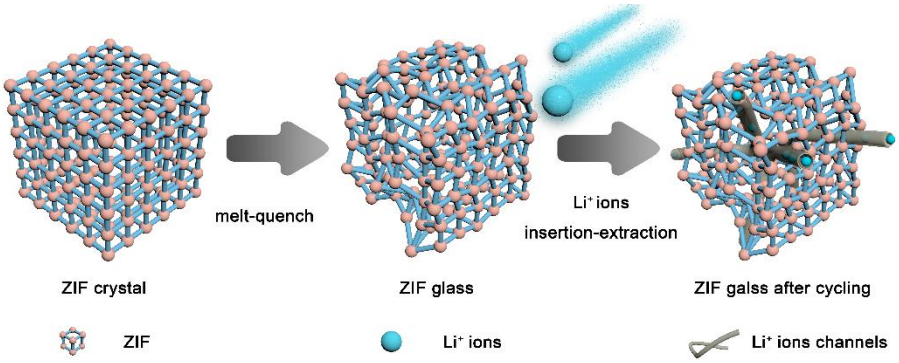

Scheme 6-1 The schematic representation of the structural origin of the capacity enhancement in glassy ZIF anode.

Based on the above discussions, the mechanism of the cycling-induced capacity enhancement in glassy ZIF anode may be schematically illustrated in Scheme 6-1. Upon heating, crystalline ZIF is melted, and thereby its network structure becomes disordered at all length scales (short-, medium- and long-range)(77,78). Upon quenching, the disordered structure is frozen-in in the glass state with higher potential energy (compared with crystal state). Once the Li^+ ions are inserted into the network structure, they will affect and disrupt the coordination bonds, and hence, generating new channels for Li^+ ion diffusion and storage. Consequently, the capacity of the glass anode substantially increases with cycling. Moreover, the short-range disorder in glassy ZIF structure enables shortening the diffusion distance of Li^+ ions, benefiting the ionic transfer kinetics. In addition, the high-energy state of glassy ZIF makes the network structure easily be distorted and depolymerized by insertion/extraction of Li^+ ions during charge-discharge cycles, and this favours the formation of new channels for Li^+ ion diffusion and storage. Thus, this type of glassy ZIF (i.e., melt-quench Co ZIF-62 glass) exhibit great potential to be a promising anode material for fabricating superior Li-ion batteries.

6.5. SUMMARY

In this Chapter, we prepared the first-ever glassy ZIF anode for LIBs, which exhibits superior lithium storage performances such as higher capacity, greater rate capability and long-term cyclability, compared to its counterpart crystalline ZIF. Strikingly, this glassy ZIF (melt-quench Co ZIF-62 glass) exhibits a tripled increase of the specific capacity (up to 306 mA h g^{-1}) after 1000 cycles at the current density of 2 A g^{-1}. The outstanding electrochemical performances of glassy ZIF might be ascribed to its unique structure characterized by a high degree of disorder at all scales and higher

energy state nature. This encouraging discovery provides us a new path to design anode materials for superior Li-ion batteries by using MOF glasses.

CHAPTER 7. CONCLUSION AND PERSPECTIVE

7.1. CONCLUSION

Although metal-organic frameworks (MOFs) have received growing attention due to their special properties, their application potential in energy storage, especially in LIBs, are still waiting to be fulfilled. There are some great reports about using MOFs as template to fabricate metal oxide and carbon composite for energy storage, while the MOFs themselves also hold huge potential, which are main points of this thesis. In detail, three aspects of MOFs are investigated and developed as anode materials for LIBs: (1) the pristine MOFs used as anode materials directly and the structure evolution due to the interaction between MOFs and lithium insertion/extraction (Chapter 4); (2) MOFs acting as protecting layer as well as template to prepare MOF-based composite (Chapter 5); (3) the impact of structure differences of MOF crystal and MOF glass on the lithium storage performance (Chapter 6). Highlights are presented as follows:

In order to explore the impact of lithiation/delithiation on the structure of MOFs, a Al-MOF (chemical formula: $Al(OH)[O_2C–C_6H_4–CO_2]$) was studied as an example. The Al-MOF was covered by graphene sheets to get Al-MOF/graphene composite, which was evaluated as anode material for LIBs. It is intriguing to notice that a pronounced structural change in the Al-MOF particles induced by the lithiation/delithiation, which manifests as an order-disorder transition. This transition could lead to the more open channels and voids, thereby benefiting the diffusion and storage of Li^+ ions. This work suggests that both the lithiation/delithiation induced order-disorder transition in MOFs and the optimized wrapping of MOF by graphene are crucial for enhancing the capacity and the cycling stability of MOF-based anode materials.

Beside acting as anode materials, MOFs could play a role in protecting SnO_2 from pulverization, which could contribute to an enhanced cycling stability. To fulfill this strategy, SnO_2 nanoparticles are in-situ packed into an Al-MOF in an optimum mass ratio, and then the derived SnO_2@MOF composite is wrapped by graphene sheets, finally resulting in the SnO_2@MOF/graphene composite. This composite exhibits greatly enhanced cycling stability, which originate from the unique structural configuration of the composite that provides rich accessible electroactive sites, shortened ion transport pathways, and superior electronic conductivity. The MOF protection layer is a key for improving the cycling stability of SnO_2 anode materials. Proved by this work, MOFs could also act as a template and host matrix to obtain materials with better lithium storage performance.

In addition, the discover of MOF glass, a new family of glass material, inspired us to explore the possibility of using MOF glass as anode materials besides crystalline MOF. Therefore, the first-ever MOF glass (Co ZIF-62 melt-quench glass) anode for LIBs was developed. This type of anode exhibits superior lithium storage performances including higher capacity, greater rate capability and long-term cyclability, compared to its counterpart crystalline ZIF. Astonishingly, glassy ZIF exhibits a tripled increase of the specific capacity (up to 306 mA h g^{-1}) after 1000 cycles at the current density of 2 A g^{-1}. The outstanding electrochemical performances of the MOF glass have been ascribed to its unique structure characterized by a high degree of disorder at all scales and higher energy state nature. This encouraging discovery sheds light on a new way us to develop the next generation of anodes for superior Li^+ ion batteries by using MOF glasses.

7.2. PERSPECTIVE

The outcomes of this thesis shed light on the development of MOF-based materials for LIBs, while following research topics are still needed to be fully investigated.

The lithium storage mechanism of MOF is still unclear, future experiment and analyses are needed. Recent studies report proposed a possible mechanism that carboxylate group from organic ligands could react with Li^+ ions to give reversible capacity(66,79). While there is still no direct evidence to prove this insertion mechanism, more advanced characterization technologies, such as in-situ XRD, in-situ NMR, etc., are urgently needed to explore the actual lithium storage mechanism in MOFs. With the more studies with MOFs, the more interesting properties and phenomena could be revealed, which would facilitate the development of MOF-based materials for LIBs as well as other research fields, such as catalysis, gas separation and storage.

Furthermore, the reason why some MOFs anode exhibit gradually increasing capacity and experience order-disorder transition along with cycling is still debatable. In addition, the origin of growing capacities of both crystalline and amorphous MOF is still lack of solid evidence. Thus, the performance-structure relationship of MOFs should be clarified if we want to design and prepare electrode materials with better cycling stability. In summary, to fabricate electrode materials for advanced LIBs with ultra-long lifetime, there are still numerous opportunities in MOFs.

BIOGRAPHY

1. Trahey L, Brushett FR, Balsara NP, Ceder G, Cheng L, Chiang YM, et al. Energy storage emerging: A perspective from the Joint Center for Energy Storage Research. Proc Natl Acad Sci U S A. 2020 Jun 9;117(23):12550–7.

2. Stenclik D, Denholm P, Chalamala B. Maintaining Balance: The Increasing Role of Energy Storage for Renewable Integration. IEEE Power Energy Mag. 2017 Nov 1;15(6):31–9.

3. Parra D, Swierczynski M, Stroe DI, Norman SA, Abdon A, Worlitschek J, et al. An interdisciplinary review of energy storage for communities: Challenges and perspectives. Vol. 79, Renewable and Sustainable Energy Reviews. Elsevier Ltd; 2017. p. 730–49.

4. Goodenough JB, Kim Y. Challenges for rechargeable Li batteries. Chem Mater. 2010 Feb 9;22(3):587–603.

5. Goodenough JB, Park KS. The Li-ion rechargeable battery: A perspective. J Am Chem Soc. 2013;135(4):1167–76.

6. Li T, Bai Y, Wang Y, Xu H, Jin H. Advances in transition-metal (Zn, Mn, Cu)-based MOFs and their derivatives for anode of lithium-ion batteries. Coord Chem Rev. 2020;410:213221.

7. Crabtree G, Kócs E, Trahey L. The energy-storage frontier: Lithium-ion batteries and beyond. MRS Bull. 2015 Nov 27;40(12):1067–76.

8. Myung ST, Kumagai N, Komaba S, Chung HT. Effects of Al doping on the microstructure of LiCoO2 cathode materials. Solid State Ionics. 2001;139(1–2):47–56.

9. Masquelier C, Padhi AK, Nanjundaswamy KS, Goodenough B. New cathode materials for rechargeable lithium batteries: the 3-D framework structures Li/sub 3/Fe/sub 2/(XO/sub 4/)/sub 3/ (X=P,As). J Solid State Chem. 1998;135(2):228–34.

10. Lee HW, Muralidharan P, Ruffo R, Mari CM, Cui Y, Kim DK. Ultrathin spinel LiMn2O4 nanowires as high power cathode materials for Li-ion batteries. Nano Lett. 2010;10(10):3852–6.

11. Goodenough JB. Cathode materials: A personal perspective. J Power Sources. 2007;174(2):996–1000.

12. Cui L-F, Yang Y, Hsu C-M, Cui Y. Carbon−Silicon Core−Shell Nanowires as High Capacity Electrode for Lithium Ion Batteries. Nano Lett. 2009;9(9):3370–4.

13. Nazir A, Le HTT, Min C-W, Kasbe A, Kim J, Jin C-S, et al. Coupling of a conductive Ni 3 (2,3,6,7,10,11-hexaiminotriphenylene) 2 metal–organic framework with silicon nanoparticles for use in high-capacity lithium-ion batteries. Nanoscale. 2020;1629–42.

14. Landi BJ, Ganter MJ, Cress CD, DiLeo RA, Raffaelle RP. Carbon nanotubes for lithium ion batteries. Energy Environ Sci. 2009 Jun 2;2(6):638–54.

15. Flandrois S, Simon B. Carbon materials for lithium-ion rechargeable batteries. Carbon N Y. 1999;37(2):165–80.

16. Wu YP, Rahm E, Holze R. Carbon anode materials for lithium ion batteries. J Power Sources. 2003 Mar 12;114(2):228–36.

17. Zeng Z, Liang WI, Liao HG, Xin HL, Chu YH, Zheng H. Visualization of electrode-electrolyte interfaces in LiPF 6/EC/DEC electrolyte for lithium ion batteries via in situ TEM. Nano Lett. 2014 Apr 9;14(4):1745–50.

18. Wu X, Wang Z, Chen L, Huang X. Ag-enhanced SEI formation on Si particles for lithium batteries. Electrochem commun. 2003;5(11):935–9.

19. Lou X-W (David). Co3O4 Hollow Nanoparticles Embedded in Mesoporous Walls of Carbon Nanoboxes for Efficient Lithium Storage. Angew Chemie Int Ed. 2020 Jul 22;17(11):anie.202008987.

20. Idota Y, Kubota T, Matsufuji A, Maekawa Y, Miyasaka T. Tin-based amorphous oxide: A high-capacity lithium-ion-storage material. Science. 1997 May 30;276(5317):1395–7.

21. Paek SM, Yoo EJ, Honma I. Enhanced cyclic performance and lithium storage capacity of SnO 2/graphene nanoporous electrodes with three-dimensionally delaminated flexible structure. Nano Lett. 2009;9(1):72–5.

22. Liu J, Cheng M, Han T, Lu Q, Zhang H, Zhou P, et al. A Novel Mechanically Robust Leaf-Shaped Tin Dioxide Li-Ion Battery Anode and Its Dynamic Structural Transformation and Electron-Transfer Simulation. Energy Technol. 2020;1901149:1–6.

23. Mesgarian R, Heydarinasab A, Rashidi A, Zamani Y. Adsorption and growth of water clusters on UiO-66 based nanoadsorbents: A systematic and

comparative study on dehydration of natural gas. Sep Purif Technol. 2020;239(December 2019):116512.

24. Tian T, Zeng Z, Vulpe D, Casco ME, Divitini G, Midgley PA, et al. A sol–gel monolithic metal–organic framework with enhanced methane uptake. Nat Mater. 2017;17(February).

25. Ye Y, Gong L, Xiang S, Zhang Z, Chen B. Metal-Organic Frameworks as a Versatile Platform for Proton Conductors. Adv Mater. 2020;1907090:1907090.

26. Zhang W, Lu G, Cui C, Liu Y, Li S, Yan W, et al. A family of metal-organic frameworks exhibiting size-selective catalysis with encapsulated noble-metal nanoparticles. Adv Mater. 2014;26(24):4056–60.

27. Feng S, Zhang X, Shi D, Wang Z. Zeolitic imidazolate framework-8 (ZIF-8) for drug delivery: A critical review. Front Chem Sci Eng. 2020;8.

28. Bagheri M, Masoomi MY. Sensitive Ratiometric Fluorescent Metal-Organic Framework Sensor for Calcium Signaling in Human Blood Ionic Concentration Media. ACS Appl Mater Interfaces. 2020;12(4):4625–31.

29. Yaghi OM, Li H. Hydrothermal Synthesis of a Metal-Organic Framework Containing Large Rectangular Channels. J Am Chem Soc. 1995;117(41):10401–2.

30. Li X, Cheng F, Zhang S, Chen J. Shape-controlled synthesis and lithium-storage study of metal-organic frameworks Zn4O(1,3,5-benzenetribenzoate)2. J Power Sources. 2006 Sep;160(1):542–7.

31. Saravanan K, Nagarathinam M, Balaya P, Vittal JJ. Lithium storage in a metal organic framework with diamondoid topology-A case study on metal formates. J Mater Chem. 2010;20(38):8329–35.

32. Liu Q, Yu L, Wang Y, Ji Y, Horvat J, Cheng ML, et al. Manganese-based layered coordination polymer: Synthesis, structural characterization, magnetic property, and electrochemical performance in lithium-ion batteries. Inorg Chem. 2013;52(6):2817–22.

33. Gou L, Hao LM, Shi YX, Ma SL, Fan XY, Xu L, et al. One-pot synthesis of a metal-organic framework as an anode for Li-ion batteries with improved capacity and cycling stability. J Solid State Chem. 2014;210(1):121–4.

34. Hummers WS, Offeman RE. Preparation of Graphitic Oxide. J Am Chem Soc.

1958;80(6):1339.

35. Stankovich S, Dikin DA, Piner RD, Kohlhaas KA, Kleinhammes A, Jia Y, et al. Synthesis of graphene-based nanosheets via chemical reduction of exfoliated graphite oxide. Carbon N Y. 2007;45(7):1558–65.

36. Marcano DC, Kosynkin D V., Berlin JM, Sinitskii A, Sun Z, Slesarev A, et al. Improved synthesis of graphene oxide. ACS Nano. 2010;4(8):4806–14.

37. Loiseau T, Serre C, Huguenard C, Fink G, Taulelle F, Henry M, et al. A Rationale for the Large Breathing of the Porous Aluminum Terephthalate (MIL-53) Upon Hydration. Chem Eur J. 2004 Mar 19;10(6):1373–82.

38. Ahsan R, Khan MZR, Basith MA. Determination of optical band gap of powder-form nanomaterials with improved accuracy. J Nanophotonics. 2017;11(04):1.

39. Conway BE, Birss V, Wojtowicz J. The role and utilization of pseudocapacitance for energy storage by supercapacitors. J Power Sources. 1997;66(1–2):1–14.

40. Lindström H, Södergren S, Solbrand A, Rensmo H, Hjelm J, Hagfeldt A, et al. Li+ ion insertion in TiO2 (anatase). 2. Voltammetry on nanoporous films. J Phys Chem B. 1997;101(39):7717–22.

41. Liu T-C. Behavior of Molybdenum Nitrides as Materials for Electrochemical Capacitors. J Electrochem Soc. 1998;145(6):1882.

42. Li C, Lou X, Yang Q, Zou Y, Hu B. Remarkable improvement in the lithium storage property of Co2(OH)2BDC MOF by covalent stitching to graphene and the redox chemistry boosted by delocalized electron spins. Chem Eng J. 2017 Oct;326:1000–8.

43. Bezverkhyy I, Ortiz G, Chaplais G, Marichal C, Weber G, Bellat JP. MIL-53(Al) under reflux in water: Formation of γ-AlO(OH) shell and H2BDC molecules intercalated into the pores. Microporous Mesoporous Mater. 2014;183:156–61.

44. Ferrari AC, Meyer JC, Scardaci V, Casiraghi C, Lazzeri M, Mauri F, et al. Raman spectrum of graphene and graphene layers. Phys Rev Lett. 2006;97(18):187401.

45. Yang D, Velamakanni A, Bozoklu G, Park S, Stoller M, Piner RD, et al. Chemical analysis of graphene oxide films after heat and chemical treatments

by X-ray photoelectron and Micro-Raman spectroscopy. Carbon N Y. 2009;47(1):145–52.

46. Zhao H, Song H, Chou L. Nickel nanoparticles supported on MOF-5: Synthesis and catalytic hydrogenation properties. Inorg Chem Commun. 2012;15:261–5.

47. Jiao Y, Han D, Ding Y, Zhang X, Guo G, Hu J, et al. Fabrication of three-dimensionally interconnected nanoparticle superlattices and their lithium-ion storage properties. Nat Commun. 2015;6:1–8.

48. Gao C, Wang P, Wang Z, Kær SK, Zhang Y, Yue Y. The disordering-enhanced performances of the Al-MOF/graphene composite anodes for lithium ion batteries. Nano Energy. 2019 Nov;65(July):104032.

49. Liang J, Yu XY, Zhou H, Wu H Bin, Ding S, Lou XW. Bowl-like SnO2@carbon hollow particles as an advanced anode material for lithium-ion batteries. Angew Chemie - Int Ed. 2014 Nov 17;53(47):12803–7.

50. Diéguez A, Romano-Rodríguez A, Vilà A, Morante JR. The complete Raman spectrum of nanometric SnO2 particles. J Appl Phys. 2001;90(3):1550–7.

51. Gu F, Fen Wang S, Feng Song C, Kai Lü M, Xin Qi Y, Jun Zhou G, et al. Synthesis and luminescence properties of SnO2 nanoparticles. Chem Phys Lett. 2003 Apr;372(3–4):451–4.

52. Gao S, Wang N, Li S, Li D, Cui Z, Yue G, et al. A Multi-Wall Sn/SnO 2 @Carbon Hollow Nanofiber Anode Material for High-Rate and Long-Life Lithium-Ion Batteries . Angew Chemie. 2020;132(6):2486–93.

53. Tu B, Shao Y, Chen W, Wu Y, Li X, He Y, et al. Novel Molecular Doping Mechanism for n-Doping of SnO 2 via Triphenylphosphine Oxide and Its Effect on Perovskite Solar Cells. Adv Mater. 2019;31(15):1–9.

54. Qiao A, Bennett TD, Tao H, Krajnc AA, Mali G, Doherty CM, et al. A metal-organic framework with ultrahigh glass-forming ability. Sci Adv. 2018 Mar 9;4(3):eaao6827.

55. Banerjee R, Phan A, Wang B, Knobler C, Furukawa H, O'Keeffe M, et al. High-throughput synthesis of zeolitic imidazolate frameworks and application to CO2 capture. Science. 2008 Feb 15;319(5865):939–43.

56. Gustafsson M, Zou X. Crystal formation and size control of zeolitic imidazolate frameworks with mixed imidazolate linkers. J Porous Mater.

2013 Feb 22;20(1):55–63.

57. Stepniewska M, Østergaard MB, Zhou C, Yue Y. Towards large-size bulk ZIF-62 glasses via optimizing the melting conditions. J Non Cryst Solids. 2020 Feb;530(December 2019):119806.

58. Frentzel-Beyme L, Kloß M, Pallach R, Salamon S, Moldenhauer H, Landers J, et al. Porous purple glass-a cobalt imidazolate glass with accessible porosity from a meltable cobalt imidazolate framework. J Mater Chem A. 2019;7(3):985–90.

59. Schneemann A, Bon V, Schwedler I, Senkovska I, Kaskel S, Fischer RA. Flexible metal-organic frameworks. Chem Soc Rev. 2014;43(16):6062–96.

60. Gadipelli S, Travis W, Zhou W, Guo Z. A thermally derived and optimized structure from ZIF-8 with giant enhancement in CO2 uptake. Energy Environ Sci. 2014;7(7):2232–8.

61. Wong CP, Miller PJ. Vibrational spectroscopic studies of alane. J Energ Mater. 2005;23(3):169–81.

62. Hu C, Huang YC, Chang AL, Nomura M. Amine functionalized ZIF-8 as a visible-light-driven photocatalyst for Cr(VI) reduction. J Colloid Interface Sci. 2019;553:372–81.

63. Zhang S, Ding MS, Xu K, Allen J, Jow TR. Understanding Solid Electrolyte Interface Film Formation on Graphite Electrodes. Electrochem Solid-State Lett. 2001;4(12):A206.

64. Chen H, Armand M, Demailly G, Dolhem F, Poizot P, Tarascon JM. From biomass to a renewable LiXC6O6 organic electrode for sustainable li-ion batteries. ChemSusChem. 2008;1(4):348–55.

65. Zhang SS, Xu K, Jow TR. EIS study on the formation of solid electrolyte interface in Li-ion battery. Electrochim Acta. 2006;51(8–9):1636–40.

66. Armand M, Grugeon S, Vezin H, Laruelle S, Ribière P, Poizot P, et al. Conjugated dicarboxylate anodes for Li-ion batteries. Nat Mater. 2009;8(2):120–5.

67. Ding S, Chen JS, Qi G, Duan X, Wang Z, Giannelis EP, et al. Formation of SnO2 hollow nanospheres inside mesoporous silica nanoreactors. J Am Chem Soc. 2011;133(1):21–3.

68. Huang JY, Zhong L, Wang CM, Sullivan JP, Xu W, Zhang LQ, et al. In situ observation of the electrochemical lithiation of a single SnO 2 nanowire electrode. Science. 2010;330(6010):1515–20.

69. Zhou X, Wan L-J, Guo Y-G. Binding SnO 2 Nanocrystals in Nitrogen-Doped Graphene Sheets as Anode Materials for Lithium-Ion Batteries. Adv Mater. 2013 Apr 18;25(15):2152–7.

70. Hu R, Zhang H, Lu Z, Liu J, Zeng M, Yang L, et al. Unveiling critical size of coarsened Sn nanograins for achieving high round-trip efficiency of reversible conversion reaction in lithiated SnO2 nanocrystals. Nano Energy. 2018;45(January):255–65.

71. Kim C, Noh M, Choi M, Cho J, Park B. Critical size of a nano SnO2 electrode for Li-secondary battery. Chem Mater. 2005;17(12):3297–301.

72. Zhang SS, Xu K, Jow TR. Electrochemical impedance study on the low temperature of Li-ion batteries. Electrochim Acta. 2004;49(7):1057–61.

73. Ho C. Application of A-C Techniques to the Study of Lithium Diffusion in Tungsten Trioxide Thin Films. J Electrochem Soc. 1980;127(2):343.

74. Kwoka M, Ottaviano L, Passacantando M, Santucci S, Czempik G, Szuber J. XPS study of the surface chemistry of L-CVD SnO2 thin films after oxidation. Thin Solid Films. 2005;490(1):36–42.

75. Gao C, Jiang Z, Wang P, Jensen LR, Zhang Y, Yue Y. Optimized assembling of MOF/SnO2/Graphene leads to superior anode for lithium ion batteries. Nano Energy. 2020;74(March):104868.

76. Wu X-L, Guo Y-G, Su J, Xiong J-W, Zhang Y-L, Wan L-J. Carbon-Nanotube-Decorated Nano-LiFePO 4 @C Cathode Material with Superior High-Rate and Low-Temperature Performances for Lithium-Ion Batteries. Adv Energy Mater. 2013 Sep;3(9):1155–60.

77. Bennett TD, Tan JC, Yue Y, Baxter E, Ducati C, Terrill NJ, et al. Hybrid glasses from strong and fragile metal-organic framework liquids. Nat Commun. 2015;6:1–7.

78. Madsen RSK, Qiao A, Sen J, Hung I, Chen K, Gan Z, et al. Ultrahigh-field 67 Zn NMR reveals short-range disorder in zeolitic imidazolate framework glasses. Science. 2020 Mar 27;367(6485):1473–6.

79. Maiti S, Pramanik A, Manju U, Mahanty S. Reversible Lithium Storage in

Manganese 1,3,5-Benzenetricarboxylate Metal–Organic Framework with High Capacity and Rate Performance. ACS Appl Mater Interfaces. 2015 Aug 5;7(30):16357–63.

LIST OF PUBLICATIONS

PUBLICATIONS IN PEER-REVIEW JOURNALS

(1) **Gao C**, Wang P, Wang Z, Kær SK, Zhang Y, Yue Y. The disordering-enhanced performances of the Al-MOF/graphene composite anodes for lithium ion batteries. *Nano Energy*. 2019 Nov;65(July):104032.

(2) **Gao C**, Jiang Z, Wang P, Jensen LR, Zhang Y, Yue Y. Optimized assembling of MOF/SnO_2/Graphene leads to superior anode for lithium ion batteries. *Nano Energy*. 2020;74(March):104868.

(3) Liu W, Qin M, **Gao C**, Yu D, Yue Y. Green and low-cost synthesis of $LiNi_{0.8}Co_{0.15}Al_{0.05}O_2$ cathode material for Li-ion batteries. *Mater Lett*. 2019; 246:153–6.

(4) Zhang Y, Wang P, Li G, Fan J, **Gao C**, Wang Z, Yue Y. Clarifying the charging induced nucleation in glass anode of Li-ion batteries and its enhanced performances. *Nano Energy*. 2019;57(December 2018):592–9.

(5) Sheng Li, Ang Qiao, **Gao C**, Yanfei Zhang, Yunlong Yue, Yuanzheng Yue. Mechanical and dynamic properties of V_2O_5-TeO_2-P_2O_5 glasses. *J. Alloys Compd.* (2020), p. 158074.

ORAL AND POSTER PRESENTATIONS AT CONFERENCES

(1) **Gao C**, Wang P, Wang Z, Kær SK, Zhang Y, Yue Y. MOF-graphene composite with long order-disorder process for high-performance lithium ion batteries. **Oral**: *4th International Conference on Nanoenergy and Nanosystems 2019*, Beijing, China, 15/06/2019.

Paper I

Nano Energy 65 (2019) 104032

Contents lists available at ScienceDirect

Nano Energy

journal homepage: www.elsevier.com/locate/nanoen

Full paper

The disordering-enhanced performances of the Al-MOF/graphene composite anodes for lithium ion batteries

Chengwei Gao[a], Peixing Wang[b], Zhaoyang Wang[c], Søren Knudsen Kær[d], Yanfei Zhang[b,**], Yuanzheng Yue[a,b,c,*]

[a] Department of Chemistry and Bioscience, Aalborg University, 9220 Aalborg, Denmark
[b] School of Materials Science and Engineering, Qilu University of Technology, Jinan 250353, China
[c] State Key Laboratory of Silicate Materials for Architectures, Wuhan University of Technology, Wuhan 430070, China
[d] Department of Energy Technology, Aalborg University, 9220 Aalborg, Denmark

ARTICLE INFO

Keywords:
Lithium ion batteries
Anodes
Metal-organic frameworks
Graphene
Order-disorder transition

ABSTRACT

The metal-organic frameworks (MOFs) have gained considerable attention owing to their unique structures with tunable three-dimensional porous frameworks and numerous applications. The large surface area and great porosity make MOFs a promising electrode material for lithium-ion batteries. In this work, the focus is placed on an unexplored key issue, i.e., the impact of lithiation/delithiation on the structure of MOFs as anode materials. To do so, Al-MOF (chemical formula: $Al(OH)[O_2C–C_6H_4–CO_2]$) particles are synthesized, and then uniformly covered by graphene to form the Al-MOF/graphene composite. It is found that the lithiation/delithiation induces a pronounced structural change in the Al-MOF particles, which manifests as an order-disorder transition. This transition leads to the more open channels, thereby benefiting the diffusion and storage of Li^+ ions. Compared with pure Al-MOF, the Al-MOF/graphene composite exhibits significantly enhanced electrochemical performances. Its capacity increases continuously from 60 to 400 mAh g^{-1} at the current density of 100 mA g^{-1}. This work indicates that both the lithiation/delithiation induced order-disorder transition in MOFs and the optimized wrapping of MOF by graphene are crucial for enhancing the capacity and the cycling stability of anode materials.

1. Introduction

Metal-organic frameworks (MOFs) as a new class of porous materials, constructed by metal nodes and organic ligands, have received great attentions due to their wide applications [1–7]. In particular, because of their large surface area, tunable porous structure, redox activity, and abundant reaction sites, MOFs have been considered as a promising material for energy storage applications, e.g., lithium storage [8–11]. However, the MOFs based anodes usually exhibit poor rate capacity owing to their low conductivity and poor structural stability that inevitably limit their practical applications [9,12,13]. To overcome this problem, an effective strategy is to fabricate composites by combining MOFs with electrically conductive materials such as graphene and conductive polymer using different methods [14–16]. Recently, Lan et al. found that, as the anode for lithium ion battereis (LIBs), polyoxometalates-based metal-organic frameworks/reduced graphene nanocomposite exhibited superior electrochemical performances, e.g., a high reversible capacity of 1075 mAh g^{-1} after 100 cycles at 50 mA g^{-1} [14]. In addition, a MOF-polyaniline composite was also found to have large areal capacitance of 2146 mF cm^{-2} at 10 mV s^{-1} when it was used as electrode for supercapacitors [17]. Among these conductive matrixes for MOFs, graphene with a single-atom-thick sheet of honeycomb carbon lattice shows great potential to enhance the performance of MOFs anode since it has high electronic conductivity and large surface area for supplying anchoring sites via strong chemical interactions to MOFs [18,19].

Considering the advantages of graphene, a MOFs/graphene composite, which combined Fe-MOFs with graphene through one solvothermal step in dimethylformamide, was applied as the anode for LIBs [15]. However, its capacity decayed rapidly with an increase of current density. That is, when the current density was increased from 50 to 400 mA g^{-1}, only around 30% capacity was retained. To improve the rate capability, Hu et al. proposed a practical and effective way, i.e., increasing the metal-chelation strength between MOFs and graphene via the benzoic acid functionalized graphene, and thereby significantly enhancing the electronic conductivity of the anodes, and thus resulting

* Corresponding author. Department of Chemistry and Bioscience, Aalborg University, 9220 Aalborg, Denmark.
** Corresponding author.
E-mail addresses: zhang-yanfei@hotmail.com (Y. Zhang), yy@bio.aau.dk (Y. Yue).

https://doi.org/10.1016/j.nanoen.2019.104032
Received 23 July 2019; Received in revised form 10 August 2019; Accepted 16 August 2019
Available online 16 August 2019

in a higher reversible capacity and ameliorative rate capability [16]. Recently, another approach, namely, the disorder/order engineering, was established, and also proved to be a powerful way to improve the electrochemical performances of both anode and cathode materials in LIBs or Na^+ ion batteries [20–22]. Despite these advances, the structural degradation mechanism of MOF materials for anode has not been fully understood and the influence of structural changes on the lithium storage performance has not been reported to the best of our knowledge. Understanding these effects would be highly beneficial to designing new MOFs and other anode materials in which the structural changes could be regulated and controlled for better lithium storage and cycling stability. Driven by the above-mentioned aspects, in this work we prepared a porous Al-based MOF/graphene composite via an easy and low-cost strategy to explore the impact of the structural change of MOF during the discharging/charging process on the electrochemical performances of LIBs.

To get higher structural stability, we first choose aluminum, which is cheaper and eco-friendly, as metal centers to prepare the Al-based MOF, specifically, Aluminum 1,4-benzenedicarboxylate Al(OH)[O_2C–C_6H_4–CO_2] [23]. In this work, this type of MOF is named as Al-MOF, which is also called MIL-53 elsewhere. The Al-based MOF is synthesized under hydrothermal reaction conditions using only water as solvent, i.e., organic solvent-free. Then, a unique Al-based MOF/graphene composite is synthesized via a facile method. For this method, graphene oxide (GO) is introduced by means of the electrostatic force between the positively charged Al-MOF particles and negatively charged GO sheets. After that, GO is reduced to graphene by vitamin C. When tested as anode for LIBs, this Al-MOF/graphene composite exhibits significantly enhanced electrochemical performances and an interesting activation process during cycling, i.e., the order-disorder transition of MOF particles, compared to the graphene-free Al-MOF.

2. Experimental section

2.1. Synthesis of Al-MOF/graphene

All raw chemicals were purchased from commercial suppliers and used as received without further purification. GO was prepared by the modified Hummer's method [24]. Al-MOF was prepared with water as solvent [23]. In detail, aluminum nitrate nonahydrate (1.3 g, 3.5 mmol) and 1,4-Benzenedioic acid (0.288 g, 1.7 mmol) were added to 30 ml deionized water. The obtained solution was transferred to a 50 ml Teflon-lined high pressure autoclave. After sealing, the autoclave was kept at 220 °C for 3 days and then naturally cooled down to room temperature. The precipitation was collected by centrifugation and washed several times with de-ionized water. After being dried in a vacuum oven, 285 mg of Al-MOF powder was dispersed in a 30 ml GO aqueous solution (0.5 mg ml^{-1}). Then 60 mg Vitamin C was added and the obtained dispersion was heated to 90 °C and kept for 2 h. Finally, the black Al-MOF/graphene powder was separated by centrifugation and then dried in a vacuum oven at 120 °C for 12 h. The as-synthesized composite was denoted as AMG.

2.2. Materials characterizations

The zeta potential of all the samples were measured with Zetasizer Nano series, Malvern. Powder X-ray diffraction (XRD) measurements of the samples were performed on a PANalytical X-ray diffractometer with Cu Kα (λ = 1.5406 Å) radiation during the 2θ range of 5–60° with a step size of 0.013°. Raman spectra were obtained from Renishaw In-Via Raman microscopic with an Ar^+ laser (λ = 785 nm) at 50 × aperture. X-ray photoelectron spectroscopy (XPS) was performed by using ESCALAB 250Xi spectrometer (ThermoFisher Scientific, USA) with non-monochromatic Al Ka X-ray (1486.6 eV) at pass energy of 50 eV. Scanning electron microscopy (SEM) measurements were conducted using Zeiss Gemini SEM 500. Transmission electron microscopy (TEM) measurements were carried out using a JEM-2100F (JEOL Ltd., Japan) in scanning TEM mode. N_2 adsorption-desorption isotherms were obtained at 77 K with an ASAP 2020 Accelerated Surface Area and Porosimetry System; Brunauer-Emmett-Teller (BET) and Barrett-Joyner-Halenda (BJH) analyses were used to calculate the specific surface area, and the corresponding pore size distribution.

2.3. Electrochemical measurements

The electrochemical performance of the as-prepared Al-MOF/graphene composite as anode were evaluated by using CR2032 coin cells with lithium foil (diameter of 10.0 mm) as the counter/reference electrode. 1 M $LiPF_6$ in ethylene carbonate (EC)/diethyl carbonate (DEC)/dimethyl carbonate (DMC) (1:1:1 vol%) and a Celgard 2325 membrane (diameter of 19.0 mm) were used as the electrolyte and separator, respectively. The working electrodes were prepared by mixing 70 wt% active materials (AMG), 20 wt% acetylene black and 10 wt% polyvinylidene difluoride (PVDF) onto a copper foil substrate and dried at 110 °C in a vacuum oven for 24 h. The loading amount of active materials was 1–2 mg. The cells were assembled in an Argon-filled glovebox with both the moisture and the oxygen content below 1 ppm and then tested at 25 °C. The galvanostatic charging/discharging tests of the samples were conducted on a Land battery test system (CT2001A). Cyclic voltammetry (CV) curves in the voltage range of 0.01–3 V and EIS spectra with the frequency range of 0.1 Hz–100 kHz were obtained on a CHI 760e electrochemical workstation.

3. Results and discussion

Scheme 1 illustrates the preparation process of the Al-MOF/graphene (AMG) composite. Initially, the Al-MOF nanoparticles carry the positive charges on their exterior surfaces confirmed by the positive value zeta potential of 15.6 mV. The positive charges are denoted as the

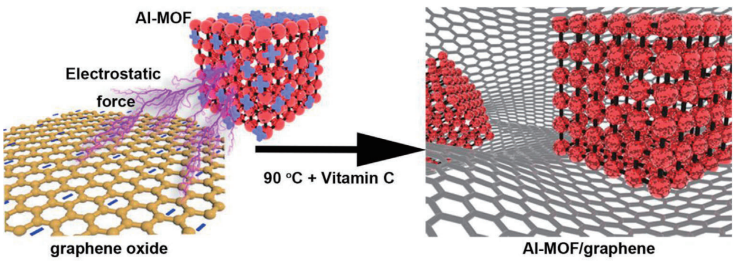

Scheme 1. Schematic representation of the preparation process of Al-MOF/graphene composite. The "+" and "-" symbols on the surface of Al-MOF and graphene oxide represent positive and negative charges, respectively.

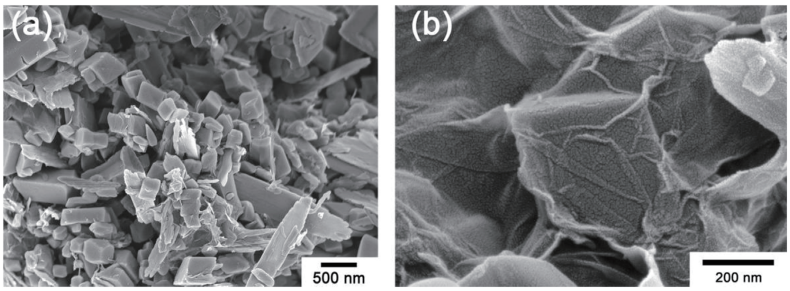

Fig. 1. SEM images of (a) Al-MOF and (b) AMG.

blue "+". The negatively charged surface of GO resulting from oxygen-contained functional groups exhibits the negative zeta potential of 44.7 mV. Due to the strong electrostatic attractive forces between the MOF and GO, the Al-MOF nanoparticles can firmly anchor on the GO surface, i.e., via a facile self-assembly process to form the Al-MOF/GO precursor. After a reduction process of GO by Vitamin C, the AMG is obtained. The mass fraction of graphene is set as 5% in order to obtain the best performance [16]. For comparison, the pristine Al-MOF was prepared by a simple hydrothermal method.

The band gaps of Al-MOF and AMG calculated from diffusion reflectance ultraviolet–visible spectra are 4.0 and 3.7 eV, respectively (Fig. S6). This decrease of band gap after the addition of graphene sheets might be a main reason for the better electronic conductivity of AMG.

The morphologies of both the Al-MOF and AMG were examined by TEM (Figs. S2 and S3) and SEM (Fig. 1a and b), respectively. The irregular Al-MOF particles with size ranges from 100 nm to several micrometers can be observed in Fig. 1a and Fig. S2. The MOF particles remain unchanged after combination with graphene. As shown in Fig. 1b and Fig. S3, the Al-MOF particles are completely covered by silk-like graphene sheets, confirming the assembly of these two components.

Fig. 2a presents the XRD patterns of the as-synthesized AMG, Al-MOF and simulated Al-MOF, respectively. It can be seen that the diffraction peaks at 8.9°, 10.3°, 15.1°, 17.9° and 20.5° of both the Al-MOF and AMG coincide well with those in the simulated pattern based on Al-MOF single-crystal [23]. This result indicates that Al-MOF preserves its ordered structure after the addition of graphene and the reduction process, implying its high structural stability. Except for those diffraction peaks assigned to Al-MOF single-crystal, the residual diffraction peaks detected in the XRD pattern arise from two other crystals forms with different guest molecules trapped in the pores of the MOF and AlO(OH) formed during the synthesis process [23,25]. Raman spectra of AMG, GO and graphene shown in Fig. 2b exhibit two obvious vibration peaks at around 1350 cm^{-1} (D-band) and 1590 cm^{-1} (G-band), respectively, which could be assigned to the E_{2g} phonon of C sp^2 atoms and the breathing mode of κ-point phonons of A_{1g} symmetry [26]. The peak intensity ratio (I_D/I_G) is usually used to measure the degree of lattice distortion of graphene sheets. The AMG exhibits the largest I_D/I_G (1.12) than rGO and GO (1.07 and 1.01), suggesting that more defects are introduced into graphene sheets after attaching to MOF particles.

To determine the surface composition of AMG, X-ray photoelectron spectroscopy (XPS) was conducted. The XPS survey spectra of AMG distinctly show three elements: aluminum (Al 2p), carbon (C 1s) and oxygen (O 1s) (Fig. 3a). As shown in Fig. 3b, the peak of Al 2p appears at 73.58 eV, which demonstrates the existence of Al^{3+} in the composite. The C 1s spectrum in Fig. 3c shows two obvious peaks at 284.7 eV and 288.9 eV. These two peaks could be fit to peaks at 284.6, 285.9, 287.3 and 288.8 eV and thus be assigned to C–C, C–O, C═O and O═C–O species, respectively [27]. The distinct peak of O═C–O species and the O 1s peak (Fig. 3d) located at 531.68 eV could be ascribed to the organic ligand of MOF, while the weak peaks of C–O and C═O species might result from the residue functional groups of graphene.

To characterize the electrochemical properties of both the Al-MOF and AMG anodes, the cyclic voltammetry curves of Al-MOF and AMG were recorded in the voltage range between 0.01 and 3 V at a scanning rate of 0.1 mV s^{-1}. For the Al-MOF electrode (Fig. 4a), two main

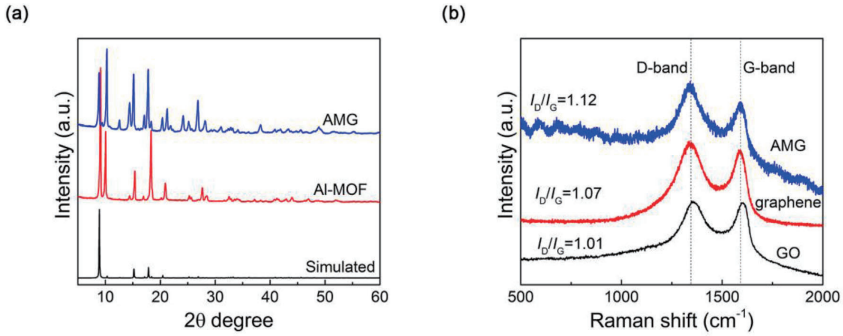

Fig. 2. (a) XRD patterns of the as-synthesized AMG, Al-MOF and the simulated pattern obtained from Al-MOF single-crystal data. (b) Raman spectra of AMG, GO and graphene.

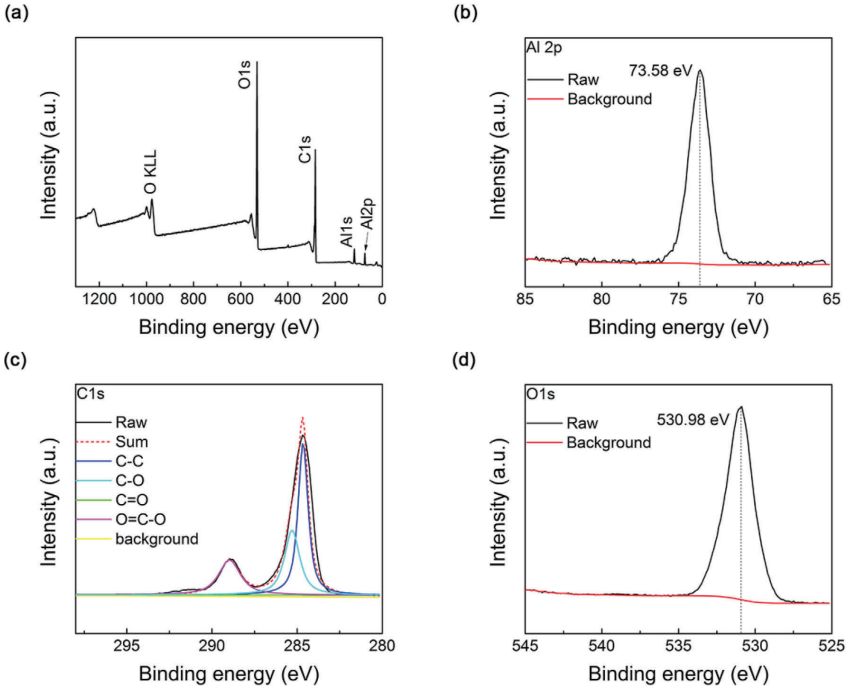

Fig. 3. (a) XPS survey spectrum of AMG. High-resolution spectra for (b) Al 2p, (c) C 1s and (d) O 1s.

reduction peaks are observed at 0.68 V and 0.82 V during the first cathodic downscan, which could be attributed to the formation of solid-electrolyte interface (SEI) film and some irreversible side reactions, respectively, upon the insertion of Li^+ ions [28]. In the subsequent two cathodic downscans, the two reduction peaks merged into one main peak and shifted to 0.84 V, representing the reversible lithiation process of the Al-MOF [29]. The three anodic upscan curves overlap well with each other and exhibit two oxidation peaks at about 0.1 V and 0.9 V, which correspond to two different lithium extraction processes from the Al-MOF. For the AMG electrode (Fig. 3b), both the cathodic and anodic curves in the three cycles are resemble to those of the Al-MOF, implying a similar lithium insertion/extraction mechanism to that of the Al-MOF. Thus, we propose a possible lithium intercalation/deintercalation mechanism of AMG as follows [29,30]:

$$Al(OH)[O_2C–C_6H_4–CO_2] + xLi^+ + e^- \leftrightarrow Al(OH)[O_2C–C_6H_4–CO_2Li_x] \quad (1)$$

As shown in Scheme 2, the MOF should possess an insertion type lithium storage mechanism, during which Li^+ ions might diffuse into or from MOF and interact with aromatic rings and carboxyl groups from organic ligands without disturbing the metal nodes. The observed cathodic and anodic peaks from CV curves could be related to the lithium insertion/extraction processes. However, further investigation should be done to confirm the detailed Li^+ ions insertion/extraction mechanism.

Fig. 4c and d presents the initial three and 100th charge-discharge profiles of the Al-MOF and AMG, respectively, at a current density of 100 mA g^{-1} in the voltage range of 0.01–3 V. The first discharge profile of Al-MOF exhibits a clear discharge plateau at about 0.7 V (Fig. 4c), which might be attributed to the formation of SEI layer. In the next two charge-discharge profiles, a discharge plateau at 0.8 V and a charge plateau at 0.9 V that originate from the Li^+ intercalation and deintercalation could be observed, coinciding well with the couple of redox peaks in the CV curves. In the 100th profile, both the charge and discharge plateau disappear, which might result from the poor structural stability, i.e., partial collapse, of Al-MOF. The initial discharge/charge capacities of Al-MOF are 381/131 mAh g^{-1}, resulting in an initial columbic efficiency of 34%. In addition, the discharge/charge capacities of the second, third and 100th cycles decrease to 159/128, 148/128 and 59/58 mAh g^{-1}, respectively, demonstrating a poor reversibility of the Al-MOF. In contrast, the AMG anode exhibits a quite different scenario. In detail, as presented in Fig. 4d, the initial three discharge/charge capacities of the AMG anode are 481/158, 263/178 and 283/207 mAh g^{-1}, respectively, which are much larger than those of the Al-MOF. Particularly, it delivers a much larger discharge/charge capacity (409/403 mAh g^{-1}) after 100 cycles, compared with the initial three cycles, and gives a significantly higher columbic efficiency of 99%. This implies that the microstructure of the AMG was further electrochemically activated by the subsequent long cycles.

Fig. 5a shows both the cyclic performance and the Coulombic efficiency of Al-MOF and AMG at the current density of 100 mA g^{-1}. All the specific capacities are calculated based on the mass of active materials. The first discharge capacity of Al-MOF is 381 mAh g^{-1} with an initial Coulombic efficiency of 34%. This large capacity loss is attributed to the formation of SEI layer and other irreversible reactions. After a slight decrease during the first several cycles, Al-MOF presents a stable capacity of 60 mAh g^{-1} and a Coulombic efficiency about 97% up to 100 cycles. Notably, the AMG anode exhibits a significantly enhanced capacity compared with the pristine Al-MOF. The obvious

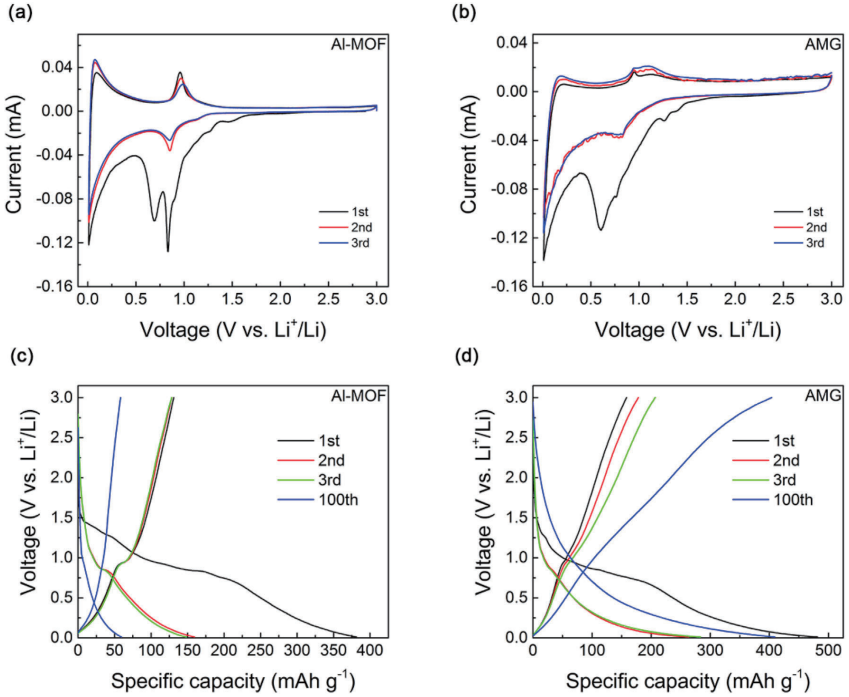

Fig. 4. Typical cyclic voltammetry curves of the initial 3 cycles for (a) Al-MOF and (b) AMG between 0.01 and 3 V at a scanning rate of 0.1 mV s^{-1}. Charge-discharge profiles of the initial 3 and the 100th cycles for the (c) Al-MOF and (d) AMG at a current density of 100 mA g^{-1}.

irreversible capacity loss in the first 20 cycles should be mainly attributed to the SEI layer and other subsequent irreversible reactions resulting from the introduction of graphene sheets. This drawback should be overcome in future to make this composite anode suitable for practical applications. To do so, some potential approaches could be used, e.g., pre-lithiation and replacement of solid electrolytes for liquid ones. After this capacity loss upon initial cycles, AMG shows a huge jump in capacity from 263 to 403 mAh g^{-1} after 100 cycles, which is

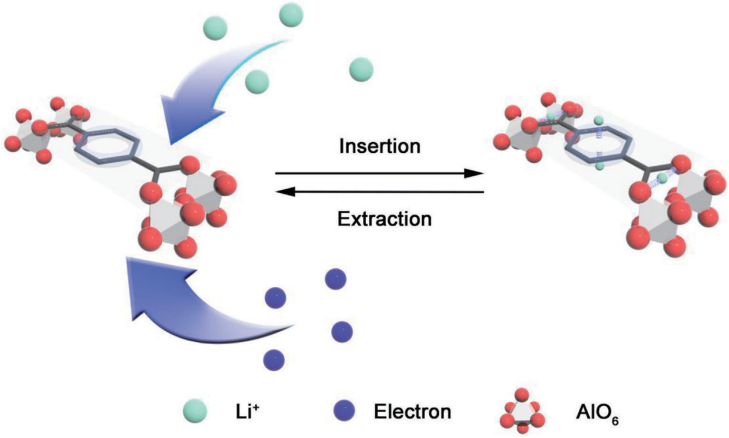

Scheme 2. Proposed Li^+ ions insertion-extraction process into or from Al-MOF.

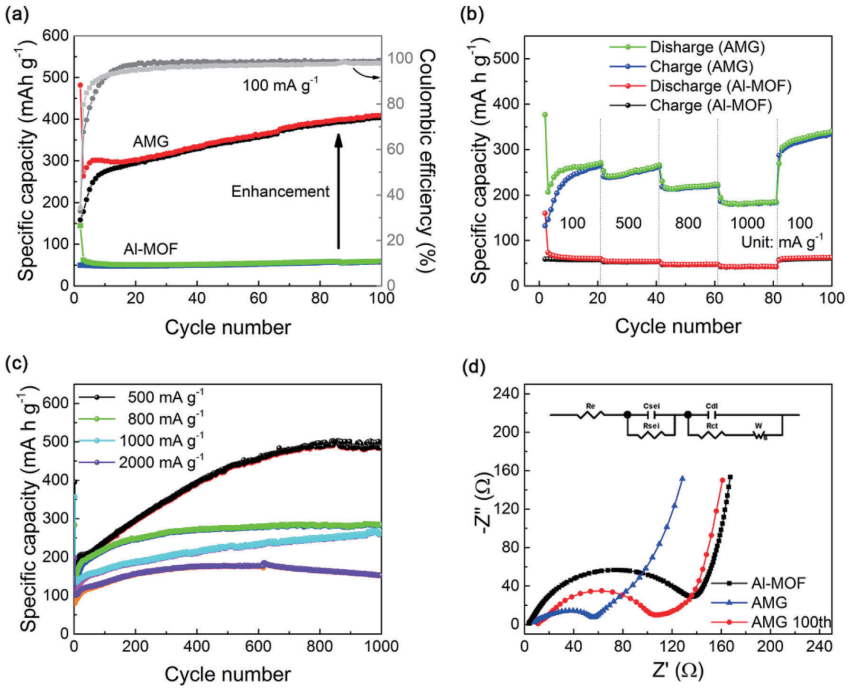

Fig. 5. (a) Cycling performance and coulombic efficiency of Al-MOF and AMG at a current density of 100 mA g^{-1}. (b) The rate capability of Al-MOF and AMG. (c) Cycling performance of AMG at different current densities. (d) Nyquist plots of Al-MOF, AMG and AMG after 100 discharging/charging cycles at 100 mA g^{-1} (Inset is the equivalent circuit).

more than 6 times higher than that of Al-MOF. This remarkable improvement in the capacity of the AMG is reported for the first time concerning MOFs-based anode materials. This could be attributed to the following advantages of the unique structures of the AMG by addition of graphene sheets, which synergistically enhance the electronic conductivity and ion diffusion kinetics. First, the graphene-covered MOF with mesoporous structure provides high specific surface area and fast Li^+ ions transport. That is, the activation process of MOF particles is facilitated by covering them with graphene, enabling more Li^+ ions diffuse into the internal pores of the MOF due to large isostatic attraction zone between Li^+ ions and carbon, where there are more reaction sites for lithium storage. Second, in addition to facilitating the electron transport, the robust network structure of the graphene can buffer the strain/stress and keep MOF structure stable during cycling. The exact mechanism for such an improvement in electrochemical performance of AMG still need to be further explored. The rate performance of the AMG anode is compared with that of Al-MOF anodes in Fig. 5b. Upon being cycled at 100, 500, 800 and 1000 mA g^{-1}, the AMG displays the average capacities of 260, 250, 220 and 180 mAh g^{-1}. The capacity can still maintain at 326 mAh g^{-1} even when the current decreases to 100 mA g^{-1}, indicating the outstanding rate stability. More strikingly, the capacity exhibits a similar increase trend under different current densities to that under a constant current density. This capacity increase not only suggests the excellent rate capability and cyclic stability of AMG, but also confirms that the charge-discharge rate tests have same effect on the structure of MOF as that of galvanostatic charge-discharge experiment. On the contrary, the Al-MOF merely shows 55, 53, 47 and 42 mAh g^{-1} under the same conditions.

The cycling performances of AMG are exhibited in Fig. 5c. In the long-term galvanostatic charge-discharge tests at different current densities, AMG maintains impressive capacity of 484, 284, 267, and 153 mAh g^{-1} after 1000 cycles at 500, 800, 1000 and 2000 mA g^{-1}, respectively. It is worth mentioning that the AMG exhibits a capacity increase trend with continuous cycling up to 1000 cycles at current densities lower than 1000 mA g^{-1}. To the best of our knowledge, this trend has not been reported for MOFs-based materials so far. This striking phenomenon could be explained by the gradual activation process, during which more and more internal pores and surface of Al-MOF become accessible for electrolyte and Li^+ ions with the help of graphene sheets. However, at the higher current density of 2000 mA g^{-1}, the charge-discharge curve exhibits a bump with a maximum value of 178 mAh g^{-1} at around 500 cycles, after which the AMG shows a slightly declining trend. This capacity fading might be related to the structural degradation at this high current density.

The electrochemical impendence spectra (EIS) of Al-MOF, AMG and AMG after 100 cycles are shown in Fig. 5d. Each EIS spectrum exhibits one semicircle from the high to middle frequency region and one inclined line in low frequency range. As the equivalent circuit shows, the intercept at far-left end is ascribed to the resistance (R_e) of the bulk electrode, electrolyte and the separator. The semicircle is relative to the SEI resistance (R_{sei} and C_{sei}) and charge transfer resistance (R_{ct} and C_{dl}). The line inclined at approximately 45° at the low frequency corresponds to the Warburg impedance (W), which is associated with the diffusion effects of Li^+ ions at the interface between the active material particles and electrolyte. It is obvious that the diameter of the semicircle of the AMG is much smaller than that of the Al-MOF. When the AMG anode

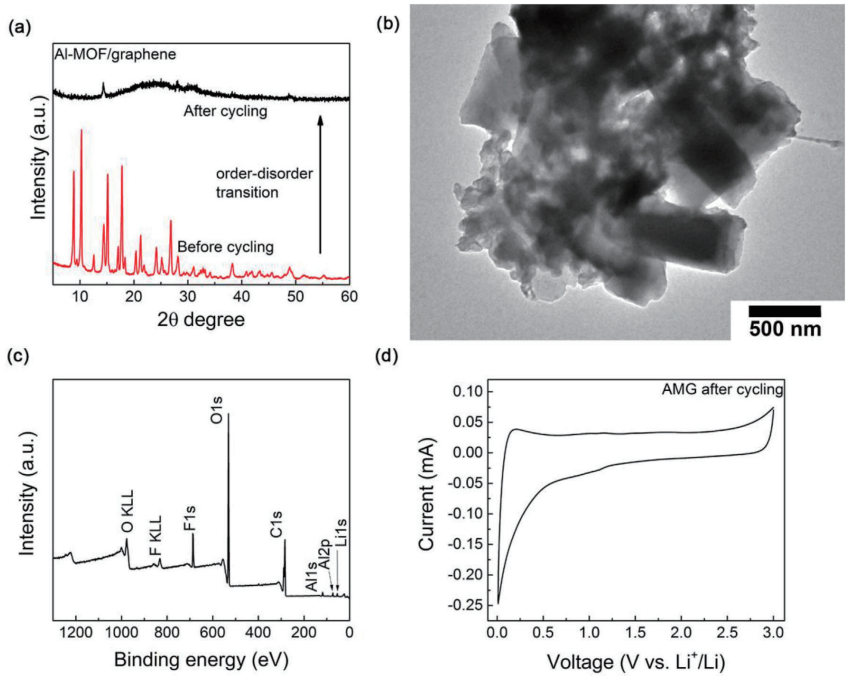

Fig. 6. (a) XRD patterns of AMG and AMG after 100 discharging/charging cycles. (b) Ex-situ TEM image, (c) Ex-situ XPS spectrum and (d) Cyclic voltammetry curve of AMG after 100 discharging/charging cycles.

undergoes 100 cycles of discharging/charging, its diameter of the semicircle increases, but is still smaller than that of the Al-MOF. This suggests that the AMG possesses enhanced Li^+ ions migration kinetics through SEI layer and faster charge transfer reactions compared to Al-MOF because of the addition of graphene sheets. However, the enhanced kinetics of AMG is gradually undermined with increasing the number of the cycles, and this might be assigned to continuous growth of the SEI film or side reactions.

To clarify the origin of the excellent electrochemical performance of AMG, we performed the XRD measurements on both AMG and AMG after 100 charge-discharge cycles. As shown in Fig. 6a, there are pronounced diffraction peaks for the as-prepared AMG before cycling. After 100 cycles, most of the diffraction peaks of AMG disappear, implying that Al-MOF is amorphized by discharging/charging cycles, i.e., the order-disorder transition occurs, and finally the long-range order vanishes. The possible scenario of the order-disorder transition could be as follows. It is known that the Al-MOF contains a large amount of voids, and ligand walls between the neiboughring voids. It is also known that the coordinative bonds between the central atom (e.g. Al in our case) and organic ligand are much weaker than the covalent bonds of the ligand molecules. Considering these two factors, the lithium ions might impact the coordinative bonds, and thereby cause the rotation, libration, and migration of some ligands, and the breakage of Al–O–Al chains. In other words, both rotational and translational disordering take place during lithiation/delithiation, and consequently more or larger channels are generated. As the discharging/charging cycling proceeds, the amount of channels continuously increases and thus the degree of long-range order in Al-MOF decreases (Fig. 6a). This will lead to a gradual enhancement of the lithium diffussion and storage as evidenced by the rising curve of the specific capacity with increasing the cycling number (Fig. 5a).

Fig. 6b shows the TEM image of the AMG anode after 100 cycles at 100 mA g^{-1}. Even after a long-term cycling process, e.g., 100 cycles, the morphology of the Al-MOF particles remains unchanged, indicating that the graphene coat protects the Al-MOF particles from collapsing. In other words, The Al-MOF particles are still anchored on the graphene and the overall structural integrity is well conserved, ensuring a high structural stability of AMG against lithium intercalation/deintercalation. As shown in Fig. 6c, the survey XPS spectrum indicates the presence of Li, F, Al, C and O in the AMG subjected to 100 cycles. It is inferred that the Li and F appear in the SEI film since a minor amount of the electrolyte could decompose. By comparing the XPS results in Fig. 6c and Fig. S8 with those of as-prepared AMG prior to cycling (Fig. 3a), it is found that there is no obvious change in valence states of Al, O and C in AMG upon 100 cycles, implying that the discharging/charging process does not change the electronic structures of the AMG surface. The CV curve after 100 cycles (Fig. 6d) shows redox peaks at around 0.1 and 1 V, which are almost same as those shown in Fig. 4b, suggesting that the lithium ion intercalation/deintercalation mechanism remains unchanged. In this context, the continuing electrochemical activation process of AMG could be ascribed to the order-disorder transition in MOF induced by discharging/charging, while the particle morphology remains unaffected. The TEM image confirms that the MOF particles is intact with graphene sheets after cycling, while the XPS results prove that the valence states of AMG have not changed upon cycling. Consequently, the AMG particles can be kept in better contact with the electric current collector. Via order-disorder transition, more channels and reactions are generated in Al-MOF, enhancing Li^+

ions imigration and storage. Thus, the interior part of bulk MOF becomes accessible for lithium ions, resulting in the great enhancement of capacity.

4. Conclusion

A high electrochemical performance Al-MOF/graphene composite was synthesized using a facile, eco-friendly and low-cost method. Through a self-assembly process, Al-MOF was uniformly anchored on graphene sheets. The Al-MOF/graphene composite showed a drastic increase in specific capacity from 60 to 400 mAh g^{-1} at the current density of 100 mA g^{-1} with increasing the discharging/charging cycles. This remarkable enhancement could be ascribed to the structural disordering in MOF crystals caused by lithiation/delithiation, since disordering causes more channels for Li^+ ions migratiton and storage. The MOF paticles remain electronically conductive with the current collector via graphene sheets. These sheets increase the electronic conductivity, and simultaneously enhance both the Li^+ ions migration kinetics through the SEI layer and the charge transfer reactions. The order-disorder transition in MOF during lithiation/delithiation cycles is a promising way to increase the cycling stability of MOF-containing anode materials.

Acknowledgements

This work was financially supported by China Scholarship Council (201707040085), National Natural Science Foundation of China (51402156) and Shandong Provincial Natural Science Foundation (ZR2014EMQ003, ZR2018QB003). We would like to thank Prof. H.Z. Tao and Prof. L.R. Jensen for their help with XPS and Raman tests, respectively.

Appendix A. Supplementary data

Supplementary data to this article can be found online at https://doi.org/10.1016/j.nanoen.2019.104032.

References

[1] K.S. Park, Z. Ni, A.P. Cote, J.Y. Choi, R. Huang, F.J. Uribe-Romo, H.K. Chae, M. O'Keeffe, O.M. Yaghi, Exceptional chemical and thermal stability of zeolitic imidazolate frameworks, Proc. Natl. Acad. Sci. U.S.A. 103 (2006) 10186–10191, https://doi.org/10.1073/pnas.0602439103.

[2] O.M. Yaghi, H. Li, Hydrothermal synthesis of a metal-organic framework containing large rectangular channels, J. Am. Chem. Soc. 117 (1995) 10401–10402, https://doi.org/10.1021/ja00146a033.

[3] J.R. Li, R.J. Kuppler, H.C. Zhou, Selective gas adsorption and separation in metal-organic frameworks, Chem. Soc. Rev. 38 (2009) 1477–1504, https://doi.org/10.1039/b802426j.

[4] P. Horcajada, T. Chalati, C. Serre, B. Gillet, C. Sebrie, T. Baati, J.F. Eubank, D. Heurtaux, P. Clayette, C. Kreuz, J.S. Chang, Y.K. Hwang, V. Marsaud, P.N. Bories, L. Cynober, S. Gil, G. Férey, P. Couvreur, R. Gref, Porous metal-organic-framework nanoscale carriers as a potential platform for drug deliveryand imaging, Nat. Mater. 9 (2010) 172–178, https://doi.org/10.1038/nmat2608.

[5] J. Lee, O.K. Farha, J. Roberts, K.A. Scheidt, S.T. Nguyen, J.T. Hupp, Metal-organic framework materials as catalysts, Chem. Soc. Rev. 38 (2009) 1450–1459, https://doi.org/10.1039/b807080f.

[6] Y. Zhao, Z. Song, X. Li, Q. Sun, N. Cheng, S. Lawes, X. Sun, Metal organic frameworks for energy storage and conversion, Energy Storage Mater 2 (2016) 35–62, https://doi.org/10.1016/j.ensm.2015.11.005.

[7] X. Wang, L. Chai, J. Ding, L. Zhong, Y. Du, T. Li, Y. Hu, J. Qian, S. Huang, Chemical and morphological transformation of MOF-derived bimetallic phosphide for e ffi cient oxygen evolution, Nano Energy 62 (2019) 745–753, https://doi.org/10.1016/j.nanoen.2019.06.002.

[8] A.V. Vinogradov, H. Zaake-Hertling, E. Hey-Hawkins, A.V. Agafonov, G.A. Seisenbaeva, V.G. Kessler, V.V. Vinogradov, The first depleted heterojunction TiO2-MOF-based solar cell, Chem. Commun. 50 (2014) 10210–10213, https://doi.org/10.1039/c4cc01978d.

[9] S. Zheng, X. Li, B. Yan, Q. Hu, Y. Xu, X. Xiao, H. Xue, H. Pang, Transition-metal (Fe, Co, Ni) based metal-organic frameworks for electrochemical energy storage, Adv. Energy Mater. 7 (2017) 1–27, https://doi.org/10.1002/aenm.201602733.

[10] G. Férey, F. Millange, M. Morcrette, C. Serre, M.L. Doublet, J.M. Grenèche, J.M. Tarascon, Mixed-valence Li/Fe-based metal-organic frameworks with both reversible redox and sorption properties, Angew. Chem. Int. Ed. 46 (2007) 3259–3263, https://doi.org/10.1002/anie.200605163.

[11] M. Jahan, Q. Bao, K.P. Loh, Electrocatalytically active graphene-porphyrin MOF composite for oxygen reduction reaction, J. Am. Chem. Soc. 134 (2012) 6707–6713, https://doi.org/10.1021/ja211433h.

[12] S. Maiti, A. Pramanik, U. Manju, S. Mahanty, Reversible lithium storage in manganese 1,3,5-benzenetricarboxylate metal–organic framework with high capacity and rate performance, ACS Appl. Mater. Interfaces 7 (2015) 16357–16363, https://doi.org/10.1021/acsami.5b03414.

[13] H. Zhang, W. Zhao, M. Zou, Y. Wang, Y. Chen, L. Xu, H. Wu, A. Cao, 3D, mutually embedded MOF@carbon nanotube hybrid networks for high-performance lithium-sulfur batteries, Adv. Energy Mater. 8 (2018) 1–11, https://doi.org/10.1002/aenm.201800013.

[14] T. Wei, M. Zhang, P. Wu, Y.J. Tang, S.L. Li, F.C. Shen, X.L. Wang, X.P. Zhou, Y.Q. Lan, POM-based metal-organic framework/reduced graphene oxide nanocomposites with hybrid behavior of battery-supercapacitor for superior lithium storage, Nano Energy 34 (2017) 205–214, https://doi.org/10.1016/j.nanoen.2017.02.028.

[15] Y. Jin, C. Zhao, Z. Sun, Y. Lin, L. Chen, D. Wang, C. Shen, Facile synthesis of Fe-MOF/RGO and its application as a high performance anode in lithium-ion batteries, RSC Adv. 6 (2016) 30763–30768, https://doi.org/10.1039/C6RA01645F.

[16] C. Li, X. Lou, Q. Yang, Y. Zou, B. Hu, Remarkable improvement in the lithium storage property of Co2(OH)2BDC MOF by covalent stitching to graphene and the redox chemistry boosted by delocalized electron spins, Chem. Eng. J. 326 (2017) 1000–1008, https://doi.org/10.1016/j.cej.2017.06.048.

[17] L. Wang, X. Feng, L. Ren, Q. Piao, J. Zhong, Y. Wang, H. Li, Y. Chen, B. Wang, Flexible solid-state supercapacitor based on a metal-organic framework interwoven by electrochemically-deposited PANI, J. Am. Chem. Soc. 137 (2015) 4920–4923, https://doi.org/10.1021/jacs.5b01613.

[18] K.S. Novoselov, A.K. Geim, S.V. Morozov, D. Jiang, Y. Zhang, S.V. Dubonos, I.V. Grigorieva, A.A. Firsov, Electric field in atomically thin carbon films, Science 306 (2004) 666–669, https://doi.org/10.1126/science.1102896.

[19] C. Petit, T.J. Bandosz, MOF-graphite oxide composites: combining the uniqueness of graphene layers and metal-organic frameworks, Adv. Mater. 21 (2009) 4753–4757, https://doi.org/10.1002/adma.200901581.

[20] Y. Zhang, P. Wang, T. Zheng, D. Li, G. Li, Y. Yue, Enhancing Li-ion battery anode performances via disorder/order engineering, Nano Energy 49 (2018) 596–602, https://doi.org/10.1016/j.nanoen.2018.05.018.

[21] Y. Zhang, P. Wang, G. Li, J. Fan, C. Gao, Z. Wang, Y. Yue, Clarifying the charging induced nucleation in glass anode of Li-ion batteries and its enhanced performances, Nano Energy 57 (2019) 592–599, https://doi.org/10.1016/j.nanoen.2018.12.088.

[22] F. Xiong, Q. An, L. Xia, Y. Zhao, L. Mai, H. Tao, Y. Yue, Revealing the atomistic origin of the disorder-enhanced Na-storage performance in NaFePO 4 battery cathode, Nano Energy 57 (2019) 608–615, https://doi.org/10.1016/j.nanoen.2018.12.087.

[23] T. Loiseau, C. Serre, C. Huguenard, G. Fink, F. Taulelle, M. Henry, T. Bataille, G. Férey, A rationale for the large breathing of the porous aluminum terephthalate (MIL-53) upon hydration, Chem. Eur J. 10 (2004) 1373–1382, https://doi.org/10.1002/chem.200305413.

[24] W.S. Hummers, R.E. Offeman, Preparation of graphitic oxide, J. Am. Chem. Soc. 80 (1958) 1339, https://doi.org/10.1021/ja01539a017.

[25] I. Bezverkhyy, G. Ortiz, G. Chaplais, C. Marichal, G. Weber, J.P. Bellat, MIL-53(Al) under reflux in water: formation of γ-AlO(OH) shell and H2BDC molecules intercalated into the pores, Microporous Mesoporous Mater. 183 (2014) 156–161, https://doi.org/10.1016/j.micromeso.2013.09.015.

[26] A.C. Ferrari, J.C. Meyer, V. Scardaci, C. Casiraghi, M. Lazzeri, F. Mauri, S. Piscanec, D. Jiang, K.S. Novoselov, S. Roth, A.K. Geim, Raman spectrum of graphene and graphene layers, Phys. Rev. Lett. 97 (2006) 187401, https://doi.org/10.1103/PhysRevLett.97.187401.

[27] D. Yang, A. Velamakanni, G. Bozoklu, S. Park, M. Stoller, R.D. Piner, S. Stankovich, I. Jung, D.A. Field, C.A. Ventrice, R.S. Ruoff, Chemical analysis of graphene oxide films after heat and chemical treatments by X-ray photoelectron and Micro-Raman spectroscopy, Carbon N. Y. 47 (2009) 145–152, https://doi.org/10.1016/j.carbon.2008.09.045.

[28] S. Zhang, M.S. Ding, K. Xu, J. Allen, T.R. Jow, Understanding solid electrolyte interface film formation on graphite electrodes, Electrochem. Solid State Lett. 4 (2001) A206, https://doi.org/10.1149/1.1414946.

[29] H. Chen, M. Armand, G. Demailly, F. Dolhem, P. Poizot, J.M. Tarascon, From biomass to a renewable LiXC6O6organic electrode for sustainable li-ion batteries, ChemSusChem 1 (2008) 348–355, https://doi.org/10.1002/cssc.200700161.

[30] M. Armand, S. Grugeon, H. Vezin, S. Laruelle, P. Ribière, P. Poizot, J.M. Tarascon, Conjugated dicarboxylate anodes for Li-ion batteries, Nat. Mater. 8 (2009) 120–125, https://doi.org/10.1038/nmat2372.

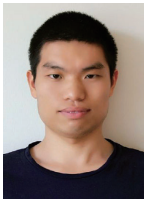

Chengwei Gao is a PhD student in Department of Chemistry and Bioscience at Aalborg University. He received his B.S. and M.S. degrees from Zhengzhou University in 2015 and 2017, respectively. His research interests mainly focus on Li/Na ion batteries.

Peixing Wang is a M.Sc. degree student in Materials Science at Qilu University of Technology. He received his B.S. degree in 2017 from the same university. His research interests focus on oxide glass anodes for lithium-ion batteries.

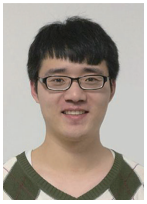

Zhaoyang Wang is a PhD student at Wuhan University of Technology. He received his B.S. and M.S. degrees from Qilu university of Technology in 2014 and 2017, respectively. His research interests mainly focus on full glass-ceramic Li/Na ion batteries.

Søren Knudsen Kær is a Professor at Aalborg University, Denmark. He obtained a M.Sc. degree in mechanical engineering from Aalborg University, Denmark in 1996 and a Ph.D. degree from the same university in 2001. He is the deputy director of the Hydrogen and Fuel Cell Academy, HyFC. His main research areas are computational fluid dynamics modelling of fuel cells and reformer reactors as well as thermodynamic modelling of fuel cell systems.

Yanfei Zhang is an Associate Professor at the Qilu University of Technology, Jinan, China. She received her Ph.D. degree in Physics from Shandong University, China, in 2009. From 2011 to 2012, she worked as a Postdoctoral fellow at Aalborg University, Denmark. Her research focuses on glass relaxation, glass transition, structure and properties of oxide glasses and glass fibers, and glass electrode materials for lithium-ion batteries.

Yuanzheng Yue is a Professor at Aalborg University (AAU), Denmark, and a distinguished visiting professor at Qilu University of Technology, China. He received his Ph.D. degree from Technische Universität Berlin, Germany, in 1995. His research deals with glasses, glass fibres, insulation materials, and amorphous materials for energy storage devices. He is a council member of the International Commission on Glass (ICG), and the founding chair of the ICG Technical Committee for Glass Fibers, and a member of the European Academy of Sciences.

Supporting Information

The disordering-enhanced performances of the Al-MOF/graphene composite anodes for lithium ion batteries

Chengwei Gao[a], Peixing Wang[b], Zhaoyang Wang[c], Søren Knudsen Kær[d], Yanfei Zhang[b,*], Yuanzheng Yue[a,b,c*]

[a]Department of Chemistry and Bioscience, Aalborg University, 9220 Aalborg, Denmark

[b]School of Materials Science and Engineering, Qilu University of Technology (Shandong Academy of Sciences), Jinan 250353, China

[c]State Key Laboratory of Silicate Materials for Architectures, Wuhan University of Technology, Wuhan 430070, China

[d]Department of Energy Technology, Aalborg University, 9220 Aalborg

*Corresponding authors: yy@bio.aau.dk (Y.Z.Y.); zhang-yanfei@hotmail.com (Y.F.Z)

Table of contents

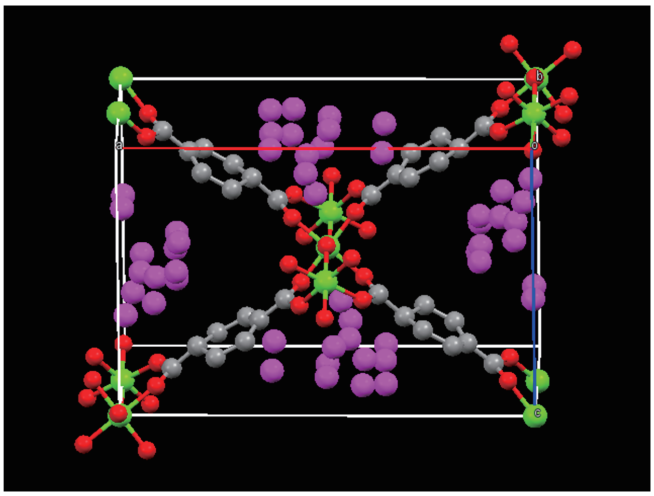

Figure S1. Crystal structure of Al-MOF of Al-MOF. Green ball: Al; red ball: O; grey ball: C; pink ball: guest molecules. Hydrogen atoms are omitted for clarity.

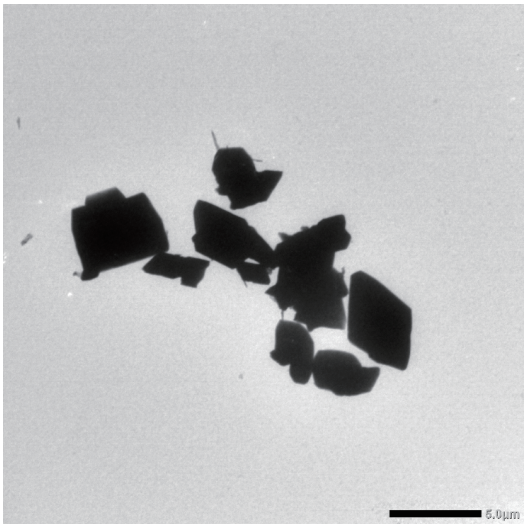

Figure S2. TEM image of Al-MOF.

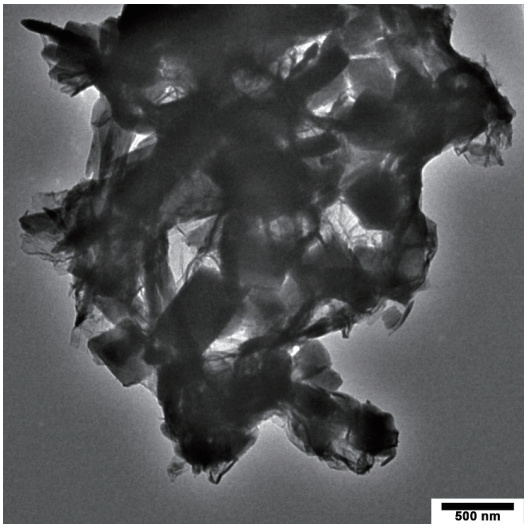

Figure S3. TEM image of AMG.

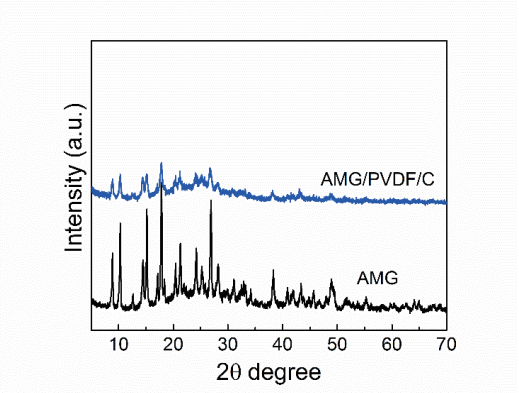

Figure S4. XRD pattern of the mixture of AMG, carbon black and PVDF

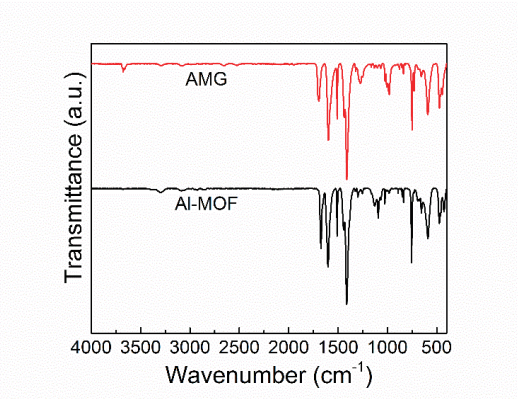

Figure S5. FT-IR spectra of AMG and Al-MOF.

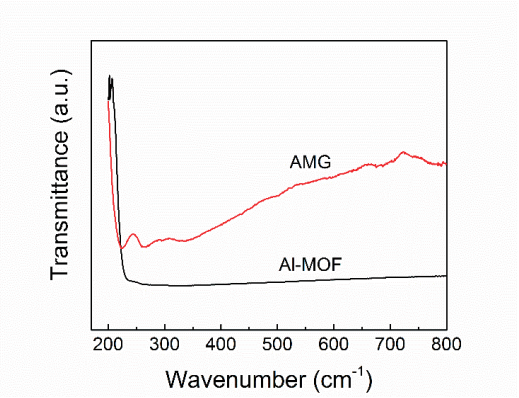

Figure S6. UV-vis spectra of AMG and Al-MOF.

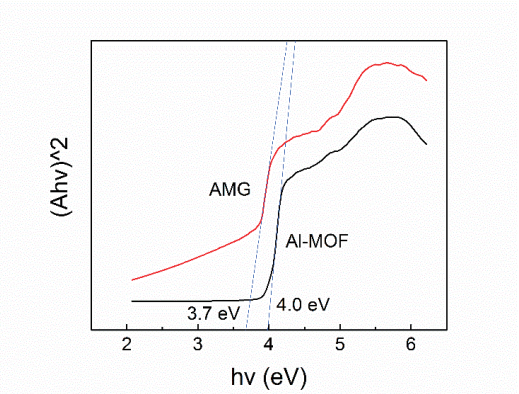

Figure S7. Tauc plots derived from Diffuse Reflectance UV-vis spectra of AMG and Al-MOF.

The optical absorption near the band edge follows the equation $\alpha hv = A(hv - Eg)^{n/2}$, where α, v, Eg, and A are the absorption coefficient, light frequency, band gap energy, and a constant, respectively. The value of n is 4 for the direct transition[1].

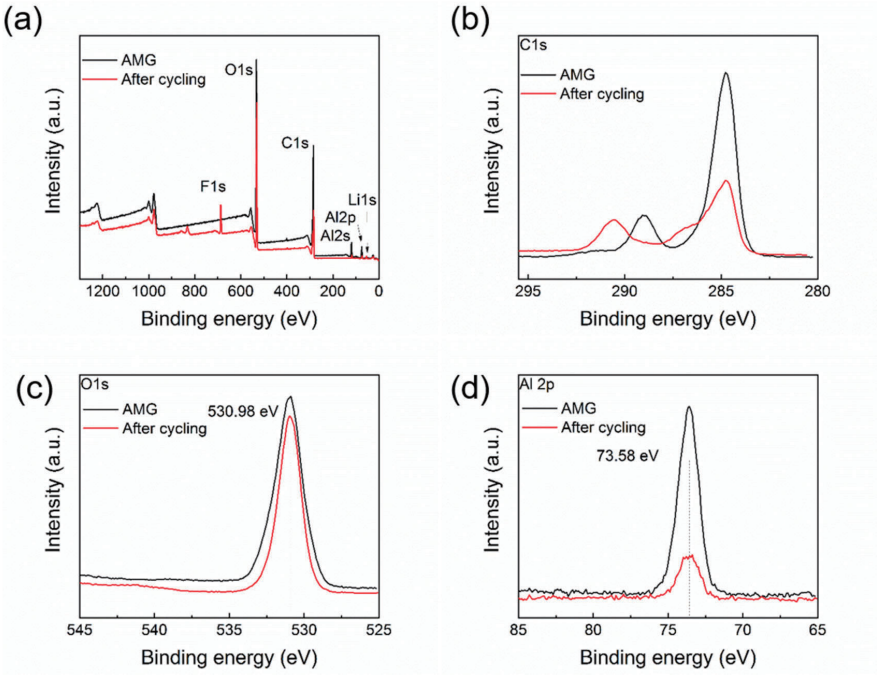

Figure S8. XPS survey spectra (a) and high-resolution spectra of O 1s (b), C 1s (c), Al 2p (d) of pristine AMG and AMG after cycling.

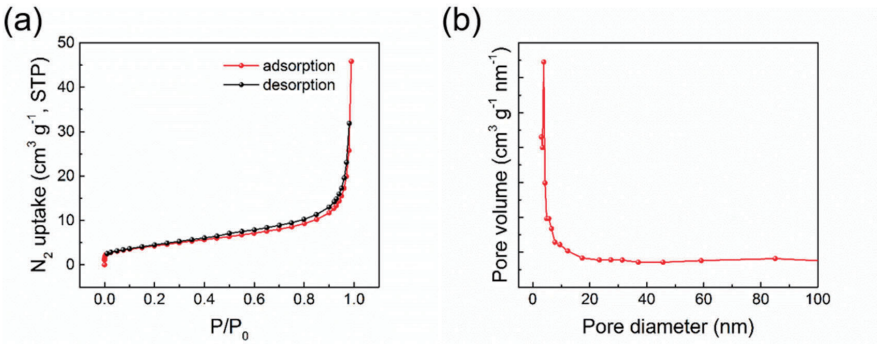

Figure S9. Nitrogen adsorption desorption isotherm (a) and pore width distribution (b) of AMG.

Reference

[1] S. Ling, B. Slater, Unusually Large Band Gap Changes in Breathing Metal-Organic Framework Materials, J. Phys. Chem. C. 119 (2015) 16667–16677. doi:10.1021/acs.jpcc.5b04050.

Paper II

Nano Energy 74 (2020) 104868

Contents lists available at ScienceDirect

Nano Energy

journal homepage: http://www.elsevier.com/locate/nanoen

Optimized assembling of MOF/SnO_2/Graphene leads to superior anode for lithium ion batteries

Chengwei Gao [a,b], Zhenjing Jiang [a], Peixing Wang [a], Lars Rosgaard Jensen [c], Yanfei Zhang [a,**], Yuanzheng Yue [a,b,d,*]

[a] School of Materials Science and Engineering, Qilu University of Technology (Shandong Academy of Sciences), Jinan, 250353, China
[b] Department of Chemistry and Bioscience, Aalborg University, 9220, Aalborg, Denmark
[c] Department of Materials and Production, Aalborg University, 9220, Aalborg, Denmark
[d] State Key Laboratory of Silicate Materials for Architectures, Wuhan University of Technology, Wuhan, 430070, China

ARTICLE INFO

Keywords:
Lithium ion batteries
Anode
Metal organic framework
Tin dioxide
Graphene
Composite

ABSTRACT

SnO_2 is one of the most promising anode materials for lithium ion batteries (LIBs). However, its cycling stability is poor due to its large volume change, and hence, its practical applications in LIBs are hindered. In this work, we propose a novel and simple strategy to enhance the performances of SnO_2-based anodes. This strategy involves optimized assembling of SnO_2 with metal organic framework (MOF) and graphene. SnO_2 nanoparticles are packed into Al-MOF in an optimum mass ratio, and then the derived SnO_2@MOF composite is wrapped by graphene, finally resulting in the SnO_2@MOF/graphene composite. This composite exhibits greatly enhanced cycling stability, i.e., the specific capacity is about 450 mA h g^{-1} after 1000 charge/discharge cycles at the current density of 1000 mA g^{-1}. This is attributed to the unique structural configuration of the composite, which gives rich accessible electroactive sites, shortened ion transport pathways, and superior electronic conductivity. The MOF protection layer is a key for improving the lithium storage of metal oxide-based anodes. Although the capacity of the SnO_2@MOF/graphene composite is not the highest among the existing anode materials, its synthesis process is simpler and cost effective.

1. Introduction

Lithium-ion batteries (LIBs) have been widely used in portable electronic devices. However, a continuously growing demand for application in large-scale energy storage devices including electric vehicles (EVs) and hybrid EVs urges the development of the next generation LIBs with significantly improved energy density and power density [1,2]. As one of the primary functional components, the anode material highly determines the performance of LIBs and has been extensively studied [3]. However, the low theoretical capacity of the commercial graphite anode (372 mA h g^{-1}) severely restricts the overall energy density of the current LIBs and limits its further applications. In efforts to solve this problem, metal oxides, nitrides, sulfides, silicon, etc. have been widely studied as anode materials owing to their high theoretical capacities and low cost [4–9].

As one of the most promising candidates for the commercial anode materials, SnO_2 has received great attention due to its high theoretical capacity, safe working potential, biological compatibility, environmental benignity and low cost [10–18]. SnO_2 was firstly reported as anode material by Idato et al. [4]. Its lithium storage performance is evaluated by performing both experiments and theoretical calculations [4,19]. The total process of lithium storage involves two steps:

$$SnO_2 + 4\ Li^+ + 4\ e^- \leftrightarrow Sn + 2\ Li_2O \quad (1)$$

$$Sn + x\ Li^+ + x\ e^- \leftrightarrow Li_xSn\ (0 \le x \le 4.4) \quad (2)$$

It should be noted that the particle size of SnO_2 plays a crucial role in determining the reversibility of Reaction 1, and thus the theoretical capacity. For bulk SnO_2 materials, Reaction 1 is considered to be irreversible, resulting in a relatively low theoretical capacity of about 780 mA h g^{-1} [20–22]. However, when the particle size of SnO_2 decreases to nanoscale, Reaction 1 becomes reversible or partly reversible and the theoretical capacity increases to the value of 1494 mA h g^{-1} [23,24]. Reaction 2 is widely believed to be reversible in terms of alloying and

* Corresponding author. School of Materials Science and Engineering, Qilu University of Technology (Shandong Academy of Science), Jinan, 250353, China.
** Corresponding author.
E-mail addresses: zhang-yanfei@hotmail.com (Y. Zhang), yy@bio.aau.dk (Y. Yue).

https://doi.org/10.1016/j.nanoen.2020.104868
Received 12 March 2020; Received in revised form 16 April 2020; Accepted 19 April 2020
Available online 12 May 2020

dealloying of lithium with Sn. However, despite its high capacity, the SnO_2 nanoparticle-based anode undergoes a huge volume change up to 250% during lithiation and delithiation processes. This leads to both structural collapse of SnO_2 and formation of the unstable solid electrolyte interface (SEI) layer, consequently resulting in poor cycling performance, i.e., the rapidly fading capacity [25]. To tackle this problem, carbon matrix was often used to protect SnO_2, and thereby to improve its cycling stability [26]. The high mechanical strength and flexibility of carbon matrix could accommodate the huge volume expansion during cycling, and thus ensure the integrity of the whole electrode. In addition, the electronic conductivity of the anode can be improved by combining SnO_2 with carbon matrix. Therefore, various kinds of carbon matrixes, such as amorphous carbon, carbon nanotube and graphene, were tested as the protecting layer to enhance the cycling performance of SnO_2 [27–30].

However, the common drawback of the carbon coating method is that the particle size of SnO_2 cannot be readily controlled during the synthesis process. The particle size of SnO_2 is an important factor for determining the reversibility of the conversion reaction from SnO_2 to Sn (Reaction (1)) for lithium storage [31]. That is to say, the size effect of SnO_2 particles is critical for the capacity of the anode material. Moreover, the nanosized SnO_2 can not only shorten the diffusion path of electrons and Li^+ ions and withstand large volume variations, but also improve the contact between the electrolytes and anodes [32]. To adjust the particle size of SnO_2, several methods, e.g., controlling temperature, pressure, additives, have been proposed [17,33,34]. However, to the best of our knowledge, the effective method for packing the nanosized SnO_2 particles into MOF has not been reported. If this can be realized, the mechanical stability of the SnO_2-based anode can be enhanced during charge/discharge cycling since it can tolerate volume expansion.

In this work, we develop the SnO_2@MOF/graphene composite anode, in which SnO_2 nanoparticles are packed into a metal organic framework (MOF), specifically, Al-MOF. For convenience, Al-MOF is called MOF hereafter. In detail, SnO_2 nanoparticles are trapped inside the pores of Al-MOF by a wet impregnation process. Thus, the volume changes of SnO_2 during charge/discharge processes can be tolerated by Al-MOF and a stable SEI film could be maintained. In addition, the Sn nanoparticles derived from SnO_2 tend to aggregate to larger Sn clusters during the electrochemical alloying-dealloying process, leading to the capacity decay [35,36]. However, the Al-MOF layer in SnO_2@MOF/-graphene composite will be capable of effectively avoiding Sn clustering. Considering the low electronic conductivity of SnO_2 and MOF, we introduced the graphene sheets to wrap the SnO_2@MOF composite in order to enhance the electronic conductivity. Moreover, graphene itself has a decent theoretical capacity as an anode material, as well as large surface area and high mechanical flexibility [37]. As a result of the synergistic effect, the SnO_2@MOF/graphene anode exhibits an outstanding lithium storage performance with greatly enhanced capacity and excellent cycling stability.

2. Experimental section

2.1. Synthesis of SnO_2@MOF/graphene

The Al-MOF was prepared using a method reported elsewhere [38]. In detail, aluminum nitrate nonahydrate (1.3 g, 3.5 mmol) and 1,4-benzenedioic acid (0.288 g, 1.7 mmol) were dissolved in 30 ml deionized water. The obtained solution was transferred to a 50 ml Teflon lined high-pressure autoclave. After sealing, the autoclave was kept at 220 °C for 3 days and then naturally cooled down to room temperature. The precipitation was collected by centrifugation and washed several times with de-ionized water. Then the product was heated at 330 °C in air for 3 days to remove the guest molecules from the pores. Graphene oxide (GO) was prepared by the modified Hummer's method and used as the precursor for the graphene [39]. To prepare the SnO_2@MOF composite, a wet impregnation method was adopted [40,41]. In detail, 100 mg MOF particles were dispersed in H_2O and the mixture was stirred for 12 h. Then 1350 mg $SnCl_2{\cdot}2H_2O$ was added to the mixture and stirred for 72 h to ensure the complete reaction from $SnCl_2{\cdot}2H_2O$ to SnO_2 (897 mg SnO_2 could be obtained if the yield is 100%). After centrifugation and drying of the mixture, 285 mg of the as-prepared SnO_2@MOF was dispersed in 30 mL graphene oxide aqueous dispersion (0.5 mg mL^{-1}). After that, 120 mg VC was added, and the obtained dispersion was stirred for 0.5 h. This mixture was transferred into an oven and heated at 90 °C for 1 h. The final product was collected by centrifugation and dried at 120 °C under vacuum. For comparison, we also prepared the SnO_2@MOF/-graphene with various mass percentages of SnO_2 and the pure SnO_2 particles under the same experimental conditions. In addition, the physical mixture of SnO_2 and MOF prepared by grinding them together was also provided for comparison.

2.2. Materials characterizations

Powder X-ray diffraction (XRD) measurements of the samples were performed on a PANalytical X-ray diffractometer with Cu Kα (λ = 1.5406 Å) radiation during the 2θ range of 5–60° with a step size of 0.013°. Raman spectroscopy measurements were conducted via Renishaw In-Via Raman microscopic with an Ar^+ laser (λ = 785 nm) at 50 × aperture. Thermogravimetric (TG) curves were collected from a Thermogravimetric Analyzers Discovery. Fourier transform infrared (FTIR) spectra were recorded on a Bruker TENSOR II FTIR spectrometer with Platinum ATR Accessory at room temperature in the range of 400–4000 cm^{-1}. X-ray photoelectron spectroscopy (XPS) was performed by using ESCALAB 250Xi spectrometer (ThermoFisher Scientific, USA)

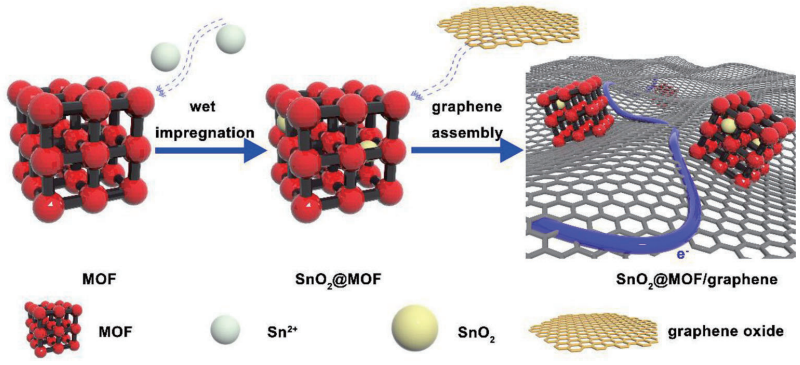

Scheme 1. Preparation of SnO_2@MOF and SnO_2@MOF/graphene (The blue line in SnO_2@MOF/graphene represents the electron transport path).

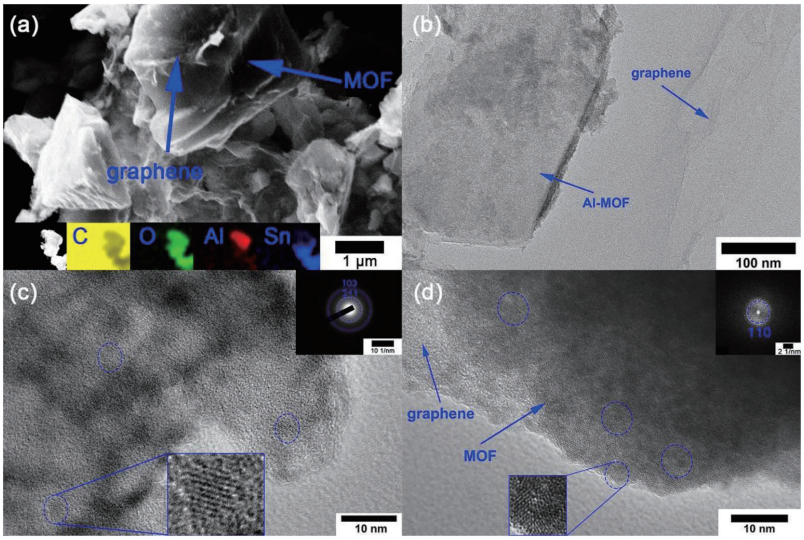

Fig. 1. Microscopic characterizations. (a) SEM image of SnO_2@MOF/graphene (Inset: EDS elemental mappings of C, O, Al and Sn); (b) TEM image of SnO_2@MOF/graphene. (c) HRTEM image of SnO_2@MOF; (d) HRTEM image of SnO_2@MOF/graphene; Insets in (c) and (d): electron diffraction.

with non-monochromatic Al Ka X-ray (1486.6 eV) at pass energy of 50 eV. Scanning electron microscopy (SEM) measurements were conducted using Zeiss Gemini SEM 500. Transmission electron microscopy (TEM) measurements were carried out using a JEM-2100F (JEOL Ltd., Japan) in the scanning TEM mode.

2.3. Electrochemical measurements

The electrochemical performances of the as-prepared SnO_2@MOF/graphene and other samples were evaluated by coin-type cell CR2032 with metallic lithium foil (diameter of 10.0 mm) as the counter electrode. The electrolyte consists of 1 M $LiPF_6$ in ethylene carbonate (EC)/diethyl carbonate (DEC)/dimethyl carbonate (DMC) (1:1:1 vol%) and a Celgard 2325 membrane (diameter of 19.0 mm) functions as the separator. The working electrodes were prepared by mixing 70 wt% active materials, 20 wt% acetylene black and 10 wt% polyvinylidene difluoride (PVDF) into a slurry and pasting onto the copper foil. After being dried at 110 °C in a vacuum oven for 12 h, the foil was cut into circular electrode with a diameter of 12 mm. The loading mass of active materials is 1–2 mg, based on which the gravimetric capacity was calculated. The cells were assembled in an Argon-filled glovebox with both the moisture and the oxygen content below 1 ppm and tested at 25 °C. The galvanostatic charge/discharge tests of the cells were conducted on a Land battery test system (CT2001A). Cyclic voltammetry (CV) curves were recorded in the voltage range of 0.01–3 V at the scanning rate of 0.1 mV s^{-1} and EIS spectra were obtained in the frequency range of 0.1 Hz to 100 kHz on a CHI 760e electrochemical workstation with an amplitude of 5 mV.

3. Results and discussion

3.1. Synthesis and characterization of SnO_2@MOF/graphene

As illustrated in Scheme 1, SnO_2@MOF was prepared via a wet impregnation method. First, the MOF particles were well dispersed and stirred in water. Then, $SnCl_2{\cdot}2H_2O$ was dissolved into the above suspension. The Sn^{2+} ions were trapped in pores of MOF by both the capillary force and the electrostatic forces between MOF and Sn^{2+} ions during the wet impregnation process [40,41]. When exposed to air, the Sn^{2+} ions in the suspension were oxidized to SnO_2. In the meantime, the micropores in MOF act as templates for the controllable growth of nanosized SnO_2. Then, the as-prepared SnO_2@MOF were dispersed into the graphene oxide (GO) aqueous suspension. The SnO_2@MOF particles gradually anchored on the surface of GO sheets during this process since the carboxyl and hydroxyl groups on the GO surface could serve as the junctions for the SnO_2@MOF particles. Afterwards, Vitamin C were added to the suspension to convert GO into the reduced graphene oxide that is noted as graphene for simplicity. Upon heat treatment at 90 °C for 1 h, the SnO_2@MOF/graphene composite was finally obtained. The graphene could enhance the electronic conductivity and the capacity of the composite anode, while the MOF could control the sizes of SnO_2 nanoparticles and protect the composite from structure degradation during cycling. All the above-mentioned effects synergistically contribute to the lithium storage performance of the SnO_2@MOF/graphene.

The morphologies of the as-prepared SnO_2@MOF/graphene and SnO_2@MOF were investigated via scanning electron microscope (SEM) and transmission electron microscope (TEM). Representative SEM and TEM images of the samples are shown in Fig. 1 and Figs. S1–S5. As seen in Fig. 1a, the SnO_2@MOF/graphene is composed of cuboid particles with size of about 1 μm. In addition, the graphene sheets could also be observed, which cover the SnO_2@MOF particles. The EDS elemental mappings of C, O, Al and Sn (inset of Fig. 1a) illustrate their uniform distribution in SnO_2@MOF/graphene. TEM results (Fig. 1b) reveal that the graphene sheets well adhere to nanoparticles of SnO_2@MOF, implying the robust combination of the three components. High-resolution TEM (HRTEM) images of SnO_2@MOF (Fig. 1c) and SnO_2@-MOF/graphene (Fig. 1d) provide information on both the size and the structure of SnO_2 particles. Evidently, SnO_2 nanoparticles (<5 nm) (blue circles) are uniformly embedded in MOF matrix. The lattice fringes of about 0.33 nm can be clearly seen in the HRTEM image for both the as-prepared SnO_2@MOF/graphene and SnO_2@MOF. These results confirm that Sn^{2+} ions from $SnCl_2{\cdot}2H_2O$ were trapped in Al-MOF and further oxidized to the nanosized SnO_2. Moreover, upon combining with graphene sheets, the nanosized SnO_2 particles and MOF give rise to the structural and chemical stability of SnO_2@MOF.

Fig. 2a shows the X-ray diffraction (XRD) patterns of both the as-

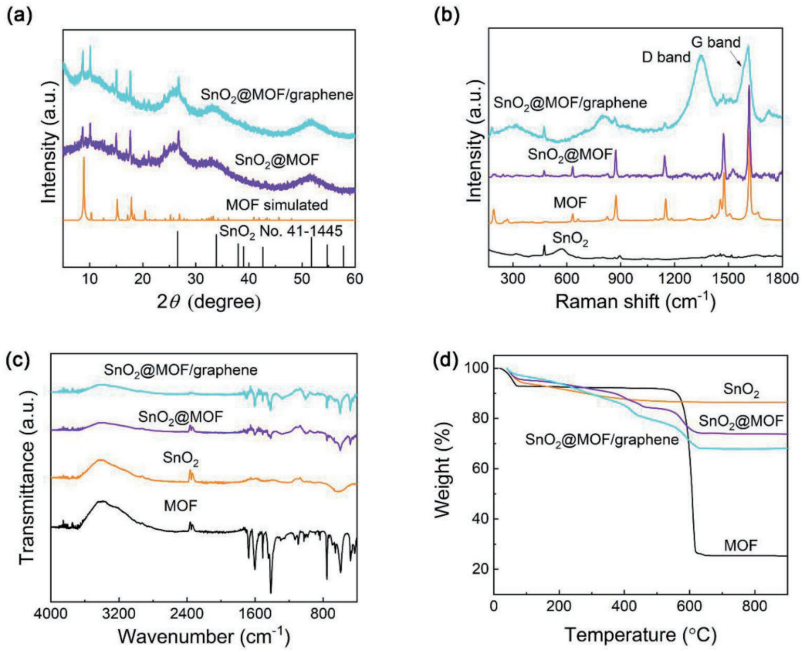

Fig. 2. Structural and thermal analyses. (a) XRD patterns of simulated SnO_2, simulated MOF, SnO_2@MOF and SnO_2@MOF/graphene; (b) Raman spectra; (c) FTIR spectra; (d) Thermogravimetry curves reflecting the mass change during heating for as-prepared SnO_2, MOF, SnO_2@MOF and SnO_2@MOF/graphene.

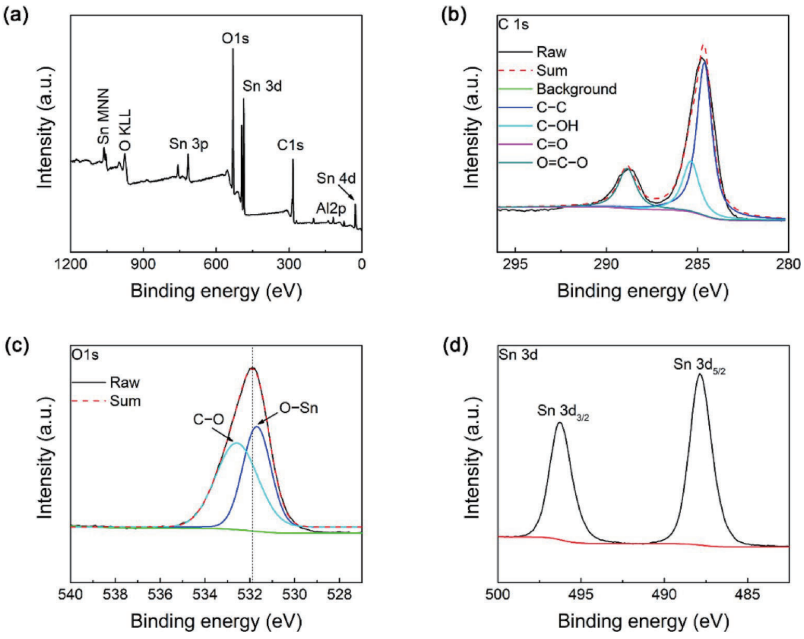

Fig. 3. Investigation on the chemical composition. XPS survey spectrum of SnO_2@MOF/graphene (a), and high-resolution spectra of C 1s (b), O 1s (c) and Sn 3d (d).

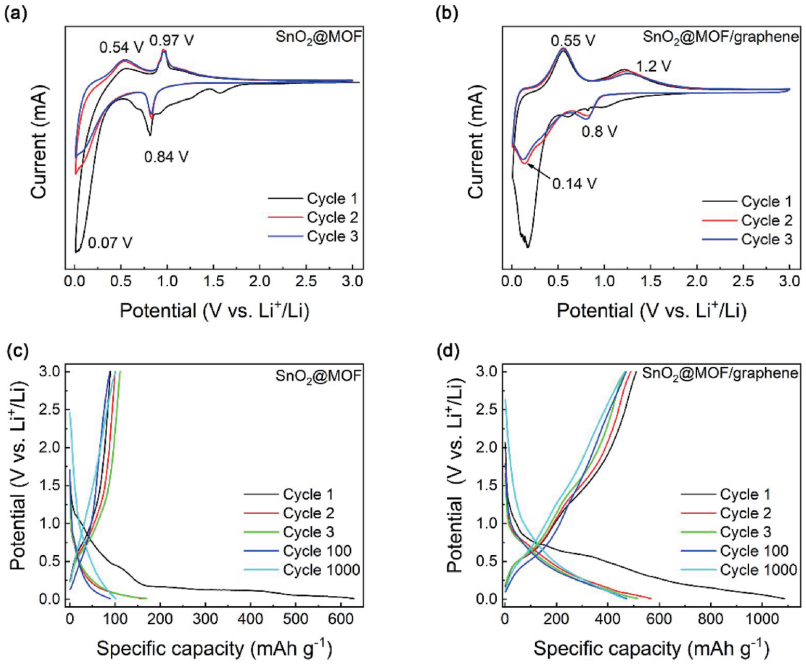

Fig. 4. Electrochemical properties. Cyclic voltammetry curves of (a) SnO_2@MOF and (b) SnO_2@MOF/graphene within the range from 0.01 to 3 V at a scan rate of 0.1 mV s^{-1}. Galvanostatic charge/discharge profiles of the initial three, 100th and 1000th cycles of (c) SnO_2@MOF and (d) SnO_2@MOF/graphene at a current density of 1000 mA g^{-1}.

prepared SnO_2@MOF and the SnO_2@MOF/graphene composites, with sharp diffraction peaks at 2θ = 8.9, 10.3, 15.2, 17.8, 26.7°. All these peaks could be indexed to the MOF by comparing the pattern of the simulated MOF, indicating that the MOF structure was not affected by the nanosized SnO_2 formation and the graphene sheet coverage. Moreover, the broad peaks at around 26.5, 33.8 and 51.7° demonstrate the formation of SnO_2 in SnO_2@MOF and SnO_2@MOF/graphene, i.e., tetragonal rutile-like SnO_2 (JCPDS No. 41–1445, space group $P4_2/mnm$, $a_0 = b_0$ = 4.738 Å, c_0 = 3.187 Å) [42]. According to the Scherrer equation, the crystal size of the SnO_2 is estimated to be around 2 nm, being consistent with the HRTEM results.

To identify the structures of as-prepared SnO_2, MOF, SnO_2@MOF and SnO_2@MOF/graphene, Raman spectra were collected (Fig. 2b). In the spectrum of SnO_2, the sharp peak at 474 cm^{-1} is assigned to the E_g mode of SnO_2 nanoparticles while the broad peak at around 575 cm^{-1} is attributed to the band *S1* because of disorder activation [43]. As for the spectra of SnO_2@MOF and SnO_2@MOF/graphene, the characteristic peaks at 192, 631, 872, 1150, 1472 and 1615 cm^{-1} belong to pure MOF. The peak at 474 cm^{-1}, which is ascribed to SnO_2, confirms the coexistence of MOF and SnO_2. In addition, SnO_2@MOF/graphene also exhibits two broad bands at 1350 and 1590 cm^{-1} that originate from the first order scattering of the E_{2g} mode and the structural defects of graphene sheets, respectively, implying the tight combination of SnO_2@MOF and graphene [44]. Furthermore, the high-intensity G band reveals a high graphitization degree of SnO_2@MOF/graphene due to the addition of graphene sheets.

Fig. 2c shows the Fourier transform infrared (FTIR) spectra of SnO_2, SnO_2@MOF and SnO_2@MOF/graphene, respectively. Both the SnO_2@MOF and SnO_2@MOF/graphene exhibit the characteristic bands at around 1600, 1500 and 1410 cm^{-1}, which could be attributed to carboxyl group ($-CO_2$) asymmetric and symmetric stretching. Besides these bands, a broad band at around 620 cm^{-1} in the spectra of SnO_2@MOF/graphene was also observed, resulting from the antisymmetric Sn–O–Sn stretching [45]. This implies the existence of SnO_2 in the SnO_2@MOF and SnO_2@MOF/graphene.

Thermogravimetric analysis (TG) of the SnO_2, MOF, SnO_2@MOF and SnO_2@MOF/graphene were carried out to measure the mass loss as a function of temperature in atmospheric air at the heating rate of 10 °C min^{-1}. The TG curves are shown in Fig. 2d. The SnO_2 exhibits high thermal stability up to 900 °C except the initial mass loss. The TG curve of MOF indicates the following two main thermal events. The initial mass loss of 8% occurs when the temperature increases from room temperature to about 100 °C, owing to the loss of absorbed water inside MOF. The second predominant mass loss of about 65% takes place at about 600 °C, which is ascribed to the decomposition of MOF. Notably, the SnO_2@MOF and SnO_2@MOF/graphene show similar thermal stability. Their mass losses below 400 °C are related to the expulsion of water molecules and guest ligands inside MOF. A sharp mass loss slightly above 600 °C is observed, which is associated with the decomposition of MOF, implying the existence of MOF in SnO_2@MOF and SnO_2@MOF/graphene. After the sharp mass drop, there are no noticeable thermal events, and the remaining mass should mainly originate from the remained SnO_2 in SnO_2@MOF and SnO_2@MOF/graphene, respectively. By comparing the mass loss, the SnO_2 content in SnO_2@MOF is calculated to be about 85%. In addition, the incorporation of SnO_2 particles into the pores of MOF is confirmed by the decrease of the surface area of 1112 m^2 g^{-1} for MOF to 150 m^2 g^{-1} for SnO_2@MOF/graphene, as well as by the total decrease of the micropore volume from 0.18 to 0.14 cm^3 g^{-1} upon impregnation (Fig. S6).

X-ray photoelectron spectroscopy (XPS) was conducted to analyze the chemical composition of SnO_2@MOF/graphene. The survey spectrum reveals the presence of C, O, Al and Sn elements (Fig. 3a). Fig. 3b shows the high-resolution spectrum of C 1s, which was fitted by four peaks at 284.8, 285.6, 286.6 and 288.9 eV, corresponding to C–C, C–OH,

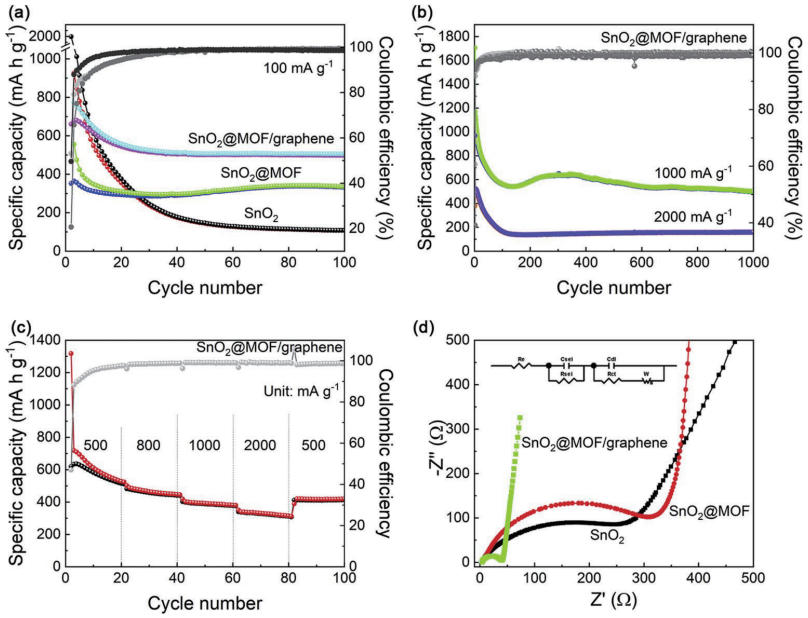

Fig. 5. Electrochemical properties. Cycling performance of (a) SnO_2, SnO_2@MOF and SnO_2@MOF/graphene at a current density of 100 mA g^{-1} and (b) SnO_2@MOF/graphene at current densities of 1000 and 2000 mA g^{-1}. (c) Rate performance of SnO_2@MOF/graphene at current densities of 500, 800, 1000, 2000, and 500 mA g^{-1}, respectively. (d) Nyquist plots of SnO_2, SnO_2@MOF and SnO_2@MOF/graphene (Inset: the equivalent circuit).

C═O, and O═C–O functional groups, respectively [44]. The graphitic carbon arises from graphene, while the oxygen-contained groups mainly originate from the organic ligands. As shown in Fig. 3c, the pronounced O 1s response could be deconvoluted into two components at 531.6 eV and 532.6 eV, which are attributed to the carboxyl groups of organic ligands and SnO_2, respectively [46]. In the high-resolution XPS spectrum of Sn 3d (Fig. 3d), two distinct peaks appear at binding energies of 487.8 eV for Sn $3d_{5/2}$ and 496.2 eV for Sn $3d_{3/2}$, resulting in an energy difference of 8.4 eV. This value agrees with that previously reported for SnO_2, confirming that tin in the composite exists as Sn^{4+} [47]. The above XPS results indicate that the SnO_2@MOF/graphene composite consists of three components, i.e., SnO_2, MOF and graphene.

3.2. Electrochemical performances

The electrochemical reaction mechanism during cycling of SnO_2@MOF and SnO_2@MOF/graphene can be clarified in terms of the cyclic voltammogram (CV) curves. Fig. 4a and b show the CV curves of the initial three cycles of SnO_2@MOF and SnO_2@MOF/graphene at a scan rate of 0.1 mV s^{-1} between 0.01 and 3 V. SnO_2@MOF exhibits two pronounced peaks at 0.84 and 0.07 V in the first cathodic scan (Fig. 4a), which are ascribed to the insertion of Li^+ ions into MOF and the formation of solid electrolyte interface (SEI) film, respectively. In addition, the peak located in the potential range of 0.6–1.0 V (Fig. 4a) is caused by the reduction of SnO_2 to Sn. In the following anodic scan, the peaks at 0.54 and 0.97 V originate from the dealloying process of Li_xSn and Li^+ ions extraction from MOF, respectively, and the former process resembles the CV behavior of SnO_2 (Fig. S7) [48]. Note that the peaks related to Li^+ ions extraction from MOF (at 0.97 and 0.84 V) for cycle 1 (Fig. 4a) are stronger than that assigned to SnO_2 (at 1.2 and 0.8 V) (Fig. 4b). This also means that MOF in SnO_2@MOF anode gives more contributions to the generation of current than SnO_2. Interestingly, SnO_2@MOF/graphene anode exhibits the CV curves with two couples of redox peaks at 0.14/0.55 V and 0.8/1.2 V. These curves are different from those of SnO_2@MOF anode, and they are associated with the alloying/dealloying process of Li_xSn and the partial reversible transformation between Sn and SnO_2, respectively [49]. The peaks at 0.97/0.84 V (Fig. 4a), which are ascribed to the interaction between lithium and MOF, are shadowed by the couple of strong peaks assigned to the reversible transformation of SnO_2 at 0.8/1.2 V. By adding graphene sheets, the peaks of SnO_2 (at 0.14/0.55 V) for cycles 2 and 3 become more pronounced compared to SnO_2@MOF since a larger fraction of the embedded SnO_2 nanoparticles in SnO_2@MOF/graphene anode could participate in redox reactions and thereby contribute to the lithium storage owing to the graphene-induced enhancement of electronic conductivity. After the initial cycle, the CV curves of SnO_2@MOF/graphene remain steady in the subsequent two cycles, indicating highly reversible electrochemical reactions and excellent structural stability.

Fig. 4c and d show the galvanostatic charge/discharge profiles of both SnO_2@MOF and SnO_2@MOF/graphene for the initial three, the 100th and 1000th cycles at a current density of 1000 mA g^{-1} over a potential range between 0.01 and 3 V (vs. Li^+/Li). In consistence with the aforementioned CV results, a weak plateau appears at around 0.9 V in the discharging curve of SnO_2@MOF anode (Fig. 4c), which arises from the interaction between Li^+ ions and MOF. In the charging profiles, the plateaus at about 0.6 and 1.0 V originate from the dealloying processes of Li_xSn and the lithium extraction from MOF, respectively. However, for SnO_2@MOF/graphene (Fig. 4d), the plateaus locate at 0.8 and 1.2 V in the galvanostatic charge/discharge curves, respectively, which are related to the reversible conversion between SnO_2 and Li_xSn. Evidently, the plateaus remain steady at 0.8/1.2 V upon 1000 cycles, indicating highly reversible electrochemical reactions between SnO_2 and Li^+ ions. In addition, the first cycle charge/discharge capacities of SnO_2@MOF/graphene anode are found to be 1086 and 510 mA h g^{-1}, respectively, and this yields the Coulombic efficiency (CE) of 47%. In a normal case, the CE of the composite should be lower, since the graphene is introduced, which has a huge surface, and hence could generate

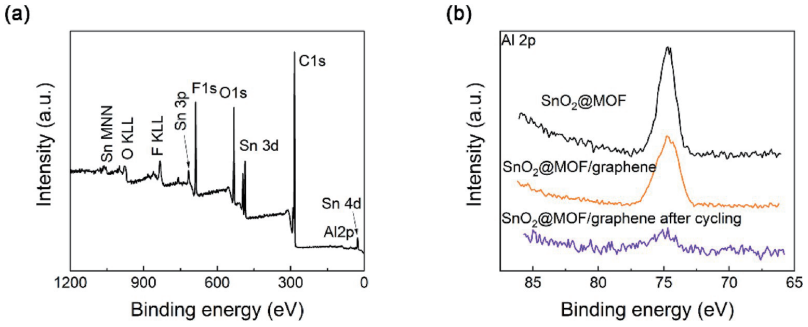

Fig. 6. Material Characterization after electrochemical tests. (a) XPS survey spectrum of SnO_2@MOF/graphene after cycling. (b) XPS core level of Al 2p of SnO_2@MOF, SnO_2@MOF/graphene and SnO_2@MOF/graphene after cycling.

large SEI, and therefore large capacity loss. However, the initial CE of the composite studied in this work is higher than that (34%) of SnO_2@MOF anode. The reason for this might be as follows. When wrapping SnO_2@MOF with graphene, the surface area of MOF decreases since the graphene blocks part of the pores of MOF. Consequently, less lithium will be trapped in the pores of MOF with graphene than the MOF without graphene, leading to a higher CE for the first cycle. However, the CE of our composite is still relatively low for LIBs. This problem should be solved by other means, e.g., pre-lithiation process.

Remarkably, from the second cycle, the CE of the SnO_2@MOF/graphene anode can reach nearly 100%, and the capacity can still remain at 460 mA h g^{-1} at 1000th cycle, considerably higher than that of SnO_2@MOF anode. This high reversible capacity of SnO_2@MOF/graphene could be ascribed to the fact that not only MOF protects nanosized SnO_2 particles from aggregation and pulverization during lithium insertion/extraction processes, but also the graphene sheets provide higher electronic conductivity, higher mechanical flexibility and chemical stability.

The cycling performances of SnO_2, SnO_2@MOF and SnO_2@MOF/graphene were studied by galvanostatic charge/discharge in the voltage range from 0.01 to 3 V at a current density of 100 mA g^{-1}. As shown in Fig. 5a, the initial charge/discharge capacities are 1996/1060, 1700/352, 1332/660 for SnO_2, SnO_2@MOF and SnO_2@MOF/graphene, leading to the capacity losses of about 50%, 80% and 50%, respectively. The initial abrupt capacity decays for the three samples could be due to both SEI formation and incomplete delithiation processes. As depicted in Fig. 5a, SnO_2@MOF/graphene anode shows superior cycling performance and largest capacity compared to SnO_2 and SnO_2@MOF counterparts during the 2nd to 100th cycles. The specific capacity of the SnO_2@MOF/graphene anode retains 500 mA h g^{-1} after 100 cycles. In contrast, the capacity of SnO_2 anode decreases to less than 100 mA h g^{-1} within the first 50 cycles. The capacity of SnO_2@MOF preserves only about 330 mA h g^{-1} after 100 cycles. The poor cycling stability of SnO_2 anode is ascribed to its structural degradation caused by the large volume expansion and the aggregation of Sn nanoparticles. However, in the case of SnO_2@MOF/graphene anode, the volume expansion of Sn nanoparticles is confined in the pores of the Al-MOF and the aggregation of Sn nanoparticles are hindered by both the Al-MOF and graphene matrixes. Thus, SnO_2@MOF/graphene could keep the capacities of 450 and 160 mA h g^{-1} after 1000 cycles at even higher current density of 1000 and 2000 mA g^{-1} (Fig. 5b), respectively, i.e., exhibits superior cycling stability. The stabilized structure against Li^+ ions insertion/extraction of this composite anode can also be reflected by its rate performance. Fig. 5c shows the rate capability of SnO_2@MOF/graphene at the rates of 500, 800, 1000, 2000 mA g^{-1} with the high steady capacities of 565, 450, 385, and 324, respectively. The capacity recovers to 410 mA h g^{-1} when the current density decreases again to 500 mA g^{-1} after 100 cycles.

Electrochemical impedance spectroscopy (EIS) measurements were conducted to evaluate the electrochemical performances. The Nyquist plots of SnO_2, SnO_2@MOF and SnO_2@MOF/graphene show similar shapes, consisting of a depressed semicircle at high frequency region and an inclined line at low frequency range. As shown in Fig. 5d, the charge transfer resistance (R_{ct}) is reflected by the diameter of the semicircle, while the impedance of solid electrolyte interphase (SEI), which is related to Li^+ ions diffusion, is represented by the straight line. The inset is the equivalent circuit used to fit the impedance data. Since SnO_2@MOF/graphene anode involves the conductive graphene sheets, its R_{ct} is much lower than both SnO_2 and SnO_2@MOF anodes, i.e., SnO_2@MOF/graphene anode has the highest electronic conductivity.

To illustrate the role of the MOF protection, a physical mixture of SnO_2 and MOF in the mass ratio of 1:1 via grinding, was also tested as anode. As expected, the mixture shows a far worse lithium storage performance compared to both SnO_2@MOF and SnO_2@MOF/graphene (Fig. S8), indicating the important assembling role of MOF in enhancing both the capacity and cycling stability of SnO_2@MOF/graphene composite anode. To further verify the assembling role of MOF in SnO_2@MOF/graphene composite anode, XPS and TEM characterizations were conducted. XPS analysis was carried out to elucidate the chemical composition and bonding character of the composite. Fig. 6a shows the XPS survey of SnO_2@MOF/graphene after 1000 cycles, which reveals the existence of Li, C, O, F, Al and Sn. These elements originate from both the SEI layer and the composite. The core spectra of Al 2p for the as-produced SnO_2@MOF and SnO_2@MOF/graphene, and the SnO_2@MOF/graphene subjected to 1000 cycles exhibit the same peaks at around 74 eV (Fig. 6b), indicating that Al species preserve their chemical environments after lithiation/delithiation processes. The Sn 3d spectrum of SnO_2@MOF/graphene after 1000 cycles shows the same two distinct peaks at 495.8 for Sn $3d_{3/2}$ and 487.4 eV for Sn $3d_{5/2}$ like those of the SnO_2@MOF/graphene before cycling (Fig. S9). The difference of 8.4 eV between the two binding energies suggests the existence of SnO_2, confirming that SnO_2 could be regenerated from LiO_2 and Sn after delithiation processes. The greatly enhanced capacity could be attributed to the reversible reaction between SnO_2 and Li^+ ions. Apart from structural characterization, the electrochemical performances of SnO_2@MOF/graphene after cycling were also conducted. In Fig. S10a, it is seen that CV curves of SnO_2@MOF/graphene after 1000 charge/discharge cycles display two redox peaks at 0.14/0.5 V and 0.8/1.2 V, which are consistent with those of the as-prepared composite. In addition, a similar EIS plot of SnO_2@MOF/graphene after cycling to that of as-prepared SnO_2@MOF/graphene can also be observed in Fig. S10b. This implies that the lithium storage mechanism of the SnO_2@MOF/graphene is the same during each of the 1000 cycles, that is, SnO_2@MOF/graphene anode has an outstanding structural stability against repeated lithium insertion-extraction processes.

The morphology of SnO_2@MOF/graphene after cycling was

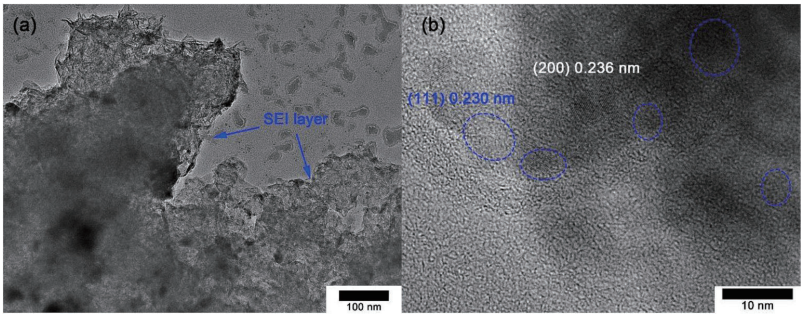

Fig. 7. Microscopic characterization after electrochemical tests. (a) TEM image of SnO_2@MOF/graphene after cycling. (b) HRTEM image of SnO_2@MOF/graphene after cycling.

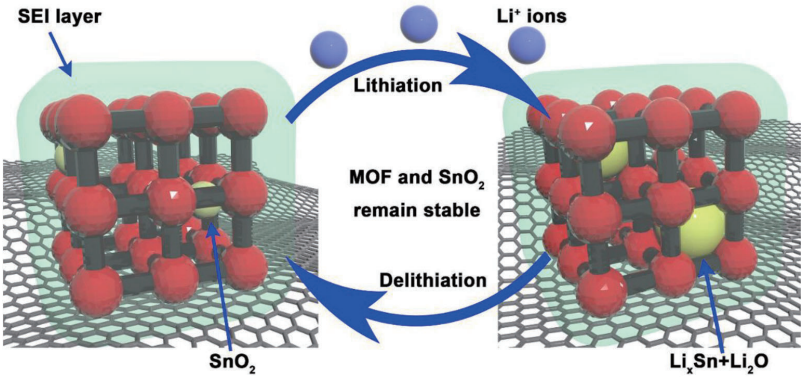

Scheme 2. Proposed mechanism for SnO_2@MOF/graphene after an SEI layer formation. The nanosized SnO_2 particles react with Li^+ ions reversibly and the MOF protect it from collapsing.

Table 1
Comparison in the lithium storage performance between the composite anode developed in this work and some recently reported SnO_2-based anodes.

Anodes	Current density (mA g^{-1})	Cycle number	Capacity (mAh g^{-1})	Reference
SnO_2@MOF/graphene	1000	1000	450	This work
SnO_2@C	1000	200	484	[51]
SnO_2@C	1000	400	656	[11]
SnO_2/N-doped C	500	100	491	[21]
Sn/SnO_x/graphene	96	250	392	[52]
SnO_2@C nanocages	5000	1000	477	[50]
SnO_2@C_3N_4	780	100	490	[53]
SnO_{2-x}/N-rGO	1000	200	652	[54]

investigated by ex-situ TEM and SEM. As shown in Fig. 7a and Fig. S11, a uniform SEI layer outside the MOF particles with a thickness of about 10 nm are observed. In Fig. 7b, the HRTEM image of SnO_2@MOF/graphene after cycling presents SnO_2 particles with diameter of about 5 nm. The lattice fringes with the spacings of 0.236 nm and 0.230 nm correspond to the (200) and (111) crystal planes of SnO_2. These results confirm that the MOF shell protects SnO_2 from aggregation and a stable SEI could be formed. These are the main reasons for the outstanding cyclic stability of SnO_2@MOF/graphene composite anode.

In Scheme 2, we propose a mechanism to illustrate how MOF protects SnO_2 upon Li^+ insertion/extraction. The SEI layer forms after the first lithiation process outside the MOF material. During the subsequent cycles, Li^+ ions could diffuse through the SEI layer and interact with SnO_2. The resulted volume changes of SnO_2 are buffered by the MOF and graphene because of their flexible porous structure. Thus, SnO_2 can react with Li^+ ions reversely to form Sn and Li_2O. Then the dealloying of Li_xSn occurs during the delithiation processes. The structure of SnO_2@MOF/graphene remains stable during both reactions, leading to a greatly enhanced cycling stability and capacity of SnO_2@MOF/graphene.

A brief comparison in the lithium storage performance between the anode developed in this work and some recently reported SnO_2-based anodes is provided in Table 1. It is noticed that most of current anode materials focus on the capacity, not on the cycling stability. However, the latter is also the determining factor for practical applications. As seen in Table 1, the SnO_2@carbon nanocage anode exhibits better performances than other SnO_2-based anodes, but it was fabricated via a different route [50]. However, in comparison to the reported approaches, the synthesis approach established in the present work is simpler and economically more effective, and hence, it has a higher potential to be up-scaled. Certainly, there is still room to improve our present approach to achieve even better anode performances.

The excellent electrochemical performance of SnO_2@MOF/graphene as anode for LIBs could be ascribed to their unique structural features in several aspects. First, the nanosized SnO_2 can be encapsulated by the nanopores in MOF, and this is beneficial to the reversible conversion between SnO_2 and Sn. Second, the MOF can effectively endure volume

changes during continuous cycling processes, hence partly alleviating the pulverization of SnO_2 and preventing detaching of the active materials from the electrode, and thereby improving the cycling stability. In addition, the formed SEI outside the MOF could remain stable during cycling, thus avoiding unnecessary loss of Li^+ ions because of the repeated breaking and forming of SEI film. Third, both the high electronic conductivity rendered by graphene integration, and favorable ion diffusion path provided by both the flexible graphene sheets and the porosity of MOF give rise to enhanced rate capability of the SnO_2@-MOF/graphene. Finally, owing to the protection role of MOF, the well-constructed robust SnO_2@MOF/graphene displays also other competitive advantages such as rich accessible electroactive sites of nanosized SnO_2, short ion transport pathways, superior electronic conductivity, and synergetic effect. In general, our anode-fabricating strategy is readily applicable to other types of anode materials with a dramatic volume change, such as other metal oxides, Si and P.

4. Conclusion

We proposed a novel approach to prepare the nanosized SnO_2 particles by using Al-MOF as both template and protecting layer, and using graphene as a promoter of electronic conductivity, aiming at improving the lithium storage performance of SnO_2 as anode for LIBs. In detail, the SnO_2@MOF was prepared by a wet impregnation method and its electronic conductivity was further improved by covering SnO_2@MOF with the graphene sheets. Thus, the SnO_2@MOF/graphene composite particles were assembled in an optimized chemical manner. This SnO_2@-MOF/graphene anode for LIB exhibited greatly enhanced electrochemical performances compared to the pure SnO_2-based anode owing to the shortened Li^+ ions diffusion distance, superior electronic conductivity, rich accessible electroactive sites and good structure stability. The SnO_2@MOF/graphene exhibited a capacity of 450 mA h g^{-1} at a current density of 1000 mA g^{-1} after 1000 cycles, whereas the pure SnO_2-based anode lost almost its total capacity after 50 cycles. In addition, the rate capability is significantly improved due to the protection of MOF. The synthesis approach established in the present work is simple and economically more effective, and hence, it has a high potential to be up-scaled. This study opens new vistas for rational design of superior anode materials for high performance LIBs.

Declaration of competing interest

The authors declare that they have no known competing financial interests or personal relationships that could have appeared to influence the work reported in this paper.

CRediT authorship contribution statement

Chengwei Gao: Methodology, Investigation, Data curation, Writing - original draft. **Zhenjing Jiang:** Data curation. **Peixing Wang:** Data curation. **Lars Rosgaard Jensen:** Methodology, Data curation. **Yanfei Zhang:** Supervision, Methodology, Writing - review & editing. **Yuanzheng Yue:** Project administration, Supervision, Writing - review & editing.

Acknowledgements

This work was financially supported by the China Scholarship Council (201707040085), National Natural Science Foundation of China (51402156), Shandong Provincial Key Project Funding (2018YFJH0402), the Colleges and Universities Twenty Terms Foundation of Jinan City (2019GXRC034) and Foundation from State Key Laboratory of Special Glass of China. We would like to thank Prof. D.Y. Wang from Aalborg University for his help with SEM measurements.

Appendix A. Supplementary data

Supplementary data to this article can be found online at https://doi.org/10.1016/j.nanoen.2020.104868.

References

[1] R. Van Noorden, The rechargeable revolution: a better battery, Nature 507 (2014) 26–28, https://doi.org/10.1038/507026a.
[2] J.B. Goodenough, Y. Kim, Challenges for rechargeable Li batteries, Chem. Mater. 22 (2010) 587–603, https://doi.org/10.1021/cm901452z.
[3] F. Wu, J. Maier, Y. Yu, Guidelines and trends for next-generation rechargeable lithium and lithium-ion batteries, Chem. Soc. Rev. 49 (2020) 1569–1614, https://doi.org/10.1039/c7cs00863e.
[4] Y. Idota, T. Kubota, A. Matsufuji, Y. Maekawa, T. Miyasaka, Tin-based amorphous oxide: a high-capacity lithium-ion-storage material, Science 276 (1997) 1395–1397, https://doi.org/10.1126/science.276.5317.1395.
[5] K. Zhang, F. Xiong, J. Zhou, L. Mai, L. Zhang, Universal construction of ultrafine metal oxides coupled in N-enriched 3D carbon nanofibers for high-performance lithium/sodium storage, Nano Energy 67 (2020) 104222, https://doi.org/10.1016/j.nanoen.2019.104222.
[6] X. Liu, J.-Q. Huang, Q. Zhang, L. Mai, Nanostructured metal oxides and sulfides for lithium-sulfur batteries, Adv. Mater. 29 (2017) 1601759, https://doi.org/10.1002/adma.201601759.
[7] Y.T. Liu, P. Zhang, N. Sun, B. Anasori, Q.Z. Zhu, H. Liu, Y. Gogotsi, B. Xu, Self-Assembly of transition metal oxide nanostructures on MXene nanosheets for fast and stable lithium storage, Adv. Mater. 30 (2018) 1707334, https://doi.org/10.1002/adma.201707334.
[8] L. Wu, J. Zheng, L. Wang, X. Xiong, Y. Shao, G. Wang, J.-H. Wang, S. Zhong, M. Wu, PPy-encapsulated SnS_2 nanosheets stabilized by defects on a TiO_2 support as a durable anode material for lithium-ion batteries, Angew. Chem. Int. Ed. 58 (2019) 811–815, https://doi.org/10.1002/anie.201811784.
[9] R. Gao, J. Tang, X. Yu, S. Tang, K. Ozawa, T. Sasaki, L.C. Qin, In situ synthesis of MOF-derived carbon shells for silicon anode with improved lithium-ion storage, Nano Energy 70 (2020) 104444, https://doi.org/10.1016/j.nanoen.2019.104444.
[10] M.S. Balogun, W. Qiu, Y. Luo, H. Meng, W. Mai, A. Onasanya, T.K. Olaniyi, Y. Tong, A review of the development of full cell lithium-ion batteries: the impact of nanostructured anode materials, Nano Res. 9 (2016) 2823–2851, https://doi.org/10.1007/s12274-016-1171-1.
[11] Z. Chen, Z. Xu, W. Li, C. Chen, J. Yang, J. Liu, F. Gong, J. Liao, M. Wu, Cellulose-hydrogel-derived self-activated carbon/SnO_2 nanocomposites for high-performance lithium storage, ACS Appl. Energy Mater. 2 (2019) 5171–5182, https://doi.org/10.1021/acsaem.9b00848.
[12] L. Zu, Q. Su, F. Zhu, B. Chen, H. Lu, C. Peng, T. He, G. Du, P. He, K. Chen, S. Yang, J. Yang, H. Peng, Antipulverization electrode based on low-carbon triple-shelled superstructures for lithium-Ion batteries, Adv. Mater. 29 (2017) 1–9, https://doi.org/10.1002/adma.201701494.
[13] S. Chen, M. Wang, J. Ye, J. Cai, Y. Ma, H. Zhou, L. Qi, Kinetics-controlled growth of aligned mesocrystalline SnO_2 nanorod arrays for lithium-ion batteries with superior rate performance, Nano Res. 6 (2013) 243–252, https://doi.org/10.1007/s12274-013-0300-3.
[14] X.W. Lou, C.M. Li, L.A. Archer, Designed synthesis of coaxial SnO_2@carbon hollow nanospheres for highly reversible lithium storage, Adv. Mater. 21 (2009) 2536–2539, https://doi.org/10.1002/adma.200803439.
[15] C. Wang, Y. Zhou, M. Ge, X. Xu, Z. Zhang, J.Z. Jiang, Large-scale synthesis of SnO_2 nanosheets with high lithium storage capacity, J. Am. Chem. Soc. 132 (2010) 46–47, https://doi.org/10.1021/ja909321d.
[16] V. Aravindan, K.B. Jinesh, R.R. Prabhakar, V.S. Kale, S. Madhavi, Atomic layer deposited (ALD) SnO_2 anodes with exceptional cycleability for Li-ion batteries, Nano Energy 2 (2013) 720–725, https://doi.org/10.1016/j.nanoen.2012.12.007.
[17] R. Hu, H. Zhang, Z. Lu, J. Liu, M. Zeng, L. Yang, B. Yuan, M. Zhu, Unveiling critical size of coarsened Sn nanograins for achieving high round-trip efficiency of reversible conversion reaction in lithiated SnO_2 nanocrystals, Nano Energy 45 (2018) 255–265, https://doi.org/10.1016/j.nanoen.2018.01.007.
[18] Y. Jiang, Y. Wan, W. Jiang, H. Tao, W. Li, S. Huang, Z. Chen, B. Zhao, Stabilizing the reversible capacity of SnO_2/graphene composites by Cu nanoparticles, Chem. Eng. J. 367 (2019) 45–54, https://doi.org/10.1016/j.cej.2019.02.141.
[19] A. Nie, L.Y. Gan, Y. Cheng, H. Asayesh-Ardakani, Q. Li, C. Dong, R. Tao, F. Mashayek, H.T. Wang, U. Schwingenschlögl, R.F. Klie, R.S. Yassar, Atomic-scale observation of lithiation reaction front in nanoscale SnO_2 materials, ACS Nano 7 (2013) 6203–6211, https://doi.org/10.1021/nn402125e.
[20] X. Wang, X. Cao, L. Bourgeois, H. Guan, S. Chen, Y. Zhong, D.M. Tang, H. Li, T. Zhai, L. Li, Y. Bando, D. Golberg, N-doped graphene-SnO_2 sandwich paper for high-performance lithium-ion batteries, Adv. Funct. Mater. 22 (2012) 2682–2690, https://doi.org/10.1002/adfm.201103110.
[21] X. Zhou, L. Yu, X.W.D. Lou, Formation of uniform N-doped carbon-coated SnO_2 submicroboxes with enhanced lithium storage properties, Adv. Energy Mater. 6 (2016) 1–6, https://doi.org/10.1002/aenm.201600451.
[22] B. Scrosati, J. Garche, Lithium batteries: status, prospects and future, J. Power Sources 195 (2010) 2419–2430, https://doi.org/10.1016/j.jpowsour.2009.11.048.
[23] X. Zhou, L.J. Wan, Y.G. Guo, Binding SnO_2 nanocrystals in nitrogen-doped graphene sheets as anode materials for lithium-ion batteries, Adv. Mater. 25 (2013) 2152–2157, https://doi.org/10.1002/adma.201300071.

[24] H.X. Zhang, C. Feng, Y.C. Zhai, K.L. Jiang, Q.Q. Li, S.S. Fan, Cross-stacked carbon nanotube sheets uniformly loaded with SnO_2 nanoparticles: a novel binder-free and high-capacity anode material for lithium-ion batteries, Adv. Mater. 21 (2009) 2299–2304, https://doi.org/10.1002/adma.200802290.
[25] I.A. Courtney, J.R. Dahn, Electrochemical and in situ X-ray diffraction studies of the reaction of lithium with tin oxide composites, J. Electrochem. Soc. 144 (1997) 2045–2052, https://doi.org/10.1149/1.1837740.
[26] S.J.R. Prabakar, Y.H. Hwang, E.G. Bae, S. Shim, D. Kim, M.S. Lah, K.S. Sohn, M. Pyo, SnO_2/Graphene Composites with self-assembled alternating oxide and amine layers for high Li-storage and excellent stability, Adv. Mater. 25 (2013) 3307–3312, https://doi.org/10.1002/adma.201301264.
[27] J. Liang, X.-Y. Yu, H. Zhou, H. Bin Wu, S. Ding, X.W.D. Lou, Bowl-like SnO_2@ Carbon hollow particles as an advanced anode material for lithium-ion batteries, Angew. Chem. Int. Ed. 53 (2014) 12803–12807, https://doi.org/10.1002/anie.201407917.
[28] P. Lian, X. Zhu, S. Liang, Z. Li, W. Yang, H. Wang, High reversible capacity of SnO_2/graphene nanocomposite as an anode material for lithium-ion batteries, Electrochim. Acta 56 (2011) 4532–4539, https://doi.org/10.1016/j.electacta.2011.01.126.
[29] X. Zhou, S. Chen, J. Yang, T. Bai, Y. Ren, H. Tian, Metal-organic frameworks derived okra-like SnO_2 encapsulated in nitrogen-doped graphene for lithium ion battery, ACS Appl. Mater. Interfaces 9 (2017) 14309–14318, https://doi.org/10.1021/acsami.7b04584.
[30] J. Han, D. Kong, W. Lv, D.M. Tang, D. Han, C. Zhang, D. Liu, Z. Xiao, X. Zhang, J. Xiao, X. He, F.C. Hsia, C. Zhang, Y. Tao, D. Golberg, F. Kang, L. Zhi, Q.H. Yang, Caging tin oxide in three-dimensional graphene networks for superior volumetric lithium storage, Nat. Commun. 9 (2018) 1–9, https://doi.org/10.1038/s41467-017-02808-2.
[31] K. Zhao, L. Zhang, R. Xia, Y. Dong, W. Xu, C. Niu, L. He, M. Yan, L. Qu, L. Mai, SnO_2 quantum dots@Graphene oxide as a high-rate and long-life anode material for lithium-ion batteries, Small 12 (2016) 588–594, https://doi.org/10.1002/smll.201502183.
[32] R. Hu, Y. Ouyang, M. Zhu, D. Chen, G. Waller, Y. Chen, B. Zhao, B. Rainwater, M. Liu, C. Yang, Y. Ouyang, Y. Chen, B. Zhao, B. Rainwater, C. Yang, M. Zhu, M. Liu, Dramatically enhanced reversibility of Li_2O in SnO_2-based electrodes: the effect of nanostructure on high initial reversible capacity, Energy Environ. Sci. 9 (2016) 595–603, https://doi.org/10.1039/C5EE03367E.
[33] H.J. Ahn, H.C. Choi, K.W. Park, S. Bin Kim, Y.E. Sung, Investigation of the structural and electrochemical properties of size-controlled SnO_2 nanoparticles, J. Phys. Chem. B 108 (2004) 9815–9820, https://doi.org/10.1021/jp035769n.
[34] M.A. Han, H.J. Kim, H.C. Lee, J.S. Park, H.N. Lee, Effects of porosity and particle size on the gas sensing properties of SnO_2 films, Appl. Surf. Sci. 481 (2019) 133–137, https://doi.org/10.1016/j.apsusc.2019.03.043.
[35] I.A. Courtney, W.R. McKinnon, J.R. Dahn, On the aggregation of tin in SnO composite glasses caused by the reversible reaction with lithium, J. Electrochem. Soc. 146 (1999) 59–68, https://doi.org/10.1149/1.1391565.
[36] I.A. Courtney, J.R. Dahn, Key factors controlling the reversibility of the reaction of lithium with SnO_2 and Sn_2BPO_6 glass, J. Electrochem. Soc. 144 (1997) 2943–2948, https://doi.org/10.1149/1.1837941.
[37] E.J. Yoo, J. Kim, E. Hosono, H.S. Zhou, T. Kudo, I. Honma, Large reversible Li storage of graphene nanosheet families for use in rechargeable lithium ion batteries, Nano Lett. 8 (2008) 2277–2282, https://doi.org/10.1021/nl800957b.
[38] T. Loiseau, C. Serre, C. Huguenard, G. Fink, F. Taulelle, M. Henry, T. Bataille, G. Férey, A rationale for the large breathing of the porous aluminum terephthalate (MIL-53) upon hydration, Chem. Eur J. 10 (2004) 1373–1382, https://doi.org/10.1002/chem.200305413.
[39] W.S. Hummers, R.E. Offeman, Preparation of graphitic oxide, J. Am. Chem. Soc. 80 (1958) 1339, https://doi.org/10.1021/ja01539a017.
[40] H. Zhao, H. Song, L. Chou, Nickel nanoparticles supported on MOF-5: synthesis and catalytic hydrogenation properties, Inorg. Chem. Commun. 15 (2012) 261–265, https://doi.org/10.1016/j.inoche.2011.10.040.
[41] Y. Jiao, D. Han, Y. Ding, X. Zhang, G. Guo, J. Hu, D. Yang, A. Dong, Fabrication of three-dimensionally interconnected nanoparticle superlattices and their lithium-ion storage properties, Nat. Commun. 6 (2015) 1–8, https://doi.org/10.1038/ncomms7420.
[42] J.Y. Huang, L. Zhong, C.M. Wang, J.P. Sullivan, W. Xu, L.Q. Zhang, S.X. Mao, N. S. Hudak, X.H. Liu, A. Subramanian, H. Fan, L. Qi, A. Kushima, J. Li, In situ observation of the electrochemical lithiation of a single SnO_2 nanowire electrode, Science 330 (2010) 1515–1520, https://doi.org/10.1126/science.1195628.
[43] A. Diéguez, A. Romano-Rodríguez, A. Vilà, J.R. Morante, The complete Raman spectrum of nanometric SnO_2 particles, J. Appl. Phys. 90 (2001) 1550–1557, https://doi.org/10.1063/1.1385573.
[44] D. Yang, A. Velamakanni, G. Bozoklu, S. Park, M. Stoller, R.D. Piner, S. Stankovich, I. Jung, D.A. Field, C.A. Ventrice, R.S. Ruoff, Chemical analysis of graphene oxide films after heat and chemical treatments by X-ray photoelectron and micro-Raman spectroscopy, Carbon N. Y. 47 (2009) 145–152, https://doi.org/10.1016/j.carbon.2008.09.045.
[45] F. Gu, S. Fen Wang, C. Feng Song, M. Kai Lü, Y. Xin Qi, G. Jun Zhou, D. Xu, D. Rong Yuan, Synthesis and luminescence properties of SnO_2 nanoparticles, Chem. Phys. Lett. 372 (2003) 451–454, https://doi.org/10.1016/S0009-2614(03)00440-8.
[46] S. Gao, N. Wang, S. Li, D. Li, Z. Cui, G. Yue, J. Liu, X. Zhao, L. Jiang, Y. Zhao, A multi-wall Sn/SnO_2@carbon hollow nanofiber anode material for high-rate and long-life lithium-ion batteries, Angew. Chem. 132 (2020) 2486–2493, https://doi.org/10.1002/ange.201913170.
[47] B. Tu, Y. Shao, W. Chen, Y. Wu, X. Li, Y. He, J. Li, F. Liu, Z. Zhang, Y. Lin, X. Lan, L. Xu, X. Shi, A.M.C. Ng, H. Li, L.W. Chung, A.B. Djurišić, Z. He, Novel molecular doping mechanism for n-doping of SnO_2 via triphenylphosphine oxide and its effect on perovskite solar cells, Adv. Mater. 31 (2019) 1–9, https://doi.org/10.1002/adma.201805944.
[48] C. Gao, P. Wang, Z. Wang, S.K. Kær, Y. Zhang, Y. Yue, The disordering-enhanced performances of the Al-MOF/graphene composite anodes for lithium ion batteries, Nano Energy 65 (2019) 104032, https://doi.org/10.1016/j.nanoen.2019.104032.
[49] S. Ding, J.S. Chen, G. Qi, X. Duan, Z. Wang, E.P. Giannelis, L.A. Archer, X.W. Lou, Formation of SnO_2 hollow nanospheres inside mesoporous silica nanoreactors, J. Am. Chem. Soc. 133 (2011) 21–23, https://doi.org/10.1021/ja108720w.
[50] M. Liu, H. Fan, O. Zhuo, J. Chen, Q. Wu, L. Yang, L. Peng, X. Wang, R. Che, Z. Hu, A general strategy to construct yolk-shelled metal oxides inside carbon nanocages for high-stable lithium-ion battery anodes, Nano Energy 68 (2020) 104368, https://doi.org/10.1016/j.nanoen.2019.104368.
[51] Q. Tian, F. Zhang, L. Yang, Fabricating thin two-dimensional hollow tin dioxide/carbon nanocomposite for high-performance lithium-ion battery anode, Appl. Surf. Sci. 481 (2019) 1377–1384, https://doi.org/10.1016/j.apsusc.2019.03.252.
[52] A.P. Nowak, K. Trzciński, M. Szkoda, G. Trykowski, M. Gazda, J. Karczewski, M. Łapiński, D. Maskowicz, M. Sawczak, A. Lisowska-Oleksiak, Nano tin/tin oxide attached onto graphene oxide skeleton as a fluorine free anode material for lithium-ion batteries, Inorg. Chem. (2020), https://doi.org/10.1021/acs.inorgchem.0c00318.
[53] D. Versaci, J. Amici, C. Francia, S. Bodoardo, Simple approach using g-C_3N_4 to enable SnO_2 anode high rate performance for Li ion battery, Solid State Ionics 346 (2020) 115210, https://doi.org/10.1016/j.ssi.2019.115210.
[54] N. Wu, W. Du, X. Gao, L. Zhao, G. Liu, X. Liu, H. Wu, Y.B. He, Hollow SnO_2 nanospheres with oxygen vacancies entrapped by a N-doped graphene network as robust anode materials for lithium-ion batteries, Nanoscale 10 (2018) 11460–11466, https://doi.org/10.1039/c8nr02290a.

Supporting Information

Optimized assembling of MOF/SnO_2/Graphene leads to superior anode for lithium ion batteries

Chengwei Gao[a,b], Zhenjing Jiang[a], Peixing Wang[a], Lars Rosgaard Jensen[c], Yanfei Zhang[a,*], Yuanzheng Yue[a,b,d,*]

[a] School of Materials Science and Engineering, Qilu University of Technology (Shandong Academy of Sciences), Jinan 250353, China.

[b] Department of Chemistry and Bioscience, Aalborg University, 9220 Aalborg, Denmark.

[c] Department of Materials and Production, Aalborg University, 9220 Aalborg, Denmark.

[d] State Key Laboratory of Silicate Materials for Architectures, Wuhan University of Technology, Wuhan 430070, China.

† Corresponding authors: zhang-yanfei@hotmail.com (Y.F.Z.), yy@bio.aau.dk (Y.Z.Y.).

Contents

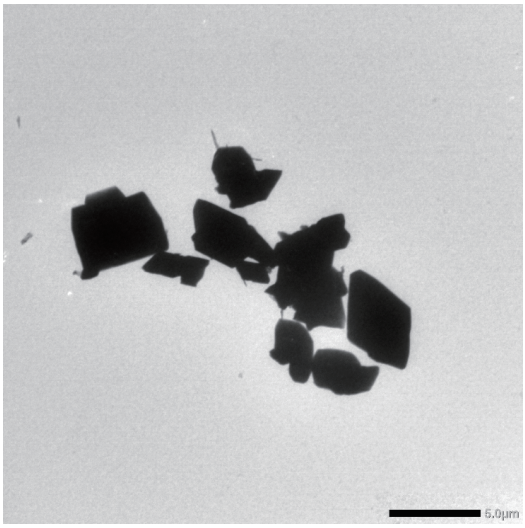

Figure S1. TEM image of Al-MOF.

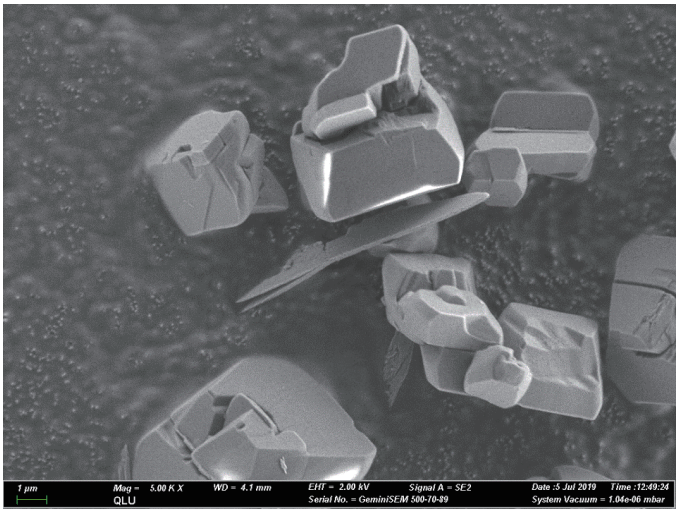

Figure S2. SEM image of Al-MOF.

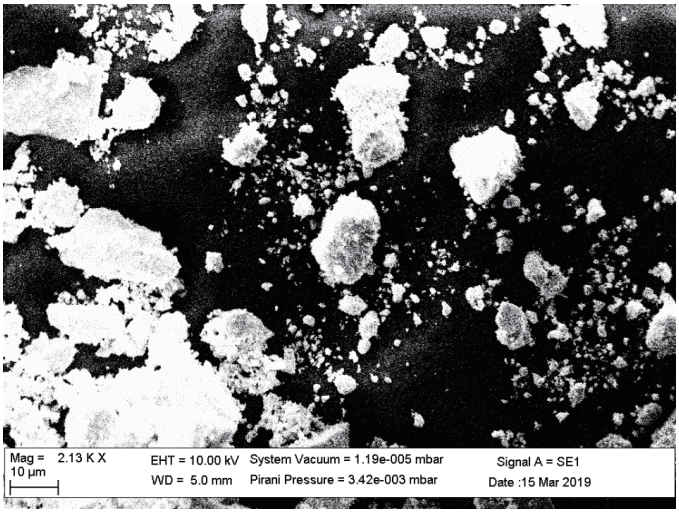

Figure S3. SEM image of SnO_2 particles.

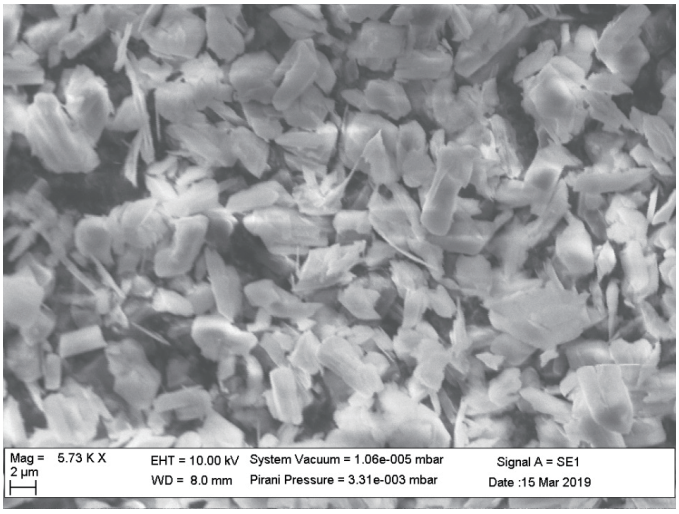

Figure S4. SEM image of SnO_2@MOF.

5.

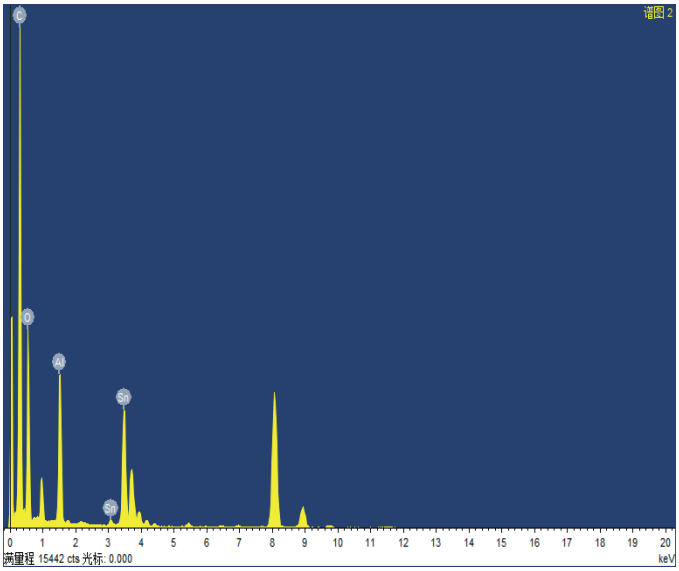

Full Scale 15442 cts Cursor: 0.000

Fig. S5. TEM EDS spectrum of SnO_2@MOF/graphene.

Table S1. Element percentage obtained from the TEM EDS spectrum.

Element	Weight percentage (%)	Atom percentage (%)
C K	50.20	74.32
O K	14.71	16.35
Al K	8.01	5.28
Sn L	27.08	4.06
All	100.00	100.00

6. Calculation of crystal size

Scherrer equation

$D_{hkl} = K\lambda/(B_{hkl}*\cos\theta)$

where D_{hkl} is the crystallite size in the direction perpendicular to the lattice planes, hkl are the Miller indices of the planes being analysed, K is a numerical factor frequently referred to as the crystallite-shape factor, normally taken as 0.9, λ is the wavelength of the X-rays, B_{hkl} is the width (full-width at half-maximum) of the X-ray diffraction peak in radians and θ is the Bragg angle.

The B_{hkl} at $\theta = 13.2°$ is around 4 degree, the corresponding D_{hkl} is 2.03 nm.

7.

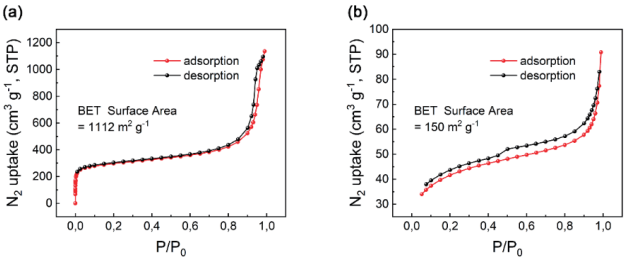

Fig. S6. N_2 adsorption/desorption isothermal curves of (a) MOF and (b) SnO_2@MOF/graphene.

8.

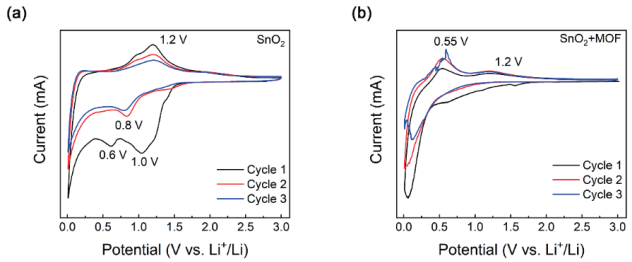

Fig. S7. Cyclic voltammetry curves of SnO_2 and SnO_2+MOF physical mixture.

9.

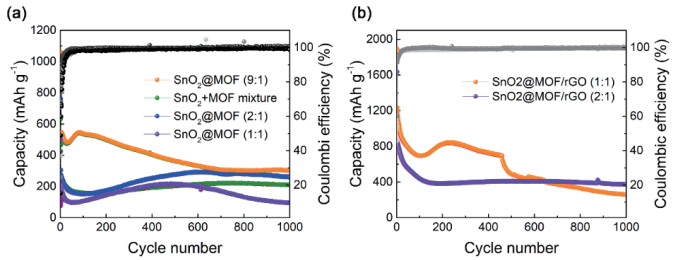

Fig. S8. (a) Cycling performance of SnO_2+MOF physical mixture, SnO_2@MOF (9:1), SnO_2@MOF (2:1) and SnO_2@MOF (1:1) at a current density of 1000 mA g^{-1} for 1000 cycles. (b) Cycling performance of SnO2@MOF/graphene with various weight percentages of SnO_2, (1:1) and (2:1), respectively, at a current density of 1000 mA g^{-1} for 1000 cycles.

10.

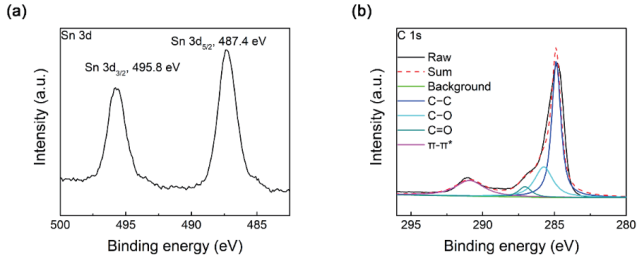

Fig. S9. XPS high resolution spectra of Sn 3d (a) and C 1s (b) of SnO_2@MOF/graphene after 1000 cycles.

11.

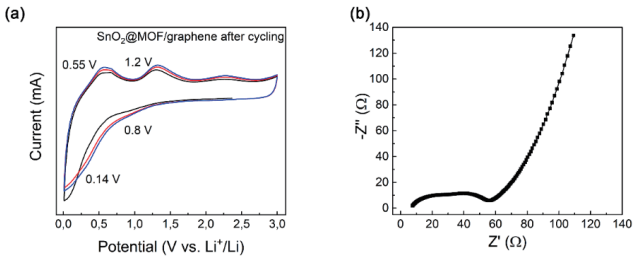

Fig. S10. (a) CV curves of SMG after 1000 cycles. (b) Nyquist plot of SnO_2@MOF/graphene after 1000 cycles.

12.

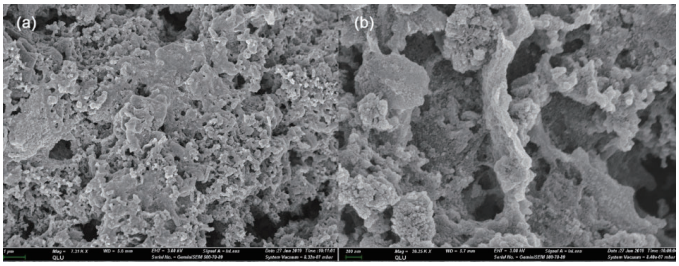

Fig. S11. SEM image of SnO_2@MOF/graphene after cycling.

ISSN (online): 2446-1636
ISBN (online): 978-87-7210-947-3 AALBORG UNIVERSITY PRESS